EXTENDING STUDIES OF OZONE PHOTODISSOCIATION TO NEAR AND FAR UV WAVELENGTHS IN THE HUGGINS AND HARTLEY BANDS

A Dissertation

by

MEGAN NICOLE AARDEMA

Submitted to the Graduate and Professional School of
Texas A&M University
in partial fulfillment of the requirements for the degree of

DOCTOR OF PHILOSOPHY

Chair of Committee,	Simon W. North
Committee Members,	Daniel P. Tabor
	David H. Russell
	George R. Welch
Head of Department,	Simon W. North

August 2023

Major Subject: Chemistry

ABSTRACT

Understanding ozone photodissociation dynamics is a key component to accurately modeling atmospheric chemistry, and the energy partitioning into the fragments and its wavelength dependence can be used to assess the potential energy surfaces used in calculations. Experimental REMPI spectra and ion images of the O_2 fragment were measured following photodissociation of O_3 in the near and far UV wavelengths. The $O_2(a^1\Delta_g)$ fragment was probed following 226 nm dissociation to extend previous studies on the Λ-doublet model to shorter wavelengths in the Hartley band and to extend studies of the j-dependent predissociation lifetime of the resonant $O_2(d^1\Pi_g)$ state used in the REMPI scheme. Following 226 nm dissociation, the $O_2(a^1\Delta_g)$ fragment is highly rotationally excited and the odd rotational states are suppressed. The rotational distribution is consistent with previous measurements at longer dissociation wavelengths, with the distribution shifting to higher rotational states and the suppression of the odd states increasing with increasing dissociation energy. The vector correlations support a parallel $\boldsymbol{\mu}$-$\boldsymbol{v}$ correlation as expected for a parallel transition from the X state of O_3 to the B state, and the $\boldsymbol{v}$-$\boldsymbol{j}$ correlation is perpendicular as expected for the dissociation of a triatomic molecule. The $\boldsymbol{\mu}$-$\boldsymbol{v}$ correlation at 226 nm is weaker than the correlation measured at longer wavelengths, which is consistent with the previously reported trend and attributed to a faster recoil velocity and less influence from the restoring force in the bending potential.

In the Huggins band, longer wavelengths excite O_3 to the bound region of the B state and spin-forbidden dissociation processes dominate. Huggins band dissociation has not been studied in as much detail as the Hartley band. Both the $O_2(a^1\Delta_g)$ and $O_2(b^1\Sigma_g^+)$ fragments

were probed following photodissociation in the Huggins band. The REMPI spectrum of $O_2(a^1\Delta_g)$ following 320 nm dissociation exhibits enhanced odd rotational states which is the opposite of the trend observed in the Hartley band and is attributed to greater coupling between the B state and $^3A''$ states correlating to odd rotational states of O_2 and weaker coupling between the B state and $^3A'$ states leading to even rotational states of O_2.

Ion image speed distributions at 320 nm and the REMPI spectrum at 330 nm both support a broad rotational state distribution of $O_2(a^1\Delta_g, v = 0)$. A 2D-REMPI spectrum collected near 330 nm allowed the simultaneous measurement of the rotational distributions of v=0-4 of the $O_2(b^1\Sigma_g^+)$ fragment and the high rotational states of $O_2(a^1\Delta_g, v = 0)$. In contrast to the broad rotational distribution of $O_2(a^1\Delta_g)$, the $O_2(b^1\Sigma_g^+)$ distribution is narrow and largely unchanging with vibrational state. The simultaneous measurements of five vibrational levels of $O_2(b^1\Sigma_g^+)$ allowed the vibrational state distribution to be obtained as well. The distribution peaks at v=0 and decreases monotonically with increasing vibrational state. New measurements of the O_2 fragment following dissociation at 320 and 330 nm will provide a stringent test of the potential energy surfaces as calculations are performed on Huggins band dissociation dynamics.

In the REMPI schemes utilized, $O_2(a^1\Delta_g)$ and $O_2(b^1\Sigma_g^+)$ are resonantly excited to the $O_2(d^1\Pi_g)$ Rydberg state which is predissociated by the $O_2(II^1\Pi_g)$ valence state. The spectral linewidth reflects the lifetime of the $O_2(d^1\Pi_g)$ state which varies significantly with rovibrational state. The predissociative lifetimes and corresponding linewidths were calculated and the potentials used in the calculations were optimized so the calculated linewidths are consistent with experimental measurements. The j-dependence of the linewidths for several vibrational levels of the $O_2(d^1\Pi_g)$ state are discussed.

DEDICATION

To my family.

In memory of Wendell Kollen.

ACKNOWLEDGEMENTS

I would first like to thank my advisor, Dr. Simon North. Thank you for being a supportive mentor, providing encouragement when I was frustrated, and for challenging me to think through my experiments and data. Thank you for many conversations over coffee about not only research but also advice about future career plans and GSAC. Thank you for always being willing to answer my questions and for making me extra coffee to get through days of laser alignment. I have learned a lot from you scientifically and professionally and I can't imagine having any other advisor for grad school.

To the North group - I could not have asked for a better group to make lasers go pew pew with. Thank you Carolyn Gunthardt for teaching me about Λ-doublets, why ozone is the greatest molecule ever, and that there is no such thing as antozone. You made research a lot of fun and I'm thankful you were my senior student. Maddie Smotzer - From recruitment weekend roomies to the ponytail teaching gang to conference travel buddies, I would not have made it through grad school without you. Thanks for bringing me chocolate on bad days and sharing your last brain cell with me on many occasions. Nick Shuber - Thank you for always being willing to talk through science (especially Ω) and for making the lab a fun place to work. Thanks for putting up with me when I dropped your phone in the diffusion pump, accidentally mopped pump oil all over the lab floor, and tested out the new label maker. Ashley Moran - You're the real MVP! You're my favorite opening day Dutch Bros date, Grey's Anatomy watching buddy, and trivia co-host. Thanks for holding office hours at Starbucks with me so we could have a weekly coffee date and finding things like 5ks in the mud for the group to do together. Taylor Best - Thanks for singing Taylor Swift songs

with me on our road trip, for always being down for an afternoon walk or coffee run, and for reminding us to make Friday lunch plans at the beginning of the week. Megan Fast - It has been fun having two Megans in the group! Thanks for deciding to join us in the imaging lab and for helping fit a complicated REMPI spectrum. You've been a fun addition to the group and I'm excited to see the work you do during your time at A&M. And Zach Buen - Thanks for being the only other person I could count on to wear shorts year round and for teaching me the best way to calibrate a doubling crystal is to yell when you see doubled light.

There are many others in the department I would also like to thank. Sandy - thank you for regularly providing chocolate and advice. Talking through things with you is always helpful. Thank you Will for not only teaching me how to use the tools in the machine shop, but also making high quality parts from my sketches on scraps of paper and helping me with many stripped and lost screws. Thank you Tim for helping me troubleshoot and fix several laser parts and Bill for fixing the bubbler quickly every time I broke it.

Thank you Dr. McBane for helpful explanations about trajectories and ozone dissociation. Thank you for letting me visit Grand Valley and showing me how to run trajectory calculations. I have learned a lot from collaborating with you.

I have had an amazing support system outside the lab as well. Thank you to my parents for many phone calls that made home feel not so far away, for regularly coming to visit, and for always letting me talk through my day. You have listened to me enough that you are able to ask questions about the lasers and experiments and that means a lot to me. Thank you Kara for making siblings weekends happen even though we live far away and for the constant stream of memes and jokes. Our conversations always make me laugh and there were many days I needed that.

Thank you Kathleen and Mackenzie for your friendship and all of the long runs and baking nights. You helped make Texas feel like home and have both been incredibly encouraging friends. Thank you Becca for your consistent thoughtfulness and support.

Thank you Doug Vander Griend, Dave Benson, and all the chemistry professors at Calvin for showing me the beauty of studying and understanding the world on a molecular level. You taught me that faith and science complement each other in endlessly fascinating ways, and I will forever be grateful.

CONTRIBUTORS AND FUNDING SOURCES

Contributors

This work was supported by a dissertation committee consisting of Professors Simon North, Daniel Tabor, and David Russell of the Department of Chemistry and Professor George Welch of the Department of Physics.

The trajectory calculations in Chapter 3 were performed by George McBane. 320 nm image speed distributions of low velocity fragments in Chapter 4 were analyzed in collaboration with Benjamen Meas. 330 nm REMPI simulations and fitting of the $O_2(a^1\Delta_g)$ spectra near 330 nm in Chapter 4 were done in collaboration with Benjamen Meas and Megan Fast.

All other work conducted for the dissertation was completed by the student under the advisement of Dr. Simon North.

Funding Sources

Support for this work was provided by the Robert A. Welch Foundation under Grant Number A-1402.

TABLE OF CONTENTS

Page

LIST OF FIGURES

FIGURE Page

LIST OF TABLES

1. INTRODUCTION

1.1 Ozone in the Atmosphere

Ozone is a critical component of the atmosphere due to the reactive products that result from its photolysis and the role ozone plays in protecting the earth from high energy UV light. Therefore, ozone is of particular interest to atmospheric chemists and has been the focus of many experimental and theoretical studies.[1–14] Understanding ozone photochemistry is key to accurately modeling atmospheric chemical processes, and discrepancies between calculations and experimental measurements involving ozone have prompted many studies on the "ozone deficit problem," which is the underprediction of stratospheric ozone concentrations in models relative to the concentrations observed. Numerous explanations to account for the deficit in the models have been proposed, including the formation of highly vibrationally excited O_2 fragments following ozone dissociation, additional reactions that lead to the production or destruction of ozone, and inaccuracies in rate constants used in the model.[8,15–29] The fact that there still remains an unaccounted for difference in ozone concentration emphasizes the importance of the interplay of theory and experiment.[30,31] Experiments are necessary to assess and refine theoretical models, as well as study complicated systems that may be difficult to study through calculations. In many cases, theory provides an explanation for the observed results and is used in predicting the results of additional studies.

Most studies of the ozone deficit problem address stratospheric ozone concentrations because ozone chemistry primarily takes place in the stratosphere. The ozone layer is a region of the stratosphere between 15 and 35 km in altitude where ozone is highly concentrated rel-

ative to the rest of the atmosphere.[32] While the ozone layer blocks a majority of high energy sunlight from reaching the earth's surface, long wavelength light passes through the ozone layer and dominates lower altitude tropospheric photochemistry. Low energy dissociation of ozone in the troposphere is believed to significantly contribute to the observed enhancement of heavy isotopes of oxygen in atmospheric ozone.[33] Previous measurements of ozone in the atmosphere have demonstrated an altitude-dependent enrichment of heavy isotopes of ozone, with greater concentrations of asymmetric isotopes than symmetric isotopes,[34–36] and as a result, studies have been conducted on both the formation and dissociation processes of heavy isotopes.[16,33,37–43] The dissociation of asymmetric molecules ($^{16}O^{16}O^{17}O$ or $^{16}O^{16}O^{18}O$) favors the formation of heavy molecular and light atomic fragments, and this preference is predicted to be stronger in the Huggins band (310-370 nm) than in lower or higher energy absorption bands.[43] The Huggins band is also predicted to have greater differences in absorption cross section between symmetric and asymmetric isotopes of ozone relative to other absorption bands.[42] The accuracy of these calculations relies heavily on the accuracy of the potential energy surfaces used in the calculations, but few experimental studies on the dissociation dynamics of ozone in the Huggins band have been performed to assess the potentials, even on ozone made up of three ^{16}O atoms. Therefore, evaluating the potential energy surfaces involved in ozone dissociation by studying the fragments from the dissociation across a range of wavelengths is crucial for understanding and modeling atmospheric ozone.

There are four main absorption bands in the UV-Visible-IR regions of light, shown in Figure 1.1 The Hartley band (200-300 nm) has the strongest absorption. The absorption spectrum in this region is broad, peaking near 260 nm, and results from excitation from the

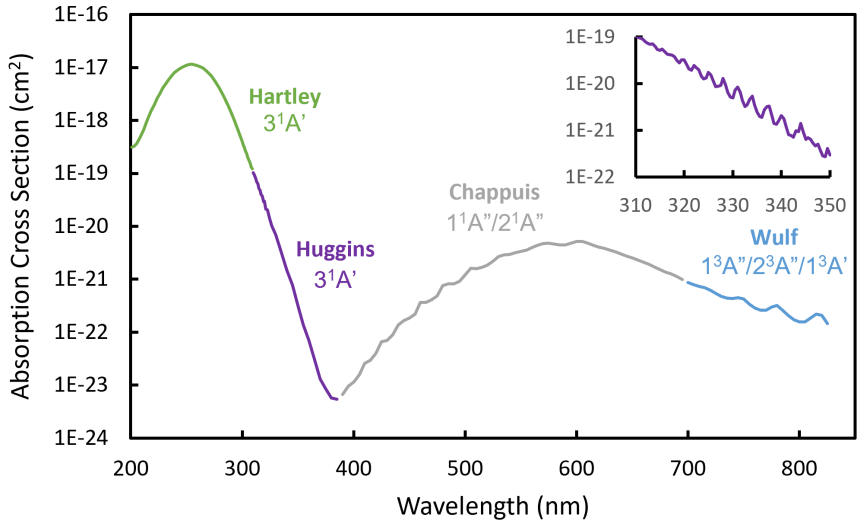

Figure 1.1: Absorption spectrum of O_3 from NASA JPL.[44] The states accessed following excitation from the ground state in each energy region is indicated.[2] The inset is a higher resolution spectrum of the Huggins band from Molina and Molina to show the structure.[45]

ground state $(^1A')$ of O_3 to the continuum of the B state $(^1A')$, which correlates with excited singlet O and O_2 products. The Huggins band (310-370 nm) is the low energy tail of the Hartley band, corresponding to excitation to the bound region of the B state. Absorption in the Huggins band is much weaker due to the large difference between ground and excited state geometries and structured due to vibrational bands.[2] The Chappuis band (400-700 nm) has a broad background with diffuse structure, resulting from excitation to the two lowest $^1A''$ states, one of which is a bound state correlating to excited singlet O and O_2, the other a repulsive state correlating to ground state triplet O and O_2. Finally, the Wulf band (700-1050 nm) corresponds to spin-forbidden transitions, primarily to the $1^3A''$ state with minor contributions from the $2^3A''$ and $1^3A'$ states. The Wulf band is structured and very weak.[2]

Following Hartley band absorption to the B state, there are two primary dissociation channels. Direct dissociation can proceed along the B state, correlating with excited singlet products $O(^1D)$ and $O_2(a^1\Delta_g)$, or trajectories can cross from the B state to the repulsive R state to produce ground state triplet products $O(^3P)$ and $O_2(X^3\Sigma_g^-)$. In the Huggins band, excitation occurs to the bound region of the B state, and the excited singlet channel is no longer energetically accessible from cold parent molecules. Below this threshold, three additional spin-forbidden channels have been observed. There are a total of five energetically accessible dissociation channels in the Hartley and Huggins bands,

$$O_3 + h\nu \longrightarrow O(^1D) + O_2(a^1\Delta_g) \qquad (310\ nm) \tag{1.1}$$

$$\longrightarrow O(^1D) + O_2(X^3\Sigma_g^-) \qquad (411\ nm) \tag{1.2}$$

$$\longrightarrow O(^3P) + O_2(b^1\Sigma_g^+) \qquad (463\ nm) \tag{1.3}$$

$$\longrightarrow O(^3P) + O_2(a^1\Delta_g) \qquad (611\ nm) \tag{1.4}$$

$$\longrightarrow O(^3P) + O_2(X^3\Sigma_g^-) \qquad (1180\ nm) \tag{1.5}$$

where Channels 1 and 5 are spin-allowed, and Channels 2-4 are spin-forbidden.[46] Spin-forbidden processes contribute significantly to the production of excited O and O_2 at long dissociation wavelengths where Channel 1 is not accessible.

Despite the numerous experimental and theoretical studies of O_3 dissociation that have been conducted, there are several questions about ozone photodissociation processes which have been recently answered or remain unanswered. First, the alternation in even and odd rotational state populations of the $O_2(a^1\Delta_g)$ fragment following Hartley band dissociation was recently attributed to a Λ-doublet propensity,[6,47] and is extended to shorter dissociation

wavelengths in the Hartley band region in this dissertation. Additionally, isotopic enrichment of ^{17}O and ^{18}O in the atmosphere is discussed in its connection to the electronic branching ratio in the Hartley band. Next, few studies have been done on the spin-forbidden dissociation processes of O_3 following Huggins band absorption. The $O_2(a^1\Delta_g$ and $b^1\Sigma_g^+)$ fragments following dissociation in Channels 3 and 4 are studied via 2D-REMPI and velocity map imaging in this dissertation. Finally, the slow-moving $O(^3P)$ fragments observed Miller et al. following 226 nm dissociation of O_3 were initially attributed to highly vibrationally excited $O_2(a^1\Delta_g)$ fragments,[8] but more recently it has been proposed that the high energy co-fragments of the low velocity $O(^3P)$ may in fact be Herzberg states of $O_2(A'\ ^3\Delta_u$ and $A\ ^3\Sigma_u^+)$.[48] Imaging studies of these fragments are proposed as a future experimental study of O_3 photodissociation in Chapter 6.

1.2 Photodissociation in the Hartley Band

Following absorption of a photon in the Hartley band, ozone is excited from the ground (X) state to the continuum of the B state ($^1A'$) above the 310 nm threshold for the spin-allowed singlet channel forming $O(^1D)$ and $O(a^1\Delta_g)$. 90% of dissociations proceed along the B state, resulting in singlet products, and the other 10% cross from the B state to the repulsive R state which correlates with ground state triplet products, $O(^3P)$ and $O_2(^3\Sigma_g^-)$. In the Hartley brand, the branching ratio between these two channels is largely wavelength and temperature-independent.[49–53]

Both the singlet and triplet dissociation channels have been well-characterized by experiments and classical trajectory calculations. The conserved O-O bond acts as a tuning mode for the triplet channel, selecting for molecules with long O-O bonds, displaced from the equilibrium geometry.[5] As a result of this selection of long O-O bonds, $O_2(X^3\Sigma_g^-)$ fragments are

highly vibrationally excited. As the dissociation energy increases, most of the additional energy appears in vibration. In the singlet channel, the vibrational distribution of the $O_2(a^1\Delta_g)$ is much colder, peaking at v=0 for all wavelengths. The O_2 fragment in both channels is rotationally excited due to differences in the bending potential between the X and B states of O_3, and the rotational energy increases with increasing dissociation energy. The anisotropy parameter, β, is positive at low j in both channels, indicative of a parallel transition as expected for the transition from the X to B state of O_3. In the triplet channel, β is j-dependent and additional bending motion in the parent molecule at the time of dissociation leads to decreasing β with increasing j, resulting in negative or near-zero values of β at high j.[5] In the singlet channel β is positive for all dissociation wavelengths, but fragments with a faster recoil velocity experience less of a restoring force in the bending potential and β decreases with increasing dissociation energy as a result of less opening of the bond angle.[4,54]

There have been several studies focused on the triplet channel products from a 226 nm dissociation following the observation of slow-moving $O(^3P)$ fragments.[4,8,55–59] The slow-moving $O(^3P)$ fragments were initially attributed to dissociations forming highly vibrationally excited $O_2(X^3\Sigma_g^-)$ co-fragments, which were thought to partially explain the ozone deficit problem. Theory has been unable to reproduce the large fraction of dissociations leading to high vibrational states,[14] and more recently the slow-moving fragments have been assigned by Schinke and co-workers to dissociations producing O_2 co-fragments in Herzberg $A'\,^3\Delta_u$ and $A\,^3\Sigma_u^+$ states following a combination of imaging experiments and dynamics calculations.[48]

The rotational envelope of the $O_2(a^1\Delta_g)$ fragment observed experimentally has largely been reproduced by theory,[4,7,12,54] but CARS experiments by Valentini et al. demonstrated

an alternation in population of the even and odd rotational states of $O_2(a^1\Delta_g)$ following O_3 dissociation, with higher populations in even states.[7,60] For decades, this was attributed to preferential curve-crossing of the odd-rotational states to the R state correlating with ground-state triplet products. Due to symmetry restrictions, the $O_2(X^3\Sigma_g^-)$ fragment can only exist in odd rotational states for a homonuclear O_2 with zero nuclear spin. According to the curve-crossing model, both odd and even rotational states of $O_2(a^1\Delta_g)$ could be formed, but the odd states would be depleted, leaving primarily even rotational states in the $O_2(a^1\Delta_g)$ fragment. This explanation implies that the alternation between even and odd rotational states should increase with longer dissociation wavelengths and higher $O_2(a^1\Delta_g)$ vibrational states because in both cases the fragments would have a lower recoil velocity, which should increase the probability of transitioning to the R state. The observed trends are in fact the opposite; the alternation is greatest at v=0, and increases with increasing dissociation energy.

Gunthardt et al. recently demonstrated that the even-odd alternation is also highly temperature dependent and have shown that it results from a Λ-doublet propensity rather than selective curve-crossing.[47] In the absence of rotation, the electronic state of the $O_2(a^1\Delta_g)$ state is doubly degenerate. One Λ-doublet (A') is symmetric with respect to the rotational plane and the other Λ-doublet (A'') is antisymmetric. The A' and A'' Λ-doublets must correspond to even and odd rotational states, respectively, because of nuclear exchange restrictions in the $O_2(a^1\Delta_g)$ state. The parent molecule has A' symmetry, so in the absence of parent rotation, A' symmetry is conserved and even rotational states of the O_2 fragment are populated. If there is rotation about the two in-plane axes of the parent molecule, the fragment O_2 rotational plane is tilted relative to the initial plane, relaxing the symmetry restrictions and allowing the formation of both Λ-doublets. As the temperature of the parent O_3 increases, the

out-of-plane rotation increases and there is increased population of the odd rotational states and therefore less alternation between even and odd states. This trend is well-described by the classical model of Gunthardt et al., as well as the observed wavelength dependence of the alternation. At higher dissociation energies, higher rotational states are populated and contributions from parent out-of-plane rotation are less significant.

Excitation of O_3 from the ground state to the B state is a parallel transition, so $\boldsymbol{\mu}$ and $\boldsymbol{v}$ should be parallel. The transition dipole moment $\boldsymbol{\mu}$ is in the molecular plane and the fragment velocity $\boldsymbol{v}$ will also be in the O_3 plane. In the dissociation of a non-rotating triatomic molecule, the molecular fragment will rotate in the molecular plane, resulting in $\boldsymbol{j}$ perpendicular to $\boldsymbol{v}$. Figure 1.2 shows the expected relationships between $\boldsymbol{\mu}$, $\boldsymbol{v}$, and $\boldsymbol{j}$ following dissociation of a non-rotating triatomic molecule. Out-of-plane rotation of the parent

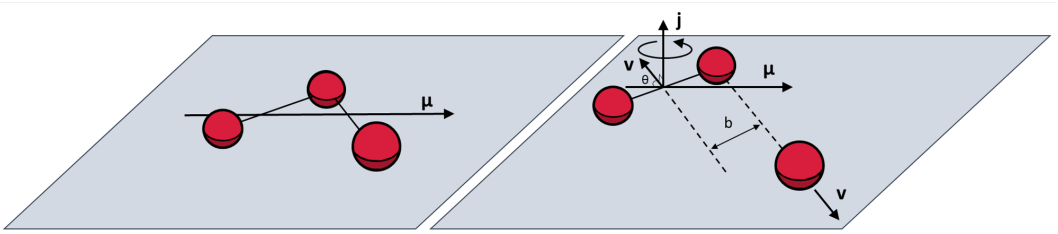

Figure 1.2: The transition dipole moment $\boldsymbol{\mu}$ is located in the molecular plane for the transition from the X state of O_3 to the B state. Both fragment translation and rotation are expected to remain in the molecular plane for the dissociation of a non-rotating parent molecule, so the velocity vector $\boldsymbol{v}$ is in the plane and the angular momentum $\boldsymbol{j}$ is perpendicular to the plane.

causes the angle between $\boldsymbol{v}$ and $\boldsymbol{j}$ to be closer to zero. Gunthardt et al. showed the temperature dependence of the $\boldsymbol{v}$-$\boldsymbol{j}$ correlation, with $\boldsymbol{v}$ and $\boldsymbol{j}$ closer to perpendicular at colder

temperatures.[47] The $\boldsymbol{v}$-$\boldsymbol{j}$ correlation is weaker for odd rotational states of O_2, indicating that odd states come from a warmer distribution of parent molecules. The Λ-doublet model has recently been confirmed by calculations using full quantum theory.[6]

In isotopically heteronuclear O_2 molecules, symmetry restrictions in both the $a^1\Delta_g$ and $X^3\Sigma_g^-$ states of O_2 are relaxed. Both Λ-doublets can correspond with even and odd rotational states of $O_2(a^1\Delta_g)$, and both even and odd rotational states of $O_2(X^3\Sigma_g^-)$ can exist. Both the curve-crossing model and the Λ-doublet model therefore predict no even-odd alternation in the rotational state distribution of heteronuclear O_2. According to the Λ-doublet model, there would be no expected change in the branching ratio between the singlet and triplet channels for heteronuclear O_2, but the curve-crossing model predicts an increase in the yield of the triplet channel because twice as many states could be occupied. Valentini et al. reported CARS spectra of both the $^{16}O^{16}O$ and $^{16}O^{18}O$ fragments following the dissociation of a mixed isotope sample of O_3.[7] The extracted populations of $^{16}O^{18}O$ fragments matched the odd states of $^{16}O^{16}O$, so the authors concluded there was equal depletion of odd and even states of $^{16}O^{16}O$ to the ground state. However, this similarity in populations does not disprove the enhancement of even rotational states of $^{16}O^{16}O$ following the Λ-doublet model. There have not been experimental measurements of the electronic branching ratios of heavy isotopes of O_3 to our knowledge, but the branching ratios have been calculated by Ndengué et al. and 90% singlet channel and 10% triplet channel is expected for all isotopes.[43] This further supports the Λ-doublet model over the curve-crossing model.

The absorption cross sections and branching ratio between the formation of heavy O atoms compared to heavy molecular O_2 following the dissociation of singly substituted heavy O_3 in the Hartley, Huggins, and Chappuis bands was studied by Ndengué et al.[33,42,43] In all

three absorption bands, the heavy atom was more likely to end up in the molecular fragment than the atomic fragment, but the preference for the molecular fragment is significantly higher in the Huggins band. Despite the minor contribution of the Huggins band to atmospheric photolysis of O_3, the Huggins band is predicted to contribute significantly to the observed enrichment of heavy O_3 isotopes. Calculations of the absorption cross sections and resulting branching ratios in the Huggins band depend on accurate potential energy surfaces, and additional experimental and theoretical studies on Huggins band dissociations are needed to calculate full 3D surfaces and assess them.

1.3 Photodissociation in the Huggins Band

Ozone absorption in the Huggins band is highly structured due to excitation to particular vibrational states in the bound region of the B state. The absorption peaks are narrow at low temperatures and broaden with increasing temperature. Figure 1.3 shows the O(^3P) yield spectrum from O'Keeffe et al. following photodissociation of O_3 in the Huggins band, which is very similar to the O_3 absorption spectrum.[61–64] The peaks are very narrow and decrease in intensity with increasing wavelength. The arrows indicate the dissociation wavelengths studied in Chapter 4.

While dissociation in the Hartley band can largely be described by three singlet states (X, B, and R), Huggins band dissociation involves interactions between the B state and triplet states correlating with spin-forbidden products. States of both A′ and A″ symmetry lead to each of the three spin-forbidden channels. Figure 1.4 shows the X, B, and R states along with the 1D potential energy curves involved in Huggins band dissociations calculated by Grebenshchikov and Rosenwaks.[65] The potential energy curves correspond to a second bond angle of 2.43 a_0 and a bond angle of 117°. In Figure 1.4, the X, B, and R states ($^1A'$)

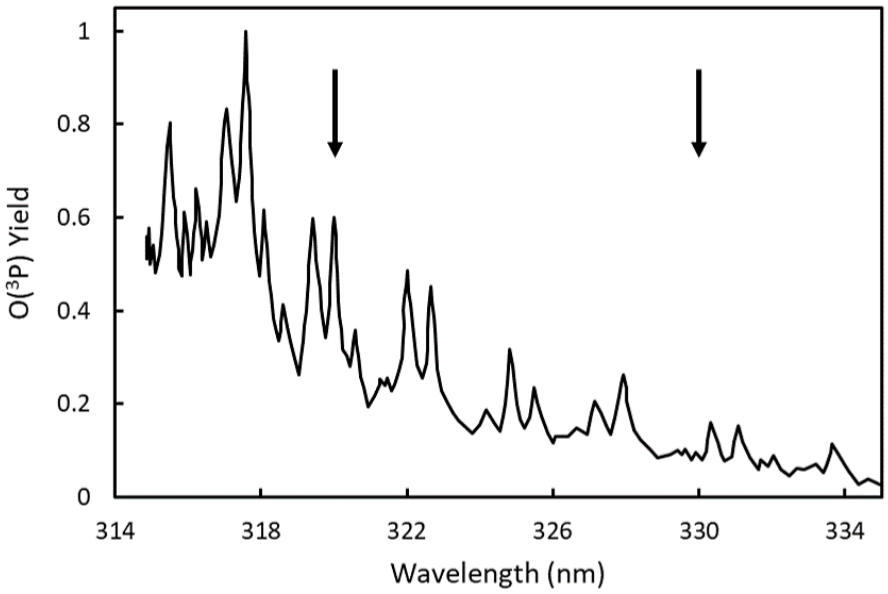

Figure 1.3: O(^3P) yield spectrum following Huggins band photodissociation of O_3 from O'Keeffe et al.[61] The O(^3P) yield spectrum is very similar to the O_3 absorption spectrum in this wavelength region. The arrows indicate dissociation wavelengths studied and discussed in Chapter 4.

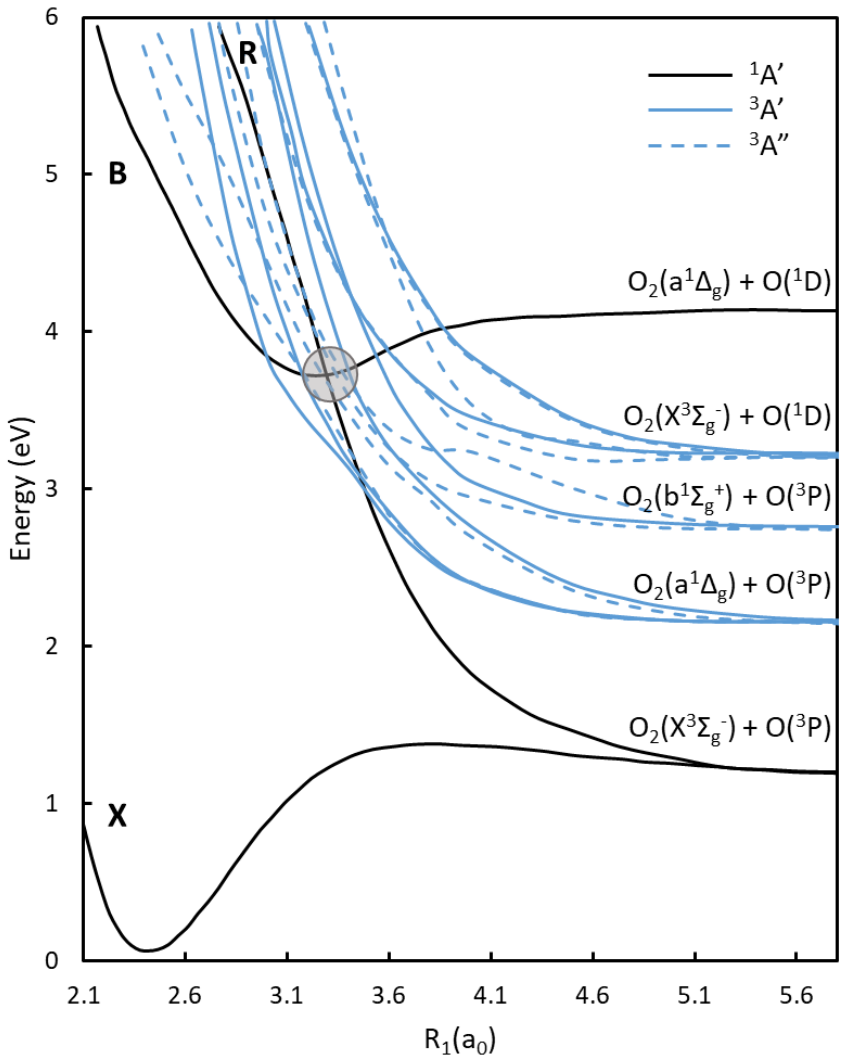

Figure 1.4: Potential energy curves calculated by Grebenshchikov and Rosenwaks.[65] The X, B, and R states are all $^1A'$ states and are shown in black. The repulsive $^3A'$ and $^3A''$ states that cross the B state and correlate with spin-forbidden products are shown in blue. The solid lines indicate states with A' symmetry and the dashed lines indicate states with A'' symmetry. The gray circle indicates the crossing point of the B and R states.

responsible for Hartley band dissociation are represented by solid black lines, and the gray circle indicates the crossing point of the B and R states responsible for spin-allowed triplet channel dissociation in the Hartley band. The blue lines indicate repulsive triplet states that cross the bound region of the B state and correlate with spin-forbidden channels. The solid lines indicate A' symmetry and the dashed lines indicate A'' symmetry. Both $^3A'$ and $^3A''$ states correlate with each of the three spin-forbidden channels.

Below 310 nm, the singlet spin-allowed dissociation channel is not energetically accessible, yet $O(^1D)$ and $O_2(a^1\Delta_g)$ have been observed following dissociation of O_3 at wavelengths longer than 310 nm.[9,64,66–69] At wavelengths slightly longer than 310 nm, the $O(^1D)$ yield is temperature dependent with greater production of $O(^1D)$ at higher temperatures. Figure 1.5 shows the $O(^1D)$ yield following Huggins band dissociation of O_3 at 200 K in blue and 250 K in purple from Ravishankara et al.[9] The temperature-dependent yield between 310 and 325 nm is attributed to dissociation from vibrationally excited O_3 parent molecules because the additional internal energy of the O_3 molecule lowers the amount of energy required to dissociate via the spin-allowed singlet channel. The $O(^1D)$ yield of 0.1 observed at cold temperatures and longer wavelengths is due to a spin-forbidden dissociation channel producing $O(^1D)$ and $O_2(X^3\Sigma_g^-)$.[9,52] This assignment is supported by broad $O(^1D)$ Doppler profiles following below-threshold dissociation of O_3 consistent with the increased $O(^1D)$ velocity for the spin-forbidden channels.[63]

There has also been evidence reported for spin-forbidden dissociation processes in time-of-flight studies. Denzer et al. performed time-of-flight spectroscopy on both the $O(^1D)$ and $O_2(a^1\Delta_g)$ fragments following dissociation of O_3 below the threshold of the spin-allowed, singlet channel.[70] Fragments were observed traveling speeds consistent with both spin-allowed

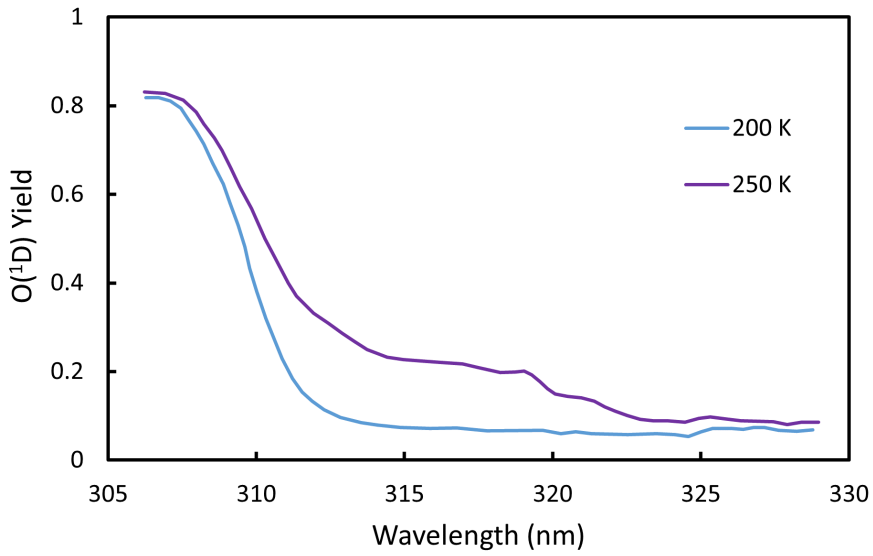

Figure 1.5: O(^1D) yield following photodissociation of O_3 in the Huggins band reported by Ravishankara et al.[9] The yield spectrum at 200 K is shown in blue and the yield at 250 K is shown in purple.

dissociation of O_3 with increased internal energy and spin-forbidden dissociation, which has a lower dissociation energy. Studies of the O(^3P) fragment following Huggins band dissociation conducted by O'Keeffe et al. showed energy distributions with three peaks, approximately the same size, attributed to O_2 co-fragments in the $X^3\Sigma_g^-$, $a^1\Delta_g$, and $b^1\Sigma_g^+$ states with equal branching ratios.[61] More recent imaging studies on the O($^3P_2$) fragment were conducted by Ulrich et al. following O_3 dissociation between 321 and 329 nm.[71] Kinetic energy distributions derived from the image radial distributions were fit by varying vibrational state populations of each of the three O_2 electronic states and the rotational temperature to minimize the deviation from the data. The rotational temperature was assumed to be the same for all vibrational and electronic states of O_2. Two models were used to fit the ki-

netic energy distributions, one with unrestricted vibrational state populations and one with population restricted to lower vibrational states. The authors concluded the branching ratio between the three channels forming O(^3P) was approximately equal across the wavelength range. The anisotropy parameter was reported for each peak in the radial distributions, but the anisotropy parameters varied widely and there was not a clear wavelength-dependent trend.

Analyzing images of the atomic fragment is difficult due to the large number of possible states of the O_2 co-fragment. As a result, significant assumptions were made about the fragment energy distributions. Studying the molecular fragment instead gives a clearer picture of the energy distributions because the corresponding atomic fragment can only occupy three nearly degenerate electronic states. Peaks in the image radial distributions can be definitively assigned, and rotational distributions and anisotropy parameters for individual dissociation channels can be individually obtained. O'Keeffe et al. studied the $O_2(b^1\Sigma_g^+)$ fragment following spin-forbidden dissociation of ozone, but probed the fragment with a REMPI scheme accessing a perturbed vibrational level of the resonant state so corrections to the rotational state populations were necessary.[72,73]

1.4 Predissociation of O_2 and Linewidths

In 2+1 REMPI schemes of the O_2 fragment, the molecule is excited from the $a^1\Delta_g$ or $b^1\Sigma_g^+$ state to the resonant $d^1\Pi_g$ state, and the linewidths in the REMPI spectra are reflective of the predissociation lifetimes of the $d^1\Pi_g$ state. The repulsive wall of the $II^1\Pi_g$ valence state cuts through the minimum of the $d^1\Pi_g$ Rydberg state, leading to predissociation as shown in Figure 1.6. The interaction between these two states and the resulting predissociation rates depend on the wavefunction overlap, and therefore varies significantly with

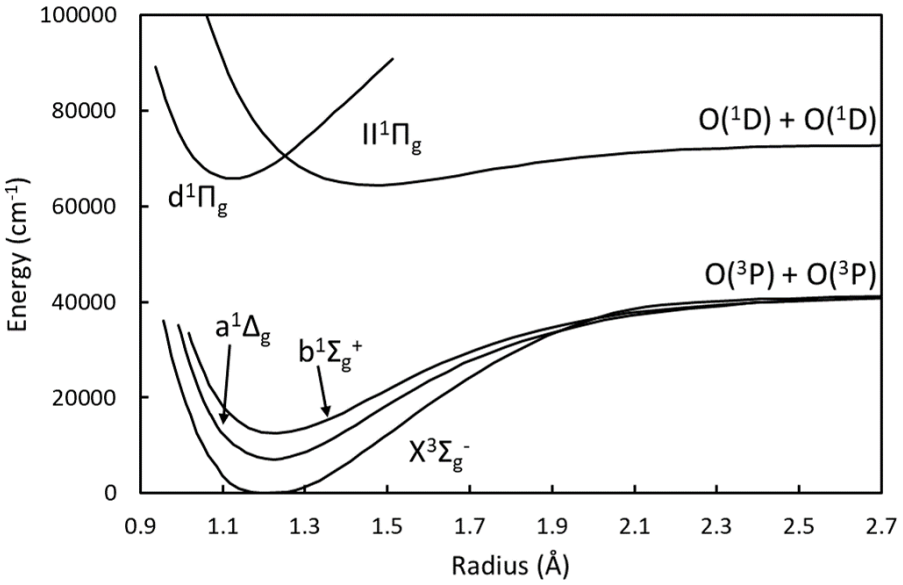

Figure 1.6: The potential energy curves from Morrill et al. for states involved in REMPI schemes between 300 and 330 nm.[74] The lowest energy state ($X^3\Sigma_g^-$) is the ground state. The $a^1\Delta_g$ and $b^1\Sigma_g^+$ states are produced from O_3 photodissociation and are excited with 2+1 REMPI to the resonant $d^1\Pi_g$ state. The $II^1\Pi_g$ state cuts through the minimum of the $d^1\Pi_g$ state, leading to predissociation.

vibrational and rotational state. The vibrational state and rotational state dependence of the linewidths for $^{16}O_2$ and $^{18}O_2$ have previously been calculated and some measurements have been made.[75,76] However, experimental measurements of the $^{16}O_2$ isotope have been limited to v=4 j=1-25 for the rotational dependence and j=1, v=4-7 for the vibrational dependence. An exponential function was used by Han et al. to fit j-dependent linewidths in a REMPI spectrum of O_2 excited to $d^1\Pi_g$, v=4, and the rotational states of $O_2(a^1\Delta_g)$ were populated up to j=37 (N=35).[6] Experimental measurements of the linewidths of higher rotational states in v=4 and higher vibrational states can be compared to the linewidths predicted by calculations of the wavefunction overlap of the $d^1\Pi_g$ and $II^1\Pi_g$ states and the corresponding predissociation rates.

2. EXPERIMENTAL

To understand the dissociation of a molecule and assess the calculated potential energy surfaces for the states involved, the scalar distributions and vector correlations of the fragments are particularly informative. The rotational distribution is reflective of the steepness of the potential with respect to bond angle relative to steepness with respect to bond length. The correlation between the transition dipole moment, $\boldsymbol{\mu}$, of the parent molecule and the fragment velocity, $\boldsymbol{v}$, depends on both the shape of the potential and the excited state lifetime. Weak correlations between the fragment angular momentum, $\boldsymbol{j}$, and both $\boldsymbol{\mu}$ and $\boldsymbol{v}$ can be indicative of a warmer distribution of parent molecules. In combination with classical trajectory calculations, experimental measurements of the fragment rotational distributions and correlations between $\boldsymbol{\mu}$, $\boldsymbol{v}$, and $\boldsymbol{j}$ can provide a picture of the dissociation process. To obtain these measurements, Velocity Map Imaging (VMI) and Resonance-Enhanced Multi-Photon Ionization (REMPI) experiments are performed.

2.1 The Imaging Chamber

The VMI apparatus is comprised of three vacuum chambers: the source, main, and detector, shown in Figure 2.1.[77–79] The source and main chambers are both pumped by Varian VHS6 diffusion pumps, backed by Welch 1397 belt-driven mechanical pumps. The detector chamber is pumped by a Turbovac 151 turbomolecular pump backed by an Edwards E2M30 rotary pump. Typical pressures without the molecular beam are 10^{-6}-10^{-7} Torr for the source and main chambers and 10^{-8} Torr for the detector chamber. Running experiments under vacuum is essential for creating a collision free environment.

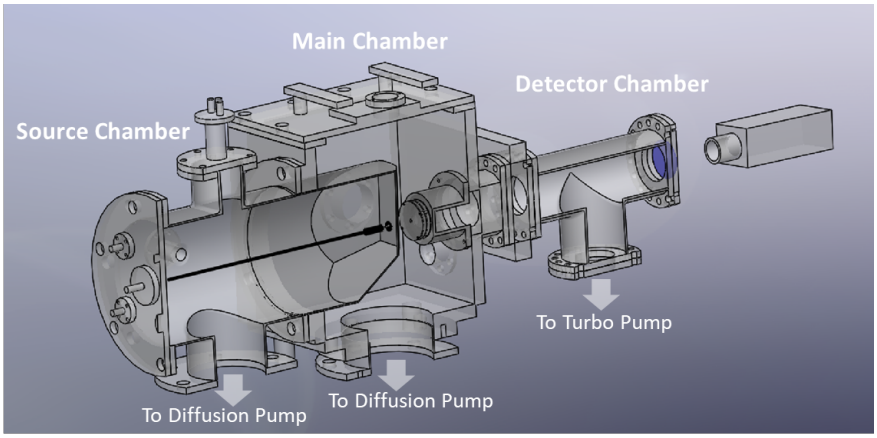

Figure 2.1: The velocity map imaging apparatus, consisting of the source, main, and detector chambers. Diffusion pumps are below the source and main chambers, and a turbo pump is below the detector chamber.

Ozone is trapped on silica beads in a bubbler and helium is flowed over the beads to generate the molecular beam. Ozone is created by flowing O_2 through an ozone generator (Ozone Engineering LG-7), which uses an electrical discharge to convert O_2 to O_3, and the resulting O_3 is trapped on silica beads in a dry ice/acetone bath at -78°C. The bubbler and silica beads are dried in a vacuum oven before each experiment to minimize the amount of water present because in the presence of water, O_3 does not adsorb to the beads as well. Once the ozone has been trapped, the headspace of the bubbler is vacuumed off and the bubbler is kept in an acetone bath near -40°C for the duration of the experiment. Helium is flowed over the the silica beads for a total pressure of 800 Torr to generate a molecular beam with approximately 5% seeding of O_3.

The molecular beam is introduced into the source chamber through a General Valve series 9 pulse valve, with an opening time of 300-400 μs. The beam is then collimated

by a skimmer cone between the source and main chambers, which selects for molecules traveling directly towards the detector with no velocity in the detection plane. This ensures any fragment translational energy in the images is a result of the dissociation rather than initial motion of the parent molecule. A skimmer cone with a smaller diameter selects for a distribution of O_3 molecules with a colder translational temperature. A skimmer cone with a 200 μm diameter was used for 226 nm dissociation experiments and 1 mm skimmer cone for experiments at 320 and 330 nm.

In the main chamber, the molecular beam is intersected at 90° by a linearly polarized laser to dissociate the molecule, and a second laser is used to selectively ionize the fragments for detection. In a 1-color experiment, a single laser is used for both photolysis and probing the fragments. The main chamber contains a series of high voltage, positively charged ion optic plates which function as Einzel lenses to velocity map the fragments onto the detector. The first plate is the repeller and has the highest voltage, typically between 3000-4000 V. The following lenses have lower voltages: 2652 V and 2299 V following a 3000 V repeller and 3544 V and 3087 V following a 4000 V repeller. The laser beams interact with the molecular beam between the repeller and the next ion optic as shown in Figure 2.2, and fragments in specific states are ionized based on the transitions resonant with the probe wavelength.

The repeller accelerates the ionized fragments down a 50 cm field-free flight tube toward the detector, which is comprised of a pair of microchannel plates (MCPs) that amplify the signal and a phosphor screen for visualization. Ionization of the fragments prior to their acceleration down the flight tube allows mass selection of the detected fragments because fragments with different mass-to-charge ratios will reach the detector at different times. For most of the experiment, a voltage of 1200 V is applied to the MCPs, which is not enough

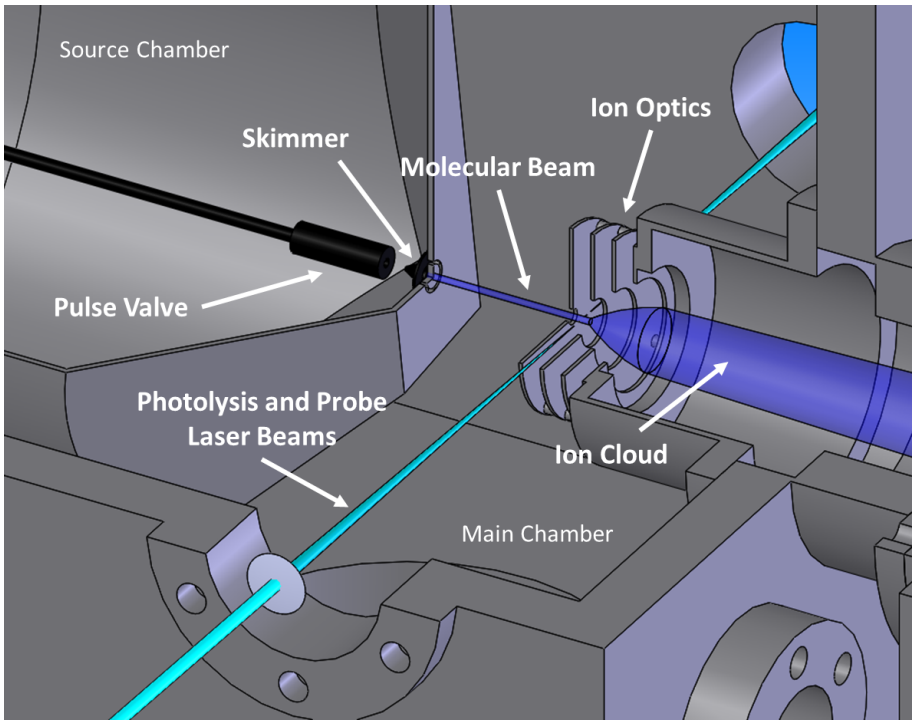

Figure 2.2: The molecular beam is introduced into the source chamber by the pulse valve and collimated as it enters the main chamber through the skimmer cone. The laser beams intersect the molecular beam between the repeller and the other ion optics. Following ionization, the fragments are accelerated toward the detector.

gain to visualize ions. At the time corresponding to the arrival of the mass of interest, the MCP voltage is increased to 2400 V. This high voltage results in a gain of 10^6 when ions hit the MCPs and a cascade of electrons is created.

The amplified signal on the phosphor screen is then captured by either a Hamamatsu R928 photomultiplier tube (PMT) or a CCD camera. For experiments looking at total ion signal as a function of wavelength, the PMT was used. When spatial resolution of the fragments was needed, the CCD camera was used. A centroiding algorithm was used for higher spatial resolution in images.[80]

The observed radial and angular distributions of the fragments are dependent on the temperature of the molecular beam because additional energy in the parent molecule can blur the speed distributions and decrease the vector correlations. The expansion of the molecular beam into the main chamber results in significant rotational cooling of the O_3 molecules, and the resulting rotational temperature of the molecular beam is dependent on the distance between the pulse valve and the skimmer cone ($\sim$ 4 cm for 320 and 330 nm experiments), the backing pressure of the buffer gas, and the timing of the pulse valve relative to the lasers. Moving the pulse valve back from the skimmer, increasing the backing pressure, and probing molecules early in the pulse all decrease the observed beam temperature.

A temperature calibration probing NO was performed with similar running conditions to the ozone experiments to estimate the ozone beam temperature. NO was used because its spectroscopy is well characterized and understood. N_2O_4 was trapped in a bubbler and He was flowed over the solid N_2O_4 to generate a beam of NO_2 and NO in He. The bubbler was kept in a -30°C bath, and the same pulse valve timing was used as for ozone. NO was probed with via the $A \leftarrow X$ transition with 1+1 REMPI at 226 nm, with 50-100 μJ of laser

power. The NO signal was highly concentrated in the center spot of the image, so the ion optics were defocused to spread out the signal and prevent saturation. The resulting NO REMPI spectrum was fit with LIFBASE to obtain a rotational temperature of 50 K for the experiments at 320 and 330 nm, as shown in Figure 2.3.[81]

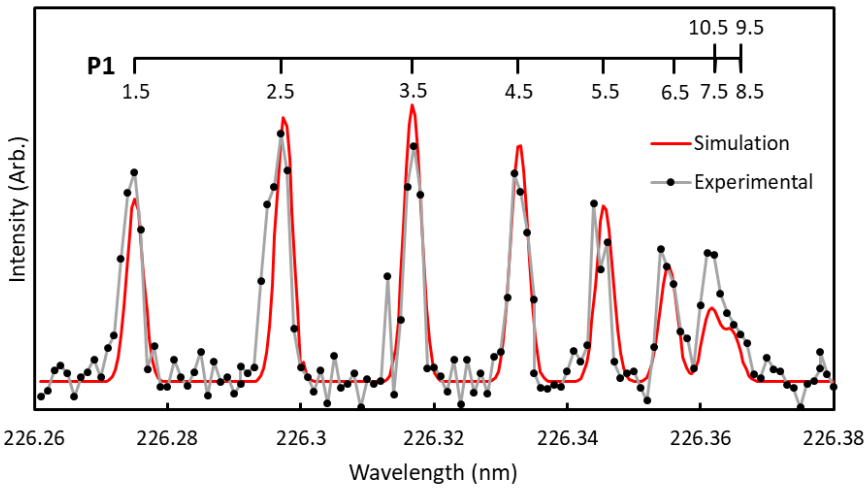

Figure 2.3: NO REMPI spectrum collected in a 1-color experiment near 226 nm used for temperature calibration. The NO was probed with 1+1 REMPI via the $A \leftarrow X$ transition. The black circles indicate experimental data and the solid red line is a simulation of a 50 K rotational distribution from LIFBASE.[81]

2.2 Laser Wavelengths and REMPI Schemes

State-selective ionization and detection of the fragments following photodissociation relies on the probe wavelength being resonant with the energy of a transition from the state of interest to a higher energy state before ionization of the fragment. Figure 2.4 shows a 2+1 REMPI scheme that excites an O_2 molecule from the ground vibrational state of $O_2(a^1\Delta_g)$

to v=4 of the resonant $d^1\Pi_g$ state before ionizing the fragment, which allows detection. As

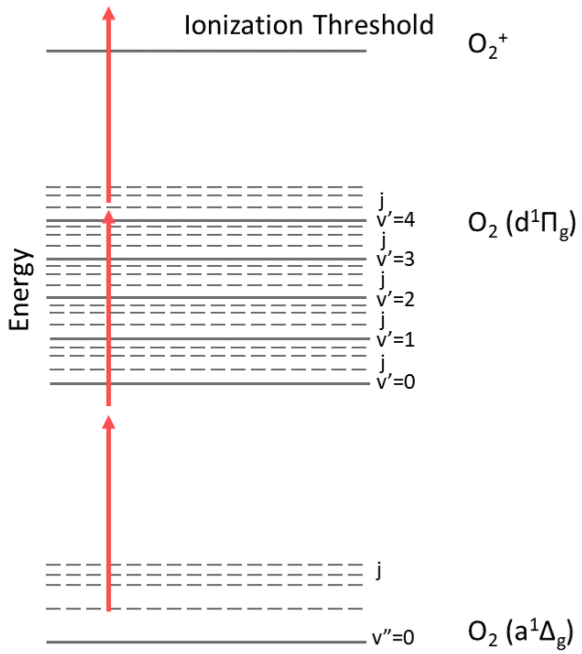

Figure 2.4: 2+1 REMPI uses two photons to resonantly excite the fragment of interest to a higher electronic state and a third photon to ionize the fragment. As the laser energy changes, the rotational states of the fragment are probed individually.

the laser wavelength is scanned, the laser energy will be resonant with transitions of different rotational states of the O_2 fragment, allowing them to be probed individually. When the laser is resonant with a particular transition, the probability of exciting molecules in the corresponding initial state increases, resulting in an increase in the number of ions detected. Peaks in the spectrum can then be assigned to individual rotational states of the fragment, and the relative intensities of the peaks are reflective of the relative population of each state.

In some cases, there was signal in the center of the detector from O_2 in the beam, not originating from the dissociation of ozone, or low-velocity signal that was non-resonant or from a different ozone dissociation channel than the channel being studied. In these cases, a mask was used to block the center of the detector from the PMT. An example of an image with a mask is shown in Figure 2.5. The signal of interest in the images is the outer ring, and the image on the left includes low-velocity signal that would contribute to the collected signal in the REMPI spectrum. In the image on the right, the mask blocked the low-velocity signal and only the high velocity signal was collected by the PMT. While some high velocity

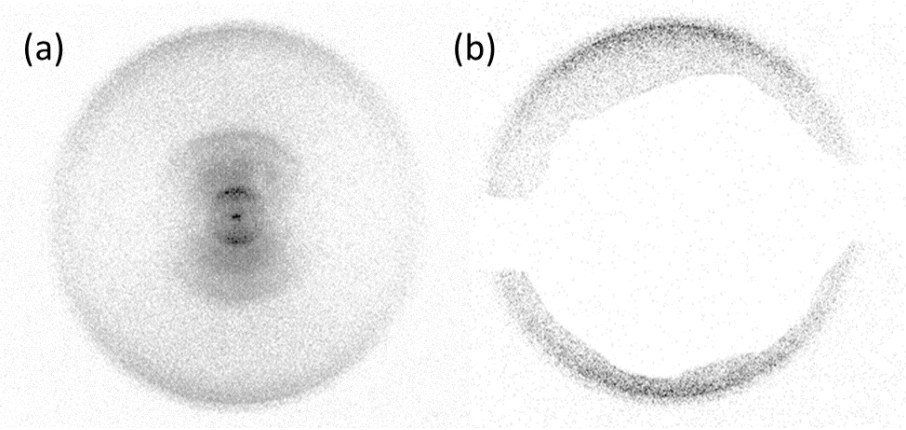

Figure 2.5: (a) An image of $O_2(a^1\Delta_g; v = 0, j = 19)$ collected in a 1-color experiment near 320 nm probed via the S-branch transition without a mask on the detector which includes fragments with both low and high velocities. (b) In the image on the right the mask blocks low-velocity signal from the PMT.

signal in the center of the image is blocked by the mask, the effect is assumed to be minor and the anisotropy is assumed to be similar for images collected with vertical polarization.

State-selective ionization and detection of fragments following photodissociation necessitates precise control of the laser wavelength, typically with a dye laser. All laser systems used in the following experiments involved a dye laser pumped by a Nd:YAG laser. The 226 nm photolysis beam was generated by frequency doubling the output of a Sirah Cobra dye laser operating near 450 nm, pumped by a frequency tripled Spectra Physics PRO 230-10 Nd:YAG laser. The probe beams at 303 nm, 320 nm, and 330 nm, were generated by frequency doubling the output of an LAS LDL 2051 dye laser, pumped by a frequency doubled Spectra Physics LAB 150-10 Nd:YAG laser. A summary of the dyes used for each wavelength range is shown in Table 2.1. The laser wavelengths were calibrated by optogalvanic

Wavelength	Oscillator	Amplifier	REMPI Transition
226 nm	0.20 g/L C450	N/A	Used for Photolysis
303 nm	0.097 g/L R610 0.017 g/L R640	0.033 g/L R610 0.006 g/L R640	4-0 $d^1\Pi_g \leftarrow\leftarrow a^1\Delta_g$
320 nm	0.22 g/L DCM	0.073 g/L DCM	2-0 $d^1\Pi_g \leftarrow\leftarrow a^1\Delta_g$
330 nm	0.22 g/L DCM 0.045 g/L LDS698	0.075 g/L DCM 0.015 g/L LDS698	1-0 $d^1\Pi_g \leftarrow\leftarrow a^1\Delta_g$ 4-0 $d^1\Delta_g \leftarrow\leftarrow b^1\Sigma_g^+$

Table 2.1: Dye concentrations for each wavelength used in experiments along with the REMPI scheme corresponding to each wavelength. All dye solutions were made in methanol.

spectroscopy using a Mg-Ne or Cu-Ne hollow cathode lamp. In the two-color experiments, there was a 25 ns delay between the photolysis and probe laser pulses. The polarization of the 226 nm beam was controlled by a double-Fresnel rhomb and a Glan polarizer, and the LAS beam polarization was controlled by a photoelastic modulator and a Glan polarizer.

In the detection of O_2 in the $a^1\Delta_g$ or $b^1\Sigma_g^+$ states, $O_2(d^1\Pi_g)$ is used as the resonant state. The repulsive wall of the nearby valence state ($II^1\Pi_g$) crosses through the minimum of the $d^1\Pi_g$ state, as shown in Figure 2.6, and the interaction between these two states results in significant perturbation of the lower vibrational levels of the $d^1\Pi_g$ state. When O_2 is excited to v=4 or higher of the $d^1\Pi_g$, it is above the dissociation threshold of the $II^1\Pi_g$ valence state and is therefore unperturbed. Unperturbed vibrational levels are necessary for obtaining

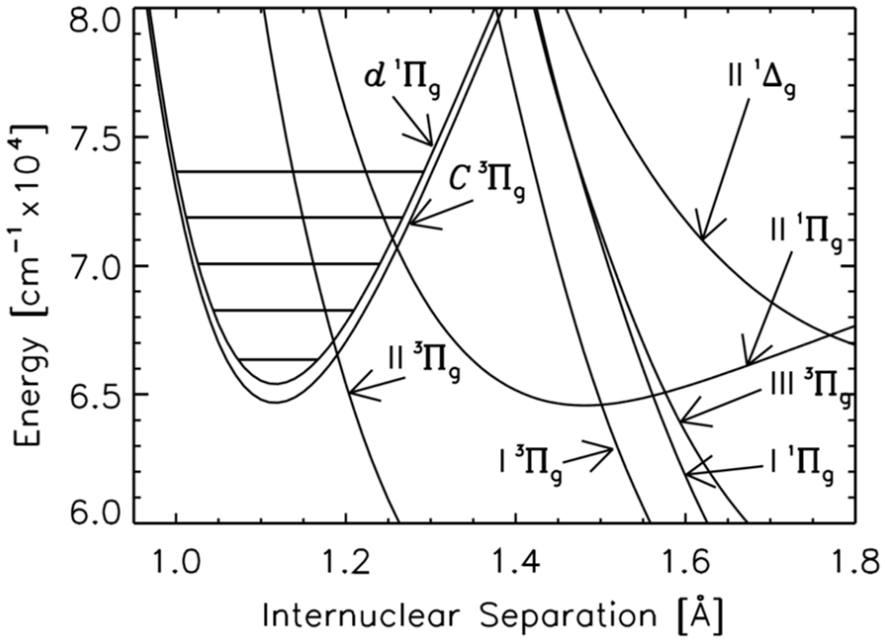

Figure 2.6: Potential energy curves for excited states of O_2 from Morrill et al.[82] The $O_2(d^1\Pi_g)$ state is accessed in REMPI schemes of the $a^1\Delta_g$ and $b^1\Sigma_g^+$ states between 300 and 330 nm. The lower vibrational levels (v$\leq$3) of the $d^1\Pi_g$ state are highly perturbed due to interactions with the $II^1\Pi_g$ state. Reprinted from *J. Molec. Spec.*, 219, 2, Morrill et al., Two-photon REMPI spectra from $a^1\Delta_g$ and $b^1\Sigma_g^+$ to $d^1\Pi_g$ in O_2, 200-216, Copyright 2003, with permission from Elsevier.

accurate rotational state distributions of the O_2 fragment, but perturbed levels can be used for imaging studies. The vibrational levels corresponding to each laser wavelength used are included in Table 2.1, and additional discussion about the selection of REMPI schemes is included in the following chapters.

REMPI spectra were typically collected in segments to maintain 2-laser alignment and laser power, and the segments were stitched together to obtain the final spectrum. For each segment in a 1D-REMPI, two spectra were collected: one with the pulse valve on and one with the pulse valve off for background correction. The background scan was fit with a 3rd order polynomial and subtracted from the scan collected with the pulse valve on. In most cases, multiple scans were collected for the same wavelength region, and these were added together following background correction of the individual scans. Each segment contained a peak that overlapped with the adjacent segments on both sides of the spectrum, and the overlapping peaks were used to scale the adjacent segments relative to each other. The overlapping regions were averaged in the final spectrum.

Once a REMPI spectrum was collected, the rotational state populations of the O_2 fragment were obtained by fitting the experimental spectrum with a simulation. Because 2+1 REMPI was used for all experiments, O, P, R, and S branches are included in the simulation for Δj=-2, -1, 1, and 2 (where j=N+L). The simulation includes transition energies calculated from rotational constants corresponding to the initial and final states of the transition. The transitions are represented by Lorentzian functions and scaled by two-photon line strengths from Bray and Hochstrasser[83] and adjustable populations. The spectra were initially fit by manually adjusting the populations, and the final populations and error bars were determined by Monte Carlo simulation. In the Monte Carlo fitting process, a random number is gener-

ated that scales the populations of each rotational state between 0.5 and 1.5 times the manual fit. A χ^2 threshold is set and any randomly generated rotational state distributions that result in a spectrum with a χ^2 value below the set threshold are saved. The distribution of populations for each rotational state that result in acceptable fits are fit with a Gaussian function, and σ is used for the error bars.

A Lorentzian function was chosen for simulations of the spectra because the dominant broadening mechanisms should lead to a Lorentzian line shape. Doppler broadening is Gaussian, but causes negligible broadening. The Doppler broadening can be calculated by the equation

$$\nu = \nu_0 \left(1 + \frac{\mathrm{v}}{c}\right) \tag{2.1}$$

where ν_0 is the transition frequency, v is the particle velocity along the probe axis, and c is the speed of light. For a molecule traveling 1500 m/s following dissociation and a transition frequency of 66,000 cm^{-1}, the Doppler shift would be 0.33 cm^{-1}. Lifetime, power, and pressure broadening all result in a Lorentzian line shape.

Lifetime and power broadening are the dominant broadening mechanisms in our experiments, leading to linewidths of 5 cm^{-1} or higher. A Voigt line shape is the combination of a Gaussian and Lorentzian function, which would most accurately describe the contributions from Doppler, lifetime, and power broadening, but because the Gaussian contributions from Doppler broadening are so small relative to the lifetime and power broadening, the peaks in the spectra can reasonably be fit with a Lorentzian function. Lifetime and power broadening and the linewidths used to fit experimental spectra will be further discussed in Section 2.5 and in Chapter 5.

2.3 Image Analysis

In a traditional 1D-REMPI spectrum, the total ion signal is collected and there is no information about the co-fragment. In an imaging experiment, the fragments are state-selected with REMPI and imaged with a position-sensitive detector. This allows measurement of the fragment speed, which can then be used to determine the co-fragment speed through the conservation of momentum. Imaging of molecular beam photodissociation was first performed by Chandler and Houston in 1987[84] and velocity-mapping lenses were added by Eppink and Parker in 1997.[85] In velocity map imaging, all fragments with the same initial velocity are mapped onto the same point on the detector, increasing the resolution of the images. Because the molecular beam is collimated at the skimmer cone, any velocity in the plane of the detector must be a result of the dissociation. After images are collected, they are symmetrized. In this process the image is reflected across mirror planes, resulting in four equivalent quadrants of the image, where each quadrant is an average of the four quadrants of the raw image.

All images in this dissertation are crushed images, meaning the entire 3D sphere of fragment molecules is projected onto the 2D detector. This results in blurring of the radial distribution, because fragments with velocity in the z-direction (perpendicular to the detector) will have less velocity in the x and y directions (in the plane of the detector). The center slice of the of the 3D sphere has the maximum velocity in the x and y directions and no velocity in the z direction, so this center slice is needed for accurate radial distributions of the images. Images with cylindrical symmetry around an axis parallel to the detector can be reconstructed to calculate the original 3D sphere from the 2D projection. The Polar Onion Peeling Algorithm uses the outer ring of the image to calculate the outer shell of the 3D sphere, and subtracts this signal from the inner radii.[86] This process is done ring by ring

until the center of the image is reached. Approximations are necessary in the Polar Onion Peeling method because the image is comprised of discrete pixels and is not a continuous function.[87] The algorithm pBASEX can be used for reconstruction as well, which fits the radial distribution with Gaussian distributions before reconstructing. This results in well-behaved functions for the reconstruction calculations and a smoother radial distribution.[88,89] Figure 2.7 shows a symmetrized image (a) before reconstruction, and two reconstructed im-

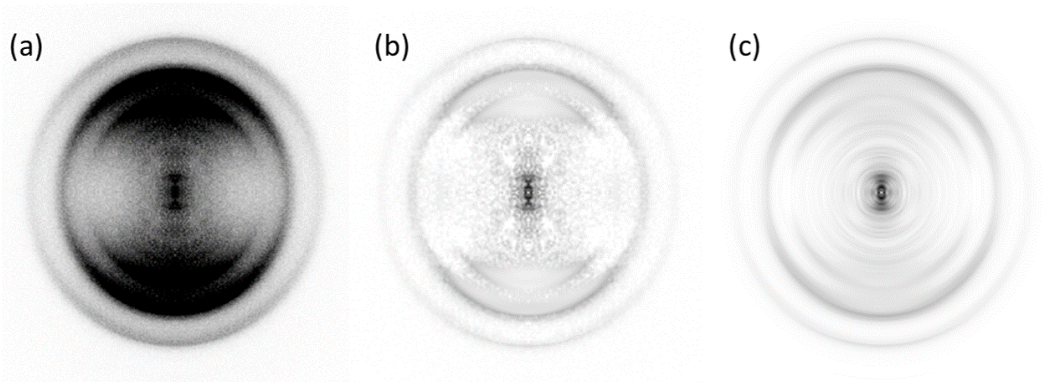

Figure 2.7: The image in (a) is a symmetrized image, representing the projection of the 3D sphere of fragments onto the detector. The second ring from the outside corresponds to the S-branch transition of $O_2(b^1\Sigma_g^+; v = 0, j = 34)$ and the assignments of the other rings are discussed in Chapter 4. The images in (b) and (c) are reconstructed, (b) with the Polar Onion Peeling algorithm and (c) with pBASEX.

ages using the Polar Onion Peeling algorithm (b) and pBASEX (c). The reconstructed image in (b) has higher levels of noise than the reconstructed image in (c).

The radius of the fragments in the image is directly related to their speed, and information

about the co-fragment can be determined using the conservation of energy,

$$E_{avail} = E_{int,O_3} + h\nu - D_0 = E_{int,O_2} + E_{int,O} + E_{trans} \tag{2.2}$$

where E_{int} is the internal energy of O_3, O_2, or O, $h\nu$ is the photon energy, D_0 is the dissociation energy, and E_{trans} is the translational energy of the fragments. The O_3 molecular beam should have very little internal energy following jet-cooled expansion into the chamber, but the temperature of the distribution can be measured and the corresponding distribution of energies included in energy calculations. Internal energy distributions of O_3 at 50 K and 300 K are shown in Figure 2.8 in blue and purple, respectively. At 300 K the O_3 internal energy distribution is much broader than 50 K. The energy values are binned, so the trends do not extend to 0 cm^{-1} of internal energy. The photolysis laser wavelength determines $h\nu$, and

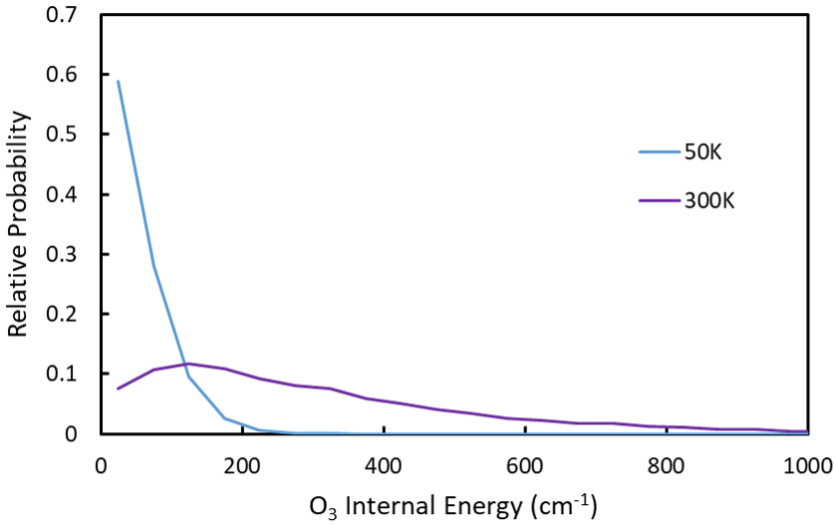

Figure 2.8: Internal energy distributions for O_3 at 50 K is shown in blue and the distribution for 300 K is shown in purple.

the probe laser wavelength is chosen to probe an individual state of the detected fragment. The speed of the detected fragment can then be used to determine the internal energy of the co-fragment.

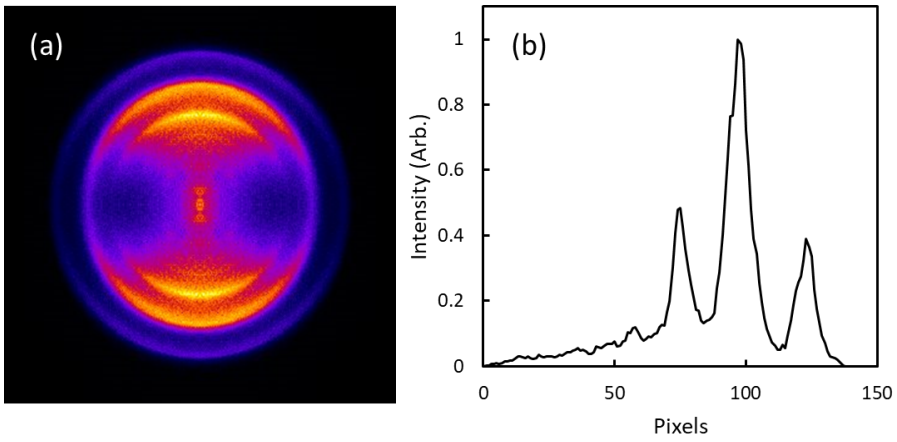

Figure 2.9: An ion image of O_2 following photodissociation of O_3 near 330 nm is shown in (a). The image contains several rings, corresponding to fragments traveling different speeds. The radial distribution in (b) corresponds to the intensity of the image as a function of radius following reconstruction. The tallest peak near 100 pixels is assigned to $O_2(b^1\Sigma_g^+; v = 0, j = 34)$ probed via an S-branch transition.

Figure 2.9 (a) shows an example of an image with multiple rings that can be assigned to multiple electronic and vibrational states of the fragment. The image is symmetrized, but it is not reconstructed so it represents the projection of the 3D sphere onto the detector. The radial distribution shown in (b) corresponds to the reconstructed image. There are three distinct peaks near 75, 100, and 120 pixels, with an additional small peak near 60 pixels. The pixels of the image can be converted to speed to obtain the speed distribution with a speed-

to-pixel ratio, which depends on experimental parameters including the ion optic voltages and flight tube length. The speed-to-pixel ratio can be determined measuring the radius (in pixels) of a fragment with a known speed. Based on the fragment speeds, the rings in Figure 2.9 are assigned to the ground vibrational state of $O_2(a^1\Delta_g)$ and multiple vibrational states of $O_2(b^1\Sigma_g^+)$. These assignments will be further discussed in Chapter 4. In many cases, a single state of a molecule is probed and the speed distribution reflects the internal energy of the co-fragment. In Figure 2.9 however, multiple states of O_2 are probed simultaneously, all with the same $O(^3P)$ co-fragment. It is also possible to have overlapping rotational transitions for the same electronic and vibrational state of the fragment. Because rotational state spacing is much smaller than vibrational and electronic state spacing, the fragments will be much closer together in speed, but it can still be possible to resolve differences in the speeds of fragments in low rotational states relative to high rotational states.

In addition to the radial distributions, spatially resolved images provide information about the angular distributions of the fragments. The angular distributions of multiple images can be used to extract correlations between the transition dipole moment $\boldsymbol{\mu}$, the velocity of the fragments $\boldsymbol{v}$, and the angular momentum of the fragments $\boldsymbol{j}$. These correlations can be indicative of the shape of the potential and the excited state lifetime. The probability (P) of a molecule absorbing a photon depends on the alignment of the molecule's transition dipole moment ($\boldsymbol{\mu}$) and the electric field of the laser ($\boldsymbol{E}$) according to the equation

$$P = |E \cdot \mu|^2 = (|E||\mu| cos\theta)^2 \tag{2.3}$$

where θ is the angle between $\boldsymbol{E}$ and $\boldsymbol{\mu}$. The probability of absorbing a photon is therefore a $\cos^2$ distribution with the highest probability of absorption when $\boldsymbol{\mu}$ and $\boldsymbol{E}$ are parallel and

the lowest probability when $\boldsymbol{\mu}$ and $\boldsymbol{E}$ are perpendicular.

The probe laser also selectively ionizes fragments in certain orientations, adding complexity to the observed angular distributions. The lasers can have vertical (V) or horizontal polarization (H), which corresponds to polarization parallel or perpendicular to the detection plane, respectively. In a 2-color experiment, the polarization of the photolysis and probe lasers can be controlled independently and the angular distributions of images collected with different laser geometries can be used to extract vector correlations. Typically a combination of VH, HV, and VV images is used to calculate vector correlations, where the first letter indicates the polarization of the photolysis laser and the second letter indicates the polarization of the probe laser. An HH geometry with both lasers horizontally polarized will produce an isotropic distribution of fragments, which cannot be used to obtain vector correlations. Each vertically polarized photon adds a cos^2 component to the angular distribution, resulting in the following equations for the angular distributions of VH, HV, and VV geometries, respectively.

$$I^{VH}(\theta) = 1 + \beta_2^{VH} P_2(cos\theta) \tag{2.4}$$

$$I^{HV}(\theta) = 1 + \beta_2^{HV} P_2(cos\theta) + \beta_4^{HV} P_4(cos\theta) \tag{2.5}$$

$$I^{VV}(\theta) = 1 + \beta_2^{VV} P_2(cos\theta) + \beta_4^{VV} P_4(cos\theta) + \beta_6^{VV} P_6(cos\theta) \tag{2.6}$$

In Equations 2.4-2.6, P_2, P_4, and P_6 are the second, fourth, and sixth Legendre Polynomials, and the β values are the image anisotropy parameters. Only VV images have the cylindrical symmetry required for reconstruction, so the analysis of images collected in VH or HV geometries involves taking a narrow slice of the outer ring of the image, which includes fragments with maximum velocity in the detection plane and no velocity perpendicular to

the plane. Alternatively, sliced imaging can be used rather than reconstruction of crushed images to obtain the center slice of an image. In sliced imaging, a lower repeller voltage is used to slow the fragments along the time-of-flight axis. Because the fragments are more spread out, it becomes possible to detect only a narrow slice in the center of the fragment sphere with the pulsed increase in MCP voltage.[90]

The vector correlations between $\boldsymbol{\mu}$, $\boldsymbol{v}$, and $\boldsymbol{j}$ can be described by Dixon's semiclassical bipolar moment formalism.[91] According to this formalism, the low-order bipolar moments, $\beta_0^2(20)$, $\beta_0^2(02)$, and $\beta_0^0(22)$ represent the expectation values for the second Legrendre polynomial, $\langle P_2(cos\theta)\rangle$, where θ is the angle between $\boldsymbol{\mu}$ and $\boldsymbol{v}$, $\boldsymbol{\mu}$ and $\boldsymbol{j}$, and $\boldsymbol{v}$ and $\boldsymbol{j}$, respectively. The values of $\beta_0^2(20)$, $\beta_0^2(02)$, and $\beta_0^0(22)$ range from -0.5 for a perpendicular correlation to 1 for a parallel correlation. The bipolar moments can be related to the measured image anisotropy parameters for images collected with 2+1 REMPI using the equations of Wei et al.,[92] which are included in Appendix A.

In Dixon's bipolar moment formalism, there are five limiting cases for the orientation of the $\boldsymbol{\mu}$, $\boldsymbol{v}$, and $\boldsymbol{j}$ vectors relative to each other, as shown in Figure 2.10. The three vectors can

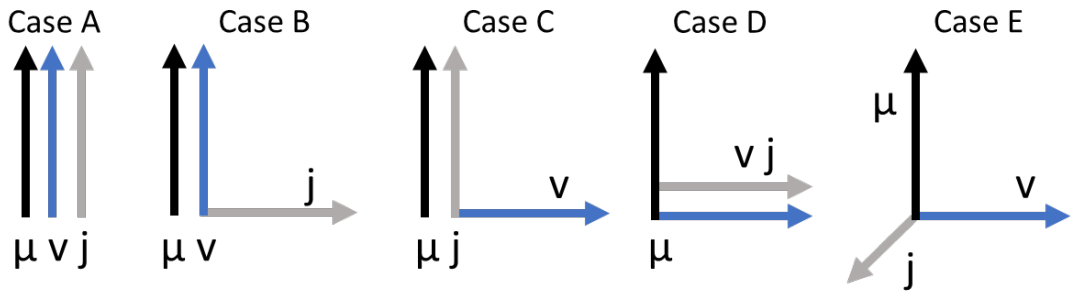

Figure 2.10: Five limiting cases of the relative orientations of the $\boldsymbol{\mu}$, $\boldsymbol{v}$, and $\boldsymbol{j}$ vectors following the semiclassical bipolar moment formalism of Dixon.[91]

all be parallel to each other, two can be parallel and the third can be perpendicular, or they can all be perpendicular to each other. Any non-limiting angles between the vectors should be described as a linear combination of the five limiting cases. Because the relative contributions of all five limiting cases should add up to one, there are four unknown probabilities to determine from the measured angular distributions. The equations of Wei et al. calculate image anisotropy parameters from bipolar moments, and the inverse of the equations are much more complicated than those reported by the authors, so typically forward convolution is used to fit experimental angular distributions rather than direct inversion.[92] In a 2-color experiment, images are collected in three laser geometries (VH, HV, and VV), providing six variables according to Equations 2.4-2.6 to fit four unknowns. Images are often collected for two rotational branches to further constrain the system. Monte Carlo simulations are used to obtain the reported vector correlations and error bars. Random numbers between 0 and 1 are generated for the contribution of each of the five limiting cases and the numbers are normalized so they represent the fraction of the final distribution that each limiting case contributes. For each ratio of the limiting cases, the bipolar moments are calculated and the angular distributions for the three laser geometries are simulated and compared to the experimental angular distributions to obtain a χ^2 value. A threshold χ^2 is set and any randomly generated distributions that are below the threshold are saved along with the corresponding bipolar moments. The reported error bars of the bipolar moments are 2σ where σ is the standard deviation of the saved bipolar moments.

In a 1-color experiment, the images are limited to a single geometry (VV), so the system is underdetermined and quantitative analysis of the angular distributions is limited. However, general conclusions about the dominant limiting case(s) can still be made. Figure 2.11 shows

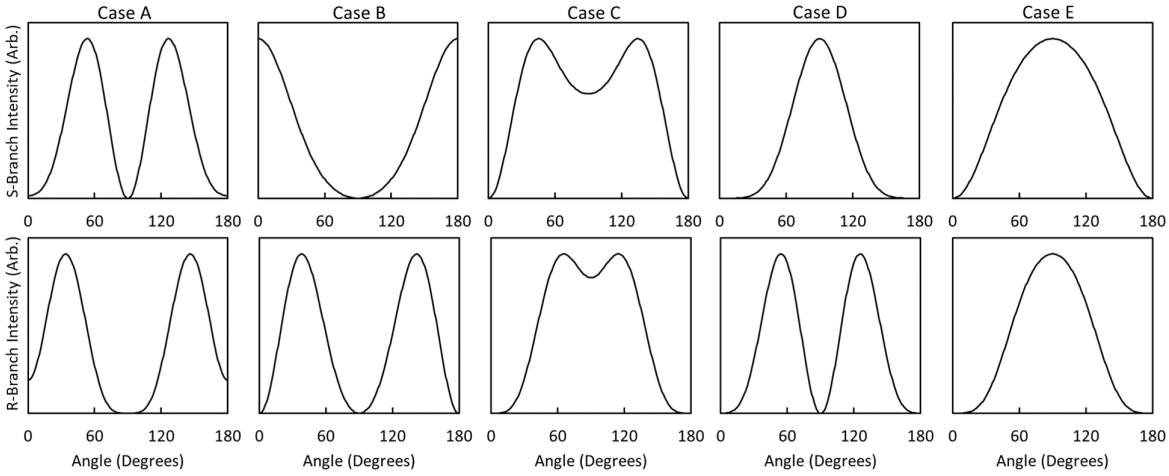

Figure 2.11: Simulated angular distributions for 1-color images collected with a vertically polarized laser in each of the limiting cases (A-E) shown in Figure 2.10. Simulations of S-branch images are shown above and R-branch images below.

simulated S- and R-branch image angular distributions for 1-color images in each of the limiting cases. The angular distributions are clearly very different in each of the cases, so it may be possible to identify which case is dominant in a particular pair of images or if a linear combination of two or three cases results in similar angular distribution to the images collected.

A simple picture of ozone dissociation in the Hartley and Huggins bands is shown in Figure 2.12. Excitation of ground state ozone to the B state is a parallel transition, so $\boldsymbol{\mu}$ and $\boldsymbol{v}$ are expected to be mostly parallel in the molecular plane. The value $\beta_0^2(20)$ may deviate from the limiting value of 1 due to the shape of the potential or a long lifetime of the excited state relative to the rotational period..[4,93] The $\boldsymbol{v}$-$\boldsymbol{j}$ correlation is expected to be perpendicular for the dissociation of a non-rotating triatomic molecule because both the fragment velocity and rotation should remain in the molecular plane of the parent. The $\boldsymbol{v}$-$\boldsymbol{j}$ correlation devi-

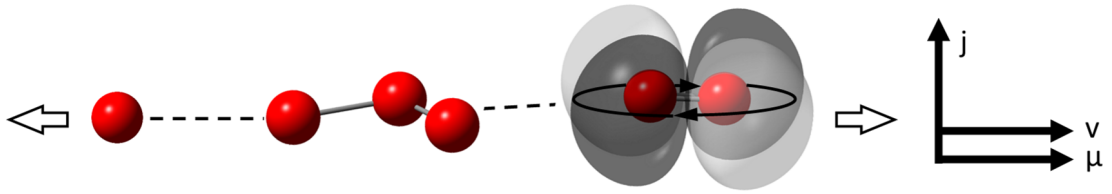

Figure 2.12: Ozone dissociation is expected to be primarily case B, with $\boldsymbol{\mu}$ and $\boldsymbol{v}$ parallel to each other in the plane of the parent molecule and $\boldsymbol{v}$ and $\boldsymbol{j}$ perpendicular to each other.

ates from from its limiting value of -0.5 when there is out-of-plane rotation of the parent molecule. For $\boldsymbol{\mu}$ primarily parallel to $\boldsymbol{v}$ and $\boldsymbol{v}$ primarily perpendicular to $\boldsymbol{j}$ as shown in Figure 2.12, Dixon's limiting case B is expected to be dominant. Vector correlations will be further discussed in Chapters 3 and 4.

2.4 2D-REMPI

REMPI and VMI can be combined into a technique known as 2D-REMPI in which a velocity mapped image is collected at each step in a REMPI spectrum. Schmaunz et al. first used 2D-REMPI to study NO fragments from NO_2 photodissociation by taking images across a wavelength range with narrow wavelength steps to allow enough resolution for the extraction of rotational populations of two vibrational and two electronic states of NO.[94] Since then, 2D-REMPI has been used to study several molecules to obtain wavelength-dependent velocity distributions.[95–101]

A program for collecting 2D-REMPI spectra of the O_2 fragment following O_3 photodissociation was written and used for the Huggins band dissociation experiments discussed in Chapter 4. The program is called Two-dimensional REMPI Application for Collection and Scanning to Unveil Image Trends (TRACSUIT). TRACSUIT controls the laser wavelength

and communicates with the camera. The wavelength step size can be controlled as well as the number of camera shots per step. At each wavelength increment, the specified number of shots are accumulated, and the resulting image is symmetrized and reconstructed. The reconstructed radial distribution is plotted as a function of wavelength in an intensity map. A second program, TrackyDacks, was written to analyze the 2D-REMPI spectra. The spatial resolution of a 2D-REMPI spectrum allows the distinction between rotational distributions of different vibrational and electronic states based on the fragment velocity. TrackyDacks integrates the 2D spectrum over a range of image radii to generate the rotational distribution for fragments traveling a particular speed. The same program can also be used to integrate across wavelengths to produce a speed distribution for a given wavelength range. The front panel of the TrackyDacks program is shown in Figure 2.13. An example 2D-REMPI spectrum is shown on the left. Reconstructed radial distributions for each image collected are plotted as a function of wavelength. The cursors on the 2D spectrum indicate the regions of integration used to obtain the spectra on the right. The top right shows intensity as a function of wavelength for a narrow range of radii, which corresponds to a rotational spectrum of fragments traveling a single speed. The bottom right shows intensity as a function of radius integrated over a narrow wavelength region, corresponding to the reconstructed radial distribution of a wavelength-averaged image.

The 2D-REMPI spectrum in Figure 2.13 was collected in a 2-color experiment following dissociation of O_3 at 226 nm. The intense signal in the spectrum is near 95 pixels, indicating the fragments are largely traveling a single speed. There is additional faint signal near 30 pixels that can be attributed to 1-color signal from 303 nm dissociation. TRACSUIT and TrackyDacks were used to collect and analyze a 2D-REMPI spectrum of O_2 following ozone

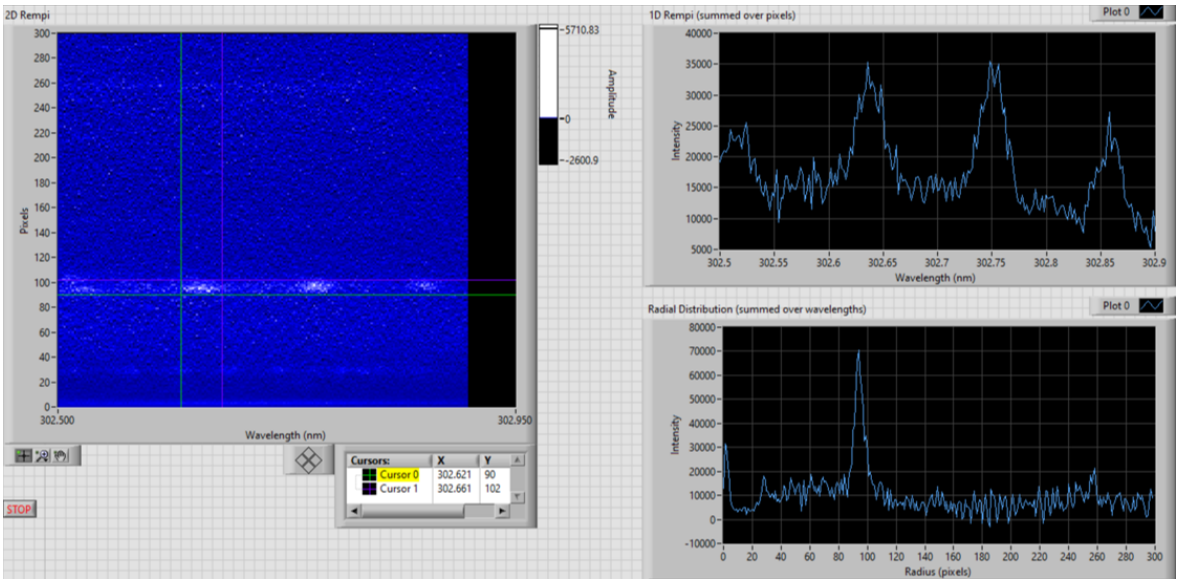

Figure 2.13: The front panel of the TrackyDacks analysis program is shown. The 2D-REMPI spectrum obtained by plotting the radial distribution as a function of wavelength is shown on the left. The rotational spectrum for the radial range indicated by the horizontal cursors is shown in the top right and the radial distribution for the wavelength range indicated by the vertical cursors is shown in the bottom right.

dissociation near 330 nm, which contains fragments traveling multiple speeds, resulting in several horizontal bands of signal across the spectrum. The 330 nm 2D-REMPI spectrum will be discussed in Chapter 4. The spectrum was collected in segments and stitched in a similar way to the 1D spectra. Signal in each segment was integrated across a narrow range of pixels and the resulting 1D spectra were used to scale each segment relative to the others based on overlapping peaks. The overlapping regions were averaged. Background correction was performed by integrating a region of the 2D spectrum without signal over the same width of pixels as the integrated 1D spectrum, fitting the background spectrum with a 3rd order polynomial, and subtracting the fit from the spectrum of data.

2.5 Modeling Linewidths

As discussed above, there are several contributions to the linewidths observed in a REMPI spectrum. Because Doppler broadening is negligible for O_2 following O_3 photodissociation in the Hartley and Huggins bands, power and lifetime broadening are dominant. While power broadening as a result of high laser power affects all the peaks in the spectrum relatively uniformly,[102] lifetime broadening is highly dependent on the vibrational and rotational state of the spectrum.[75,76] As discussed above, O_2 in the $a^1\Delta_g$ and $b^1\Sigma_g^+$ states are excited to the $d^1\Pi_g$ state in 2+1 REMPI schemes between 300 and 330 nm. In addition to the perturbations in low vibrational levels of the $d^1\Pi_g$ Rydberg state, the $II^1\Pi_g$ valence state causes predissociation from the $d^1\Pi_g$ state. Greater wavefunction overlap between the Rydberg and valence states increases the transition probability, which corresponds to increasing predissociation rates and decreasing lifetime. Following the energy-time uncertainty principle, faster predissociation rates will lead to broader spectral linewidths. The wavefunction overlap varies significantly across vibrational and rotational states, leading to highly variable linewidths.

The Bound-Continuum (BCONT) program written by Le Roy and Kraemer calculates transition rates between a bound state and the continuum of another state, which can be used to determine predissociation lifetimes and linewidths.[103] The program calculates eigenvalues and the corresponding wavefunctions for given potentials and determines the wavefunction overlap for specified vibrational and rotational states of the bound state, taking into account the coupling between the two states. The potentials and the coupling between them can be adjusted to reproduce predissociation rates that are consistent with experimentally measured linewidths. The potentials can then be used to predict rotational state dependent linewidth trends that have not yet been studied experimentally. The calculated linewidth trends and the potentials used to calculate them will be discussed in Chapter 5.

3. HARTLEY BAND PHOTODISSOCIATION

3.1 Previous Studies on O_3 Dissociation in the Hartley Band

Light between 200 and 300 nm dominates stratospheric ozone photochemistry and as a result, Hartley band dissociations have been extensively studied, including several studies on the dominant singlet channel. Specifically, the wavelength dependence of the $O(^1D)$ spatial anisotropy parameter (β) and the $O_2(a^1\Delta_g)$ rotational distribution have been studied between 235 and 298 nm.[4,6,7,10,12,47] The alternation between the even and odd rotational states of $O_2(a^1\Delta_g)$ initially attributed to selective curve-crossing of the odd rotational states to the R state has recently been shown to result instead from a Λ-doublet propensity.[6,47] This is consistent with the observed temperature, wavelength, and vibrational state dependence of the alternation and has implications for modeling isotopic enrichment. The curve-crossing model predicts differences in the branching ratio between the singlet and triplet channels for different isotopes of O_3 but the Λ-doublet model does not. Although no experimental measurements of the branching ratios of isotopically substituted O_3 have been made to our knowledge, calculations predict the same branching ratio for all isotopes, consistent with the Λ-doublet model.[43]

The Hartley absorption band extends from 200 to 300 nm, so extending studies of the $O_2(a^1\Delta_g)$ fragment to shorter wavelengths than previous studies allows assessment of a higher energy portion of the B state potential and accesses higher rotational states than lower energy dissociations. There have also been studies on ozone dissociation at higher energies than the Hartley band, such as 193 nm.[50,104–107] At this wavelength, additional electronic states of ozone are energetically accessible in the initial absorption and previous studies have

reported evidence for additional product channels, including triple dissociation to form three O atoms. The β parameter for most channels at these wavelengths is negative, indicative of a perpendicular transition in contrast to the parallel transition to the B state in the Hartley band.

Imaging studies of ozone dissociation in the triplet channel have previously been performed at 226 nm because the absorption cross section of ozone is large at this wavelength and there is a 2+1 REMPI scheme to probe the atomic O fragment ($3p\ ^3P_j \leftarrow\leftarrow\ 2p\ ^3P_j$). Therefore, 1-color experiments can be performed without the need for separate photolysis and probe lasers. Early images of the O(^3P) fragment revealed a bimodal speed distribution, which was initially attributed to a bimodal vibrational state distribution in the $O_2(X^3\Sigma_g^-)$ fragment with peaks assigned to v=14 and v=27.[8,55] The highly vibrationally excited O_2 products were thought to be an additional source of ozone formation, which would partially explain the ozone deficit problem. This initial assignment of the slow O(^3P) fragments prompted many additional studies of O_3 photodissociation at 226 nm.[4,19,56–59] A more recent study has instead attributed the slow O(^3P) fragments to dissociations that form the O_2 co-fragment in Herzberg states ($A'\ ^3\Delta_u$ and $A\ ^3\Sigma_u^+$) with higher electronic energy rather than high vibrational levels of the ground electronic state.[48] The energy of the Herzberg states is consistent with the observed speed of the O(^3P) fragments, but the Herzberg states of O_2 have not been studied directly.

Despite the numerous studies of O_3 dissociation at 226 nm, the singlet channel has not been previously studied at this wavelength, and the singlet channel studies have not been extended to the high energy region of the Hartley band.

3.2 $O_2(a^1\Delta_g)$ Rotational Distribution at 226 nm

A REMPI spectrum of the $O_2(a^1\Delta_g)$ fragment following O_3 dissociation at 226 nm is shown in Figure 3.1. The O_2 fragment is probed near 303 nm with 2+1 REMPI via the 4-0

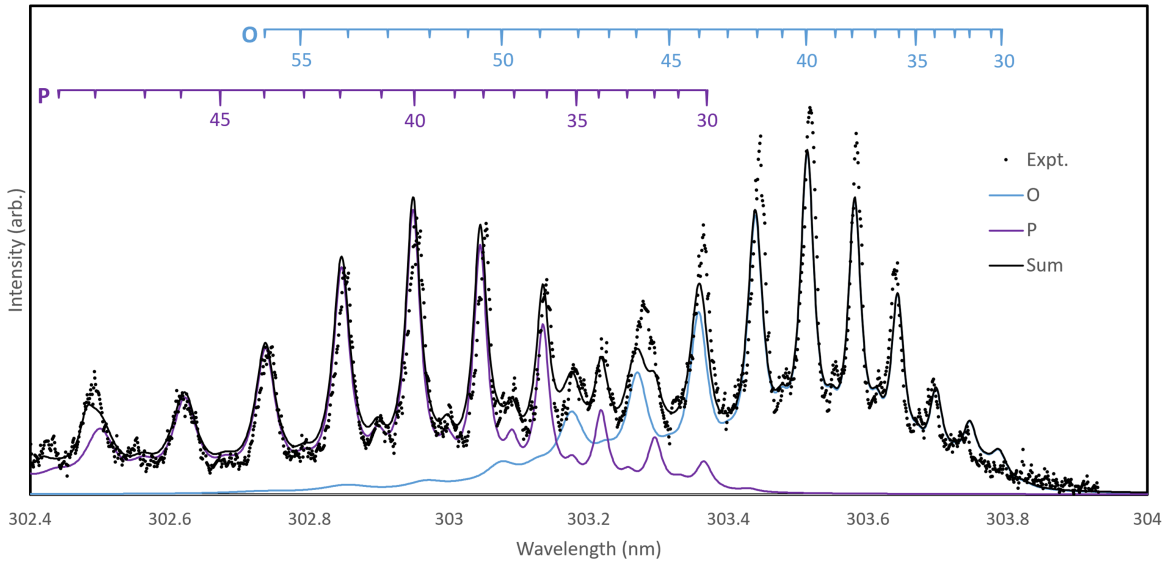

Figure 3.1: O_2 REMPI spectrum following 226 nm dissociation of O_3 probed via the $O_2(d^1\Pi_g, v = 4 \leftarrow\leftarrow a^1\Delta_g, v = 0)$ transition. The black circles are experimental data and the simulated O and P branches used to fit the spectrum are shown in blue and purple, respectively. The solid black line represents the sum of the branches. Reprinted with permission from Aardema et al. *J. Phys. Chem. A* 2022, 126, 39, 6898-6907. Copyright 2022 American Chemical Society.

band of the $O_2(d^1\Pi_g \leftarrow\leftarrow a^1\Delta_g)$ transition. The experimental data is shown by the black circles, the O and P branches are shown by the blue and purple lines, respectively, and the sum of the branches is shown by the solid black line. The rotational state transitions corresponding to each peak are indicated by the comb at the top, and it is clear the odd rotational

states are highly suppressed as observed in previous studies in the Hartley band.[6,7,12,47] The simulation used to fit the spectrum uses Lorentzian functions at each transition energy with adjustable linewidths and populations. The linewidths employed are j-dependent and will be discussed in Chapter 5.

The rotational state populations and error bars obtained from fitting the spectrum using Monte Carlo simulation are shown in black in Figure 3.2. The solid blue line represents

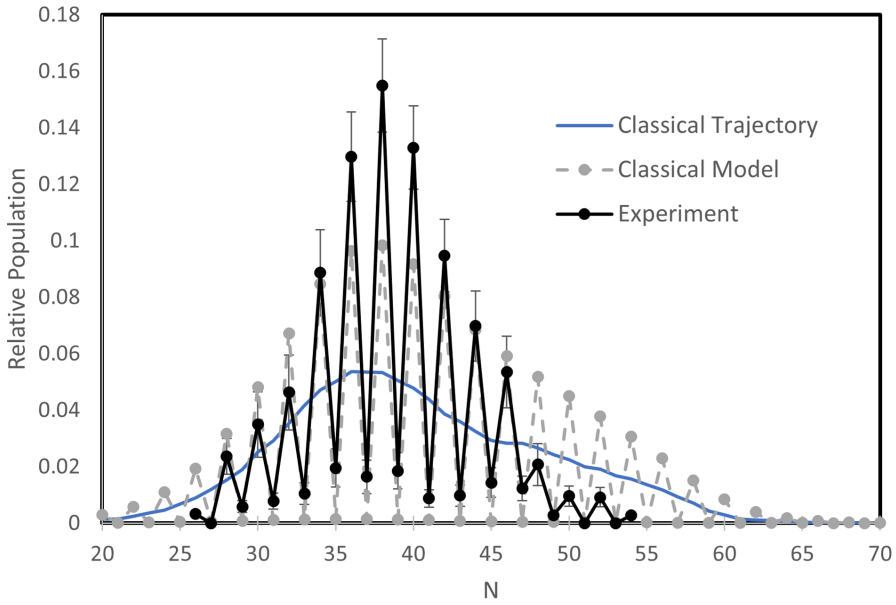

Figure 3.2: The rotational state populations fit to the REMPI spectrum in Figure 3.1 are shown in black. The rotational state distribution calculated by classical trajectory calculations is shown in blue. The grey populations represent the calculated distribution depolarized using the classical model of Gunthardt et al.[47] Reprinted with permission from Aardema et al. *J. Phys. Chem. A* 2022, 126, 39, 6898-6907. Copyright 2022 American Chemical Society.

the rotational state distribution predicted by classical trajectory calculations, and the gray

circles indicate the calculated populations depolarized by the classical model of Gunthardt et al. for a 70 K distribution of O_3 parent molecules.[47] The classical model takes into account O_3 rotation and the Λ-doublet propensity that leads to greater population in even rotational states. The O_3 parent is treated as an asymmetric top, and all possible combinations of J_A, J_B, and J_C are considered with weighting factors following a Boltzmann distribution. The angle between the resulting O_2 angular momentum and the rotation axis perpendicular to the original molecular plane represents the extent of depolarization resulting from O_3 out-of-plane rotation and can be used to determine the fraction of each Λ-doublet contributing to each O_2 rotational state. The O_2 populations are scaled by the A′ and A″ fractions to obtain the final rotational state distribution. The classical model overpredicts the suppression of the odd rotational states as previously reported by Gunthardt et al.[47]

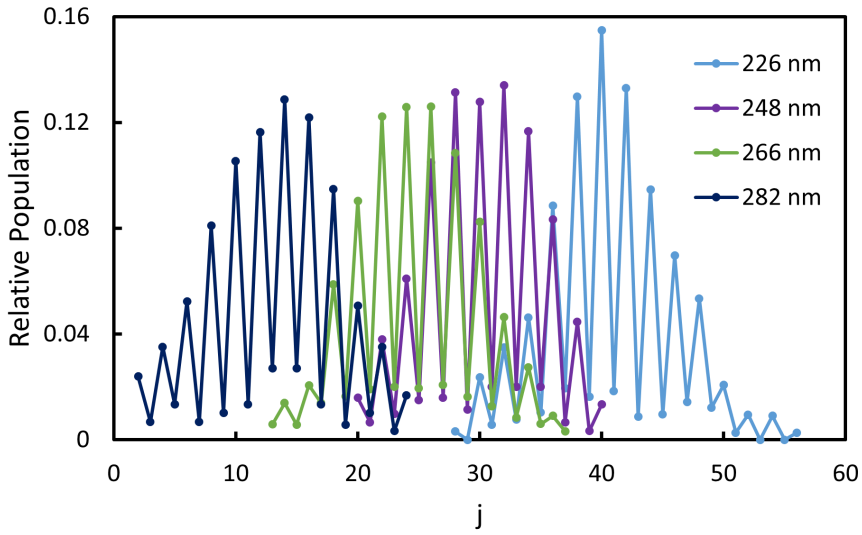

Figure 3.3: The rotational distributions of $O_2(a^1\Delta_g, v = 0)$ following O_3 dissociation at 226, 248, 266 and 282 nm are shown in light blue, purple, green, and dark blue, respectively.[6,12,47]

In comparison to the rotational state distribution measured at longer wavelengths, the rotational distribution is shifted to higher rotational states following dissociation at 226 nm. Figure 3.3 shows the rotational distributions following dissociation at 226 nm (light blue), 248 nm (purple), 266 nm (green), and 282 nm (dark blue).[6,12,108] The measured rotational distribution following 226 nm is consistent with the trend observed at longer wavelengths. The suppression of the odd rotational states, $S(j_{odd})$, can be quantified with the equation

$$S(j_{odd}) = \frac{P(j_{even}) - P(j_{odd})}{P(j_{even})} \tag{3.1}$$

where $P(j_{odd})$ is the population of the odd rotational states and $P(j_{even})$ is the average population of the two even states adjacent to the odd rotational state.[47] The odd rotational states will have the greatest suppression in the center of the distribution because fragments in rotational states at the edges of the distribution come from the warmest parent molecules. This trend can be seen in Figure 3.4 where $S(j_{odd})$ is plotted as a function of j for the rotational state distribution measured for a 226 nm dissociation. The low suppression at j=49 corresponds to a decrease in population between j=48 and j=50, but a similarity in the populations of j=47 and j=49. This results in less calculated suppression in j=49 than nearby odd rotational states. For a 266 nm dissociation, the suppression of the odd states at the peak of the distribution is 0.83, and for a 226 nm dissociation the suppression is 0.88. The difference is subtle, but the increase in odd state suppression is consistent with the Λ-doublet model which predicts greater alternation at higher energy dissociations because small amounts of out-of-plane O_3 motion will be less significant at higher rotational states.

The envelope of the experimental rotational distribution largely matches the calculated distribution for dissociation at 226 nm, but the calculated distribution contains a shoulder

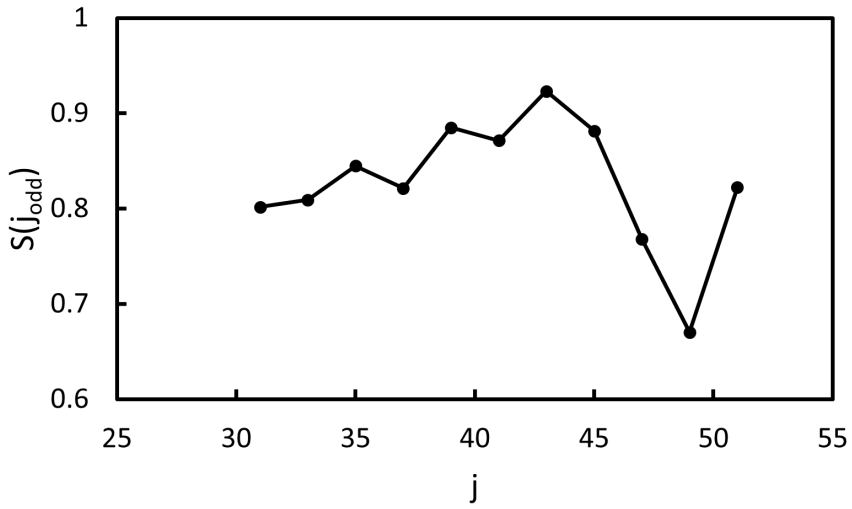

Figure 3.4: The suppression of the odd rotational states in the 226 nm rotational state distribution calculated with Equation 3.1 are shown as a function of j. The suppression is highest in the middle of the rotational state distribution and decreases at both low and high rotational states.

around N=45 with higher populations at higher rotational states. This is the first deviation between measured and calculated distributions seen for Hartley band dissociation of O_3. The REMPI spectrum shown in Figure 3.5 was simulated using the populations calculated with the classical model. The calculated populations lead to underprediction of the intensity around 303.5 nm, which corresponds to moderate rotational states in the O branch. The intensity is overpredicted at shorter wavelengths near 302.5 nm, which corresponds to high rotational states in the P branch. The deviations between the simulation and data are more significant when the rotational state distribution includes the shoulder at high rotational states, indicating the shoulder at high rotational states is not present in the experimental spectrum.

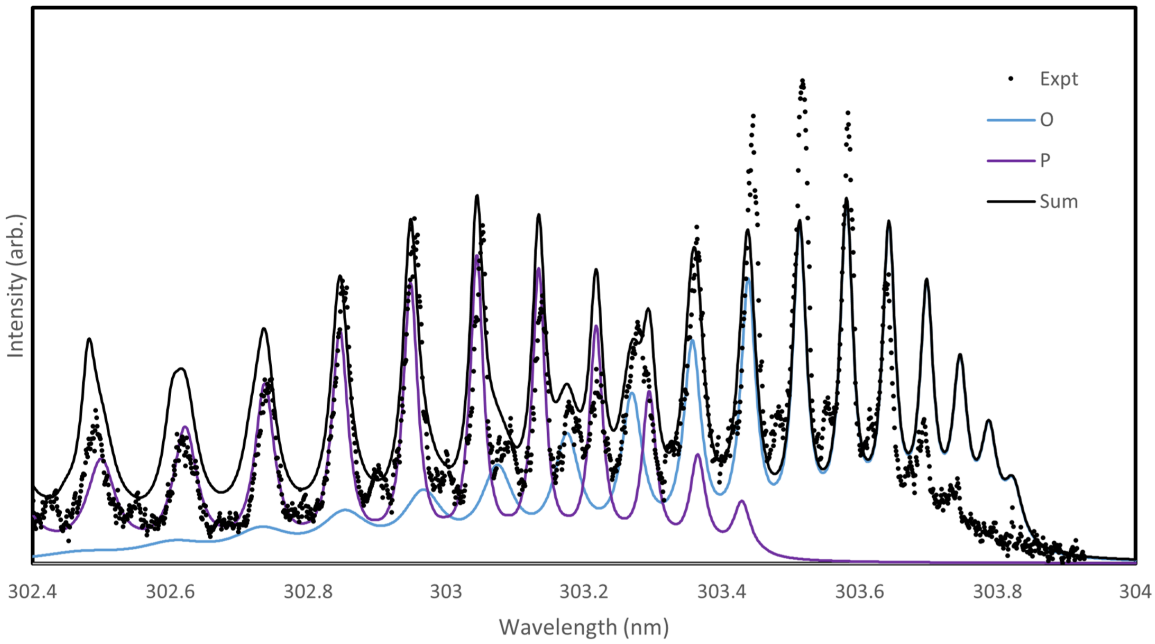

Figure 3.5: The experimental REMPI spectrum in Figure 3.1 is shown in black circles and fit with a simulation using the populations obtained by depolarizing the rotational state distribution calculated by classical trajectories. The O branch is shown in blue, the P branch is shown in purple, and the sum of the branches is shown by the solid black line. Reprinted with permission from Aardema et al. *J. Phys. Chem. A* 2022, 126, 39, 6898-6907. Copyright 2022 American Chemical Society.

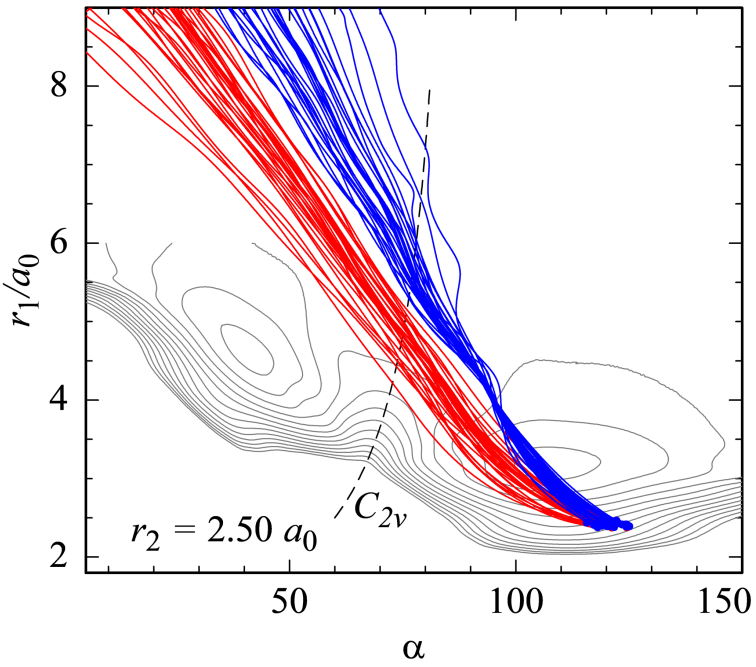

Figure 3.6: Trajectories on the potential energy surface of the B state of O_3. The blue trajectories begin with no momentum, and the red trajectories begin with initial momentum that decreases the bond angle. The red trajectories result in higher rotational states of the O_2 fragment than the blue trajectories. Reprinted with permission from Aardema et al. *J. Phys. Chem. A* 2022, 126, 39, 6898-6907. Copyright 2022 American Chemical Society.

The origin of the high rotational state shoulder in the calculated distribution is not clear. Figure 3.6 shows two sets of trajectories. The trajectories shown in blue begin with no momentum. The trajectories shown in red are trajectories that result in high rotational states which all begin with initial momentum corresponding to decreasing bond angle. The difference between the final O_2 rotational states between these two sets of trajectories suggests the potential may be too weak at small bond angles, resulting in less deflection of the red trajectories back toward the blue trajectories. The wavelength-dependent trend in anisotropy parameters, however, suggests too strong a potential.

3.3 $O_2(a^1\Delta_g)$ Vector Correlations at 226 nm

Ion images of the $O_2(a^1\Delta_g; v = 0, j = 38)$ fragment were collected in three geometries (VV, HV, and VH) following O_3 dissociation at 226 nm, probed via O and P branch transitions. The signal in the center of the images is 1-color signal from 303 nm dissociation of O_3. Dissociation at 303 nm is lower energy than 226 nm, so the fragments appear at smaller radii in the images. The outer ring was used to obtain the angular distributions shown in Figure 3.8. The intensity at the top and bottom of the images is indicative of a parallel $\boldsymbol{\mu}$-$\boldsymbol{v}$ correlation as expected for a transition from the ground state of O_3 to the B state. The 4-fold symmetry in the P-branch VV and HV images indicates a perpendicular $\boldsymbol{v}$-$\boldsymbol{j}$ correlation as expected for a triatomic dissociation. The image anisotropy parameters can be fit to the equations of Wei et al. to extract bipolar moments through forward convolution.[92] The resulting bipolar moments and error bars were obtained through Monte Carlo simulation of the angular distributions.

Following Dixon's bipolar moment formalism, the low order bipolar moments, $\beta_0^2(20)$, $\beta_0^2(02)$ and $\beta_0^0(22)$ correspond to the expectation value of the second Legendre polynomial,

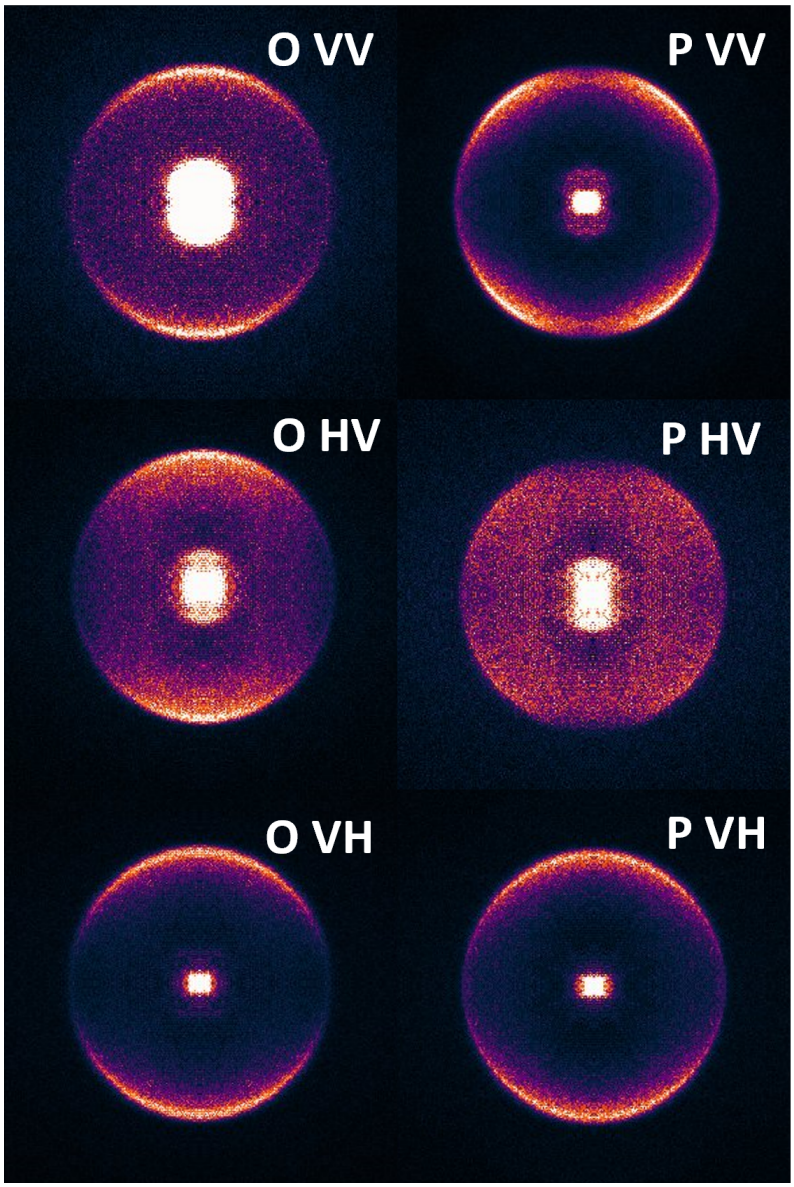

Figure 3.7: Ion images of $O_2(a^1\Delta_g; v = 0, j = 38)$ produced from the 226 nm dissociation of jet-cooled O_3. Fragments were probed via O- and P-branch transitions of the $O_2(d^1\Pi_g, v = 4 \leftarrow\leftarrow a^1\Delta_g, v = 0)$ transition. O-branch images are shown on the left and P-branch images on the right. VV, HV, and VH indicate the polarization of the photolysis and probe lasers. Reprinted with permission from Aardema et al. *J. Phys. Chem. A* 2022, 126, 39, 6898-6907. Copyright 2022 American Chemical Society.

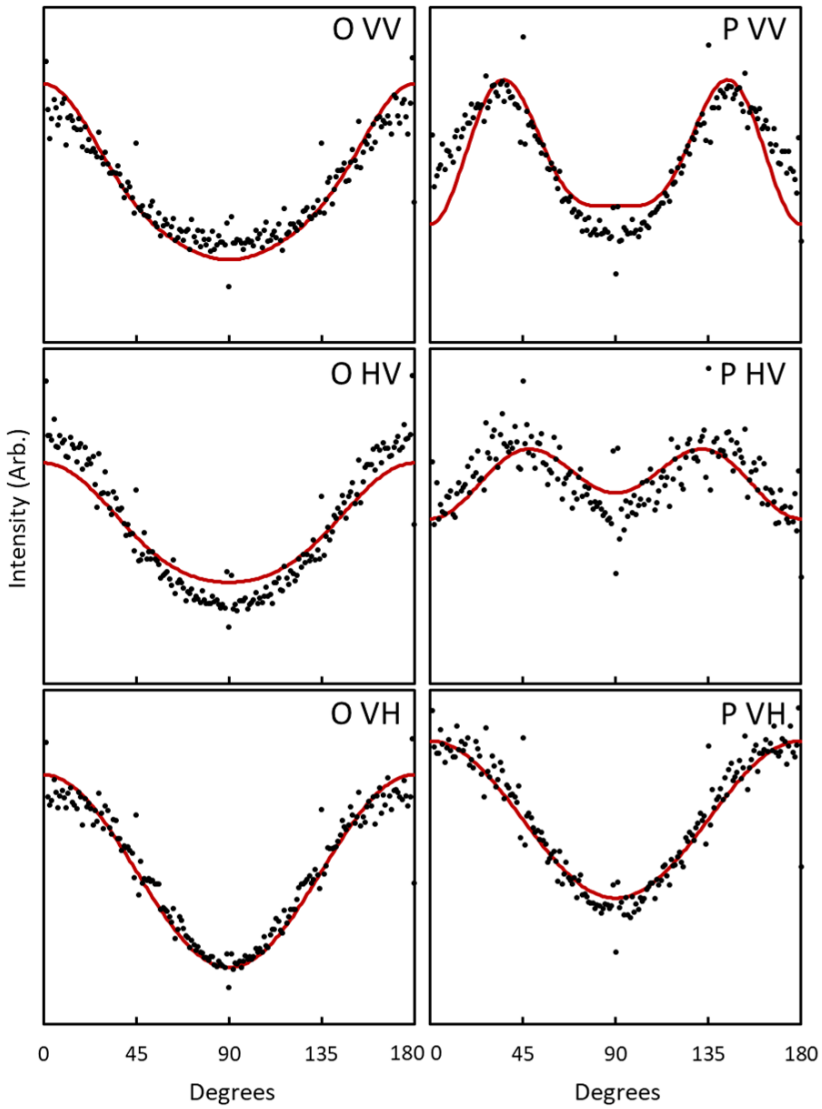

Figure 3.8: Angular distributions corresponding to the outer ring of the images shown in Figure 3.7. Angular distributions for O-branch images are shown on the left and P-branch images on the right. VV, HV, and VH indicate the polarization of the photolysis and probe lasers. The black circles indicate the experimental angular distribution and the solid red lines indicate the fits to the distributions. Reprinted (adapted) with permission from Aardema et al. *J. Phys. Chem. A* 2022, 126, 39, 6898-6907. Copyright 2022 American Chemical Society.

Bipolar Moment	Experimental Value
$\beta_0^2(20)$	0.36 ± 0.07
$\beta_0^2(02)$	-0.32 ± 0.17
$\beta_0^0(22)$	-0.18 ± 0.14
$\beta_0^2(22)$	-0.14 ± 0.12
$\beta_0^2(24)$	0.27 ± 0.06
$\beta_0^2(44)$	0.001 ± 0.11
$\beta_0^0(44)$	0.16 ± 0.11
$\beta_0^2(42)$	-0.13 ± 0.13
$\beta_0^2(64)$	0.21 ± 0.07

Table 3.1: Bipolar moments obtained from Monte Carlo simulation using forward convolution to fit the image angular distributions in Figure 3.8.

$\langle P_2(cos\theta)\rangle$, where θ is the angle between the two vectors of interest. The values for $\beta_0^2(20)$, $\beta_0^2(02)$ and $\beta_0^0(22)$ in Table 3.1 represent an average $\boldsymbol{\mu}$-$\boldsymbol{v}$ angle of 41°, a $\boldsymbol{\mu}$-$\boldsymbol{j}$ angle of 70°, and a $\boldsymbol{v}$-$\boldsymbol{j}$ angle of 62°. This is consistent with $\boldsymbol{\mu}$ parallel to $\boldsymbol{v}$ and $\boldsymbol{v}$ perpendicular to $\boldsymbol{j}$, indicating case B is dominant as expected. The values of $\beta_0^2(02)$ and $\beta_0^0(22)$ following 226 nm dissociation are similar to the values reported by Gunthardt et al. for a 266 nm dissociation.[47] For j=18 following a 266 nm dissociation at 70 K, $\beta_0^2(02)$ is -0.35$\pm$0.08 and $\beta_0^0(22)$ is -0.32$\pm$0.08. The value of $\beta_0^2(20)$ measured at 226 nm is lower than the value of 0.63$\pm$0.02 measured at 266 nm.

The wavelength dependence of the $\beta_0^2(20)$ (where $\beta_0^2(20)$=$\frac{1}{2}\beta$) was previously studied between 235 and 298 nm, and is now extended to 226 nm. Figure 3.9 shows the values of $\beta_0^2(20)$ calculated with classical trajectories for $O_2(a^1\Delta_g, v = 0)$ from McBane et al. in gray,[4] and the experimentally measured $\beta_0^2(20)$ values from Dylewski et al. for

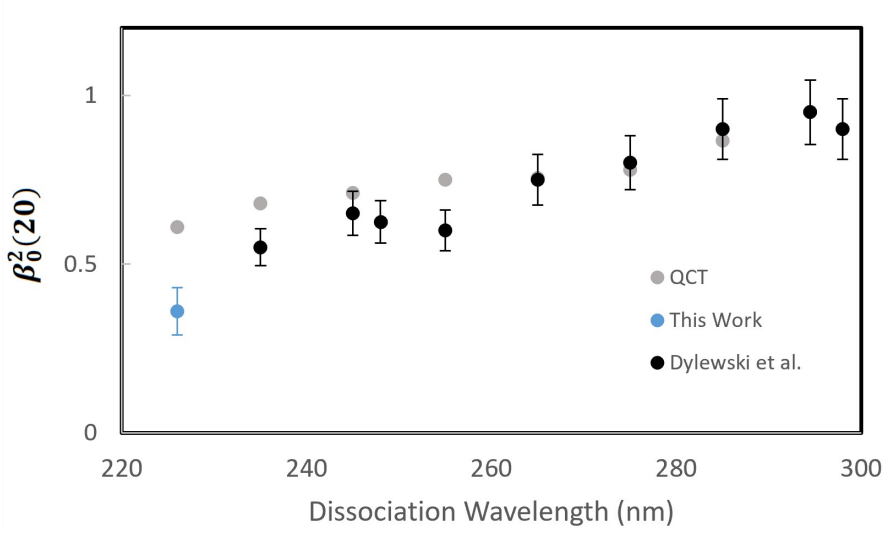

Figure 3.9: The values of $\beta_0^2(20)$ calculated by classical trajectory calculations from McBane et al. are shown in gray.[4] The experimental values of $\beta_0^2(20)$ obtained from O(^1D) images by Dylewski et al. are shown in black.[10] The value shown in blue is the experimentally measured $\beta_0^2(20)$ for $O_2(a^1\Delta_g; v = 0, j = 38)$ following 226 nm dissociation. Reprinted with permission from Aardema et al. *J. Phys. Chem. A* 2022, 126, 39, 6898-6907. Copyright 2022 American Chemical Society.

$O(^1D)$ images in black.[10] The blue data point indicates the experimental measurement of $O_2(a^1\Delta_g; v = 0, j = 38)$ following 226 nm dissociation. The experimental measurements of $\beta_0^2(20)$ are consistent with the calculated values at longer wavelengths, but the deviation between experiment and theory increases with decreasing wavelength. At shorter wavelengths the classical trajectory calculations overpredict the value of $\beta_0^2(20)$. When O_3 is excited from the X state to the B state, the equilibrium bond angle decreases from 117° to 107°. When the bond angle continues to decrease below 107°, the molecule experiences a restoring force, causing the bond angle to increase again. The decrease in bond angle causes the direction of the fragment velocity to move away from the direction of $\boldsymbol{\mu}$, and the restoring force causes the fragment velocity to move back towards $\boldsymbol{\mu}$.[4,10] The average angle between $\boldsymbol{\mu}$ and $\boldsymbol{v}$ is dependent on the dissociation wavelength because the amount of available energy will influence the recoil velocity and the amount of time the molecule spends in the excited state. At longer dissociation wavelengths, the recoil velocity is slower, the molecule has increased time to experience the restoring force, and the resulting fragment velocity is closer to the direction of $\boldsymbol{\mu}$, as seen in Figure 3.9. McBane et al. have attributed the deviation at shorter dissociation wavelengths to the bending potential being too strong at large O-O_2 distances, which would result in a stronger restoring force and overprediction of $\beta_0^2(20)$.

The value of $\beta_0^2(20)$ is calculated to be 0.605 averaged over rotational states in v=0, and 0.705 for v=0, j=38. In addition to the decreasing bond angle following excitation to the B-state, translational and rotational motion of the parent molecule during the excited state lifetime can also lead to weaker $\boldsymbol{\mu}$-$\boldsymbol{v}$ correlations which can be estimated following the model of Busch and Wilson.[93] For a 70 K distribution of O_3, the depolarized $\beta_0^2(20)$ for $O_2(a^1\Delta_g; v = 0, j = 38)$ is estimated to be 0.67, which is still higher than the observed

value of 0.36. However, the wavelength-dependent trend is consistent between experiment and theory, and the increased deviation at 226 nm is consistent with previous results.

While the depolarization of the $\boldsymbol{\mu}$-$\boldsymbol{v}$ correlation depends on the excited state lifetime, the $\boldsymbol{v}$-$\boldsymbol{j}$ correlation is independent of lifetime. The value of $\beta_0^0(22)$ is, however, also dependent on the translation and rotation of the parent molecule. The value of $\beta_0^0(22)$ following the dissociation of a non-rotating triatomic molecule is expected to be -0.5, corresponding to a perpendicular $\boldsymbol{v}$-$\boldsymbol{j}$ correlation, but out-of-plane motion of the parent molecule can decrease the angle between $\boldsymbol{v}$ and $\boldsymbol{j}$, resulting in $\beta_0^0(22)$ diminished from its limiting value of -0.5. Depolarization from parent thermal velocity can be accounted for by modified spherical Bessel functions,[109–112] and depolarization from parent internal motion can be described by the model of Busch and Wilson.[93] The depolarized v-j correlation as a function of N is shown in Figure 3.10 calculated with the classical model of Gunthardt et al., where the open circles indicate even rotational states and the closed circles indicate odd rotational states.[47] Deviation from the limiting value of $\beta_0^0(22)$=-0.5 is expected to be greater for odd rotational states because odd states result from a distribution of O_3 molecules with greater out-of-plane motion and at rotational states at the edges of the distribution which require greater parent rotation to result in a final fragment rotational state that differs from the 0 K calculated distribution. The deviation is expected to be greater at low rotational states where contributions from parent out-of-plane motion are more significant. Based on these models, depolarization of the $\boldsymbol{v}$-$\boldsymbol{j}$ correlation is expected to be minor for N=36. The value of $\beta_0^0(22)$ is predicted to be -0.48 for $O_2(a^1\Delta_g; v = 0, j = 38)$, which is stronger than the observed value of -0.18. The experimental value may be closer to zero than predicted because the REMPI peak for the P-branch transition N=36 (j=38) is overlapped with intensity from

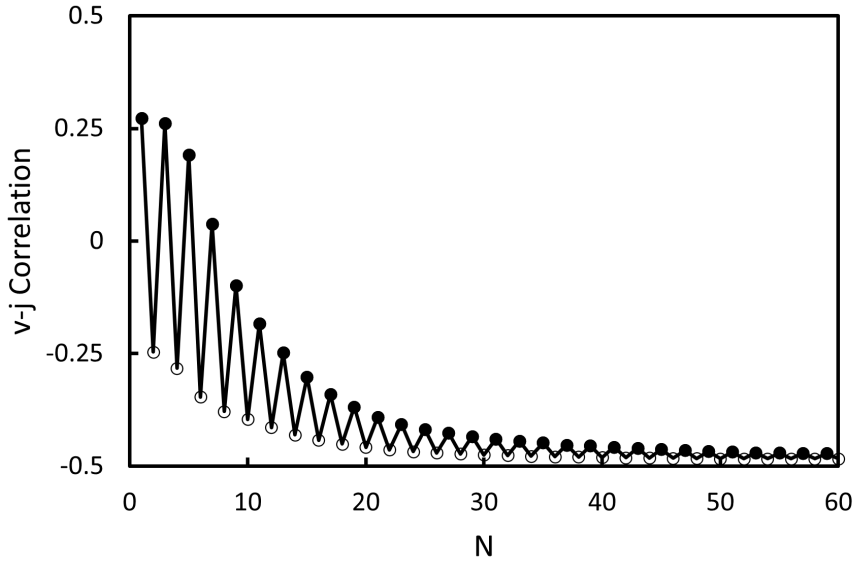

Figure 3.10: Calculated values of $\beta_0^0(22)$ as a function of N using the classical model of Gunthardt et al., which takes into account depolarization due to initial motion of the parent O_3 molecules.[47] The even rotational states are represented by open circles and the odd rotational states by closed circles.

high rotational states in the O branch, but the experimental value is consistent with previous measurements of $\beta_0^0(22)$ for O_2 following O_3 dissociation between 248 and 300 nm which range between -0.4 and -0.2.[113–117] Vector correlations were only obtained for j=38 following 226 nm dissociation, but the values of $\beta_0^0(22)$ were shown by Gunthardt et al. to be closer to zero for odd rotational states than even rotational states, due to greater depolarization resulting from a warmer distribution of O_3 and a decreased angle between $\boldsymbol{v}$ and $\boldsymbol{j}$.[47]

4. HUGGINS BAND PHOTODISSOCIATION

4.1 Previous Studies on O_3 Dissociation in the Huggins Band

Previous studies on the Huggins band dissociation of ozone have included time-of-flight studies on both the $O(^1D)$ and $O_2(a^1\Delta_g)$ fragments which have demonstrated speeds consistent with dissociation via a spin-forbidden channel. Based on the speed distribution of the $O(^3P_0)$ fragment, O'Keeffe et al. concluded the branching ratio between the spin-allowed channel forming $O(^3P)$ with $O_2(X^3\Sigma_g^-)$ and the spin-forbidden channels forming $O(^3P)$ with $O_2(a^1\Delta_g)$ and $O_2(b^1\Sigma_g^+)$ was equal following 322.64 nm dissociation of O_3.[61] Ulrich et al. collected ion images of $O(^3P_2)$ following O_3 dissociation between 321 and 329 nm, and reported the total kinetic energy distributions of the fragments at each dissociation wavelength.[71] The authors also concluded there is approximately equal branching between the three channels forming $O(^3P)$. REMPI spectra of $O_2(b^1\Sigma_g^+)$ probed via the 1-0 band of the $O_2(d^1\Pi_g \leftarrow\leftarrow b^1\Sigma_g^+)$ transition were reported following O_3 dissociation at 337.2 and 344 nm by O'Keeffe et al.[73] The REMPI scheme utilized by the authors accesses a perturbed vibrational level of the resonant $O_2(d^1\Pi_g)$ state, but the authors reported rotational state distributions of $O_2(b^1\Sigma_g^+, v = 0)$, adjusting populations for the perturbations. The reported rotational state distributions peak at j=34 and j=28 for dissociation at 337.2 and 344 nm, respectively. In this chapter, additional experiments on the spin-forbidden channels are discussed, probing the $O_2(b^1\Sigma_g^+)$ fragment with unperturbed vibrational levels of the $O_2(d^1\Pi_g)$ state and studying the $O_2(a^1\Delta_g)$ fragment rotational state distribution through ion image speed distributions and REMPI.

4.2 $O_2(a^1\Delta_g)$ Even-Odd Alternation at 320 nm

While REMPI spectra of the $O_2(b^1\Sigma_g^+)$ fragment have been previously reported, the rotational state distribution of the $O_2(a^1\Delta_g)$ fragment has not been directly measured below the energetic threshold of the spin-allowed singlet channel despite the interest in the even-odd alternation observed at higher energies. The even rotational states of $O_2(a^1\Delta_g)$ have greater population in the Hartley band because of a Λ-doublet propensity in which there is a preference for the orbital of the O_2 fragment to be oriented in the molecular plane to conserve the A′ symmetry of the parent O_3.[6,47] The A′ Λ-doublet must correspond to even rotational states due to symmetry restrictions. If the molecular orbital is instead oriented perpendicular to the molecular plane, the symmetry is A″, which must correspond with odd rotational states. In a non-rotating molecule, the A′ and A″ Λ-doublets are degenerate, but there is a preference to conserve the parent A′ symmetry.

The alternation between even and odd rotational states of $O_2(a^1\Delta_g)$ was shown by Gunthardt et al. to be temperature dependent, with greater alternation at lower temperatures.[47] In the parent ozone molecule, there are three axes of rotation: two in the molecular plane and one perpendicular to the plane. The angular momentum of the O_2 fragment contains components along all three axes, but at low temperatures, the O_2 rotation remains primarily in the initial plane of the parent O_3. As the temperature increases, rotation around the two in-plane axes causes the fragment O_2 rotation plane to tilt relative to the initial plane, breaking the symmetry restrictions. This causes greater mixing of the Λ-doublets and results in less alternation between the intensity of even and odd rotational states at higher temperatures. In the previous study of the temperature dependence of the alternation, the $O_2(d^1\Pi_g, v = 2 \leftarrow\leftarrow a^1\Delta_g, v = 0)$ REMPI transition was used to probe the $O_2(a^1\Delta_g)$ frag-

ment following 266 nm dissociation of O_3. The perturbations of the v=2 level of the resonant state cause increased intensity of the odd rotational states in the S and R branches, making differences in the alternations at different temperatures easier to identify.

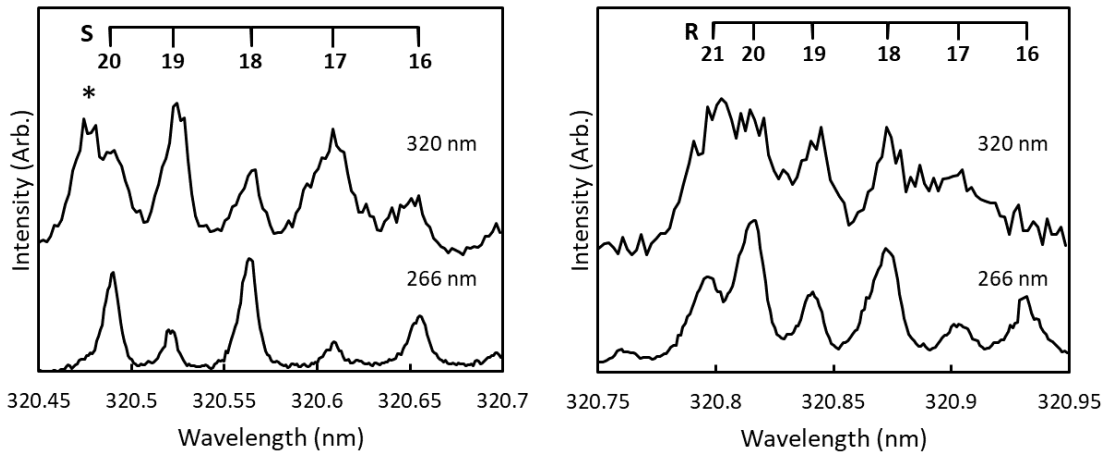

Figure 4.1: S-branch (left) and R-branch (right) transitions of $O_2(a^1\Delta_g)$ following dissociation of O_3, probed via the $O_2(d^1\Pi_g, v = 2 \leftarrow\leftarrow a^1\Delta_g, v = 0)$ transition. The top spectra are 1-color experiments, and the bottom spectra are 2-color experiments with O_3 photodissociation at 266 nm.[47] Rotational states of the transitions are indicated by the combs at the top. The peak marked by * indicates the P-branch transition of j=42.

Figure 4.1 compares the S and R branches of the $O_2(a^1\Delta_g)$ fragment following O_3 dissociation near 320 nm in a 1-color experiment (top) and following 266 nm dissociation in a 2-color experiment (bottom) reported by Gunthardt et al.[47] In the 266 nm spectra, the even rotational states are enhanced due to a preference for the formation of the A′ Λ-doublet which corresponds to even rotational states, but in the 320 nm spectra, the odd states are enhanced despite the cold temperature of 50 K. Although the experiment used a single laser for both

the photolysis and the probe, the enhanced odd states are not consistent with peaks in the absorption spectra of O_3, as shown in Figure 4.2. The 2-0 REMPI of O_2 probed via the

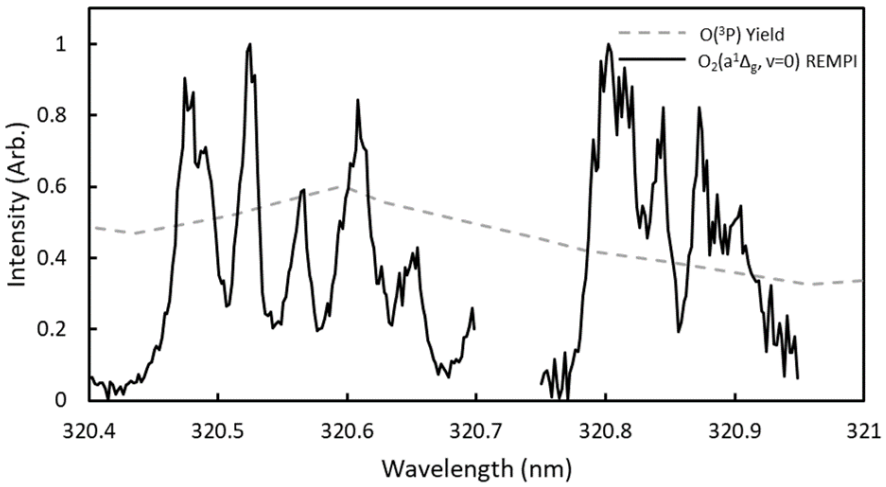

Figure 4.2: The $O_2(d^1\Pi_g, v = 2 \leftarrow\leftarrow a^1\Delta_g, v = 0)$ REMPI spectra from Figure 4.1 are shown in black, and the $O(^3P)$ yield spectrum obtained from PHOFEX spectroscopy by O'Keeffe et al. is shown in gray.[61]

$O_2(d^1\Pi_g \leftarrow\leftarrow a^1\Delta_g)$ transition is shown by the black solid line, and the $O(^3P)$ yield from a PHOFEX spectrum reported by O'Keeffe et al. is shown by the dashed gray line.[61] There is a minor feature in the $O(^3P)$ yield spectrum that is much broader than single rotational transitions, indicating peaks in the absorption spectra cannot account for differences in intensity between the even and odd rotational states observed in the 1-color REMPI spectrum.

The enhanced odd rotational state peaks are instead believed to result from greater coupling between the B state and $^3A''$ states than $^3A'$ states. Potential energy curves have been previously calculated for repulsive $^3A'$ and $^3A''$ states that cross the minimum of the B ($^1A'$)

state and correlate with spin-forbidden products.[2,65,118] Both $^3A'$ and $^3A''$ states correlate with each of the spin-forbidden channels. Because the fragment O_2 has been shown to conserve the symmetry of the parent O_3 at cold temperatures in the Hartley band, the relative populations of even and odd rotational states should reflect the relative contributions of the A' and A'' states to the dissociation. Grebenshchikov and Rosenwaks also calculated the coupling between the B state and each of the triplet states for a single geometry ($R_1 = 2.43\ a_0$, $R_2 = 3.20\ a_0$, and $\alpha = 117°$), shown in Figure 4.3. A 1D Landau-Zener model can be used

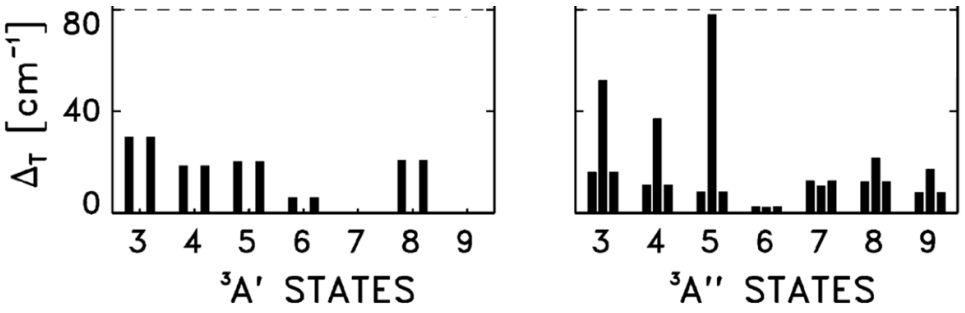

Figure 4.3: Spin-orbit matrix elements calculated by Grebenshchikov and Rosenwaks for coupling between the B state of O_3 and the repulsive $^3A'$ and $^3A''$ states correlating to spin-forbidden products.[65] Reprinted (adapted) with permission from Grebenshchikov and Rosenwaks, *J. Phys. Chem. A* 2010, 114, 36, 9809-9819. Copyright 2010 American Chemical Society.

to calculate the probability P of crossing from the B state to each of the triplet states with the following equation,

$$P = 2\ exp\left[\frac{-2\pi\Delta_T^2}{\hbar\nu|F_B - F_T|}\right]\left(1 - exp\left[\frac{-2\pi\Delta_T^2}{\hbar\nu|F_B - F_T|}\right]\right), \tag{4.1}$$

where Δ_T is the spin-orbit matrix element between the B state and the triplet state, ν is the relative velocity, and F_B and F_T are the slopes of the B and triplet state potential curves, respectively, at the crossing point. The calculated probabilities for each transition are shown in Table 4.1, obtained using the couplings calculated by Grebenshchikov and Rosenwaks, and a relative velocity estimated from the difference in energy between the initial excitation (320 nm) and the crossing point of the B and triplet states.

$^3A'$ states 3-5 and $^3A''$ states 3-4 correlate to O(^3P) and $O_2(a^1\Delta_g)$ products, and because A' states must correspond with even rotational states of $O_2(a^1\Delta_g)$ and A'' states must correspond with odd states, the relative probabilities of dissociation along $^3A'$ versus $^3A''$ states should correspond to the relative intensity of even and odd rotational states in the REMPI spectrum. Based on the probabilities in Table 4.1, transitions to $^3A''$ are 1.55 times more likely than transitions to $^3A'$ states. The utilized model is simple and only considers a single geometry, but the higher probability of $^3A''$ state dissociations is consistent with the enhanced odd rotational state peaks in the 320 nm REMPI spectrum in Figure 4.1.

Ion images of the $O_2(a^1\Delta_g)$ fragment were also collected in a 1-color experiment following O_3 dissociation near 320 nm and are shown in Figure 4.4. The outer ring in each image corresponds to spin-forbidden dissociation, forming $O_2(a^1\Delta_g)$ with an O(^3P) co-fragment. The diffuse signal at intermediate radii (approximately half the speed of the outer ring) is non-resonant and largely wavelength independent. The signal at small radii is attributed to spin-allowed dissociation of vibrationally excited O_3 forming $O_2(a^1\Delta_g)$ and O(^1D). The additional internal energy of the parent O_3 allows the spin-allowed singlet channel to be accessed despite the laser energy being below the dissociation threshold. Much less energy is available for fragment translation in the spin-allowed channel due to the higher dissocia-

$^3A'$ State	Relative Velocity	Transition Probability
$3\ ^3A'(1)$	1470 m/s	4.0x10^{-3}
$3\ ^3A'(3)$	1470 m/s	4.0x10^{-3}
$4\ ^3A'(1)$	2038 m/s	8.0x10^{-4}
$4\ ^3A'(3)$	2038 m/s	8.0x10^{-4}
$5\ ^3A'(1)$	1922 m/s	7.3x10^{-4}
$5\ ^3A'(3)$	1922 m/s	7.3x10^{-4}
$6\ ^3A'(1)$	1443 m/s	1.1x10^{-4}
$6\ ^3A'(3)$	1443 m/s	1.1x10^{-4}
$7\ ^3A'(1)$	1249 m/s	0
$7\ ^3A'(3)$	1249 m/s	0
$^3A''$ State	Relative Velocity	Transition Probability
$3\ ^3A''(1)$	2020 m/s	1.0x10^{-3}
$3\ ^3A''(2)$	2020 m/s	1.1x10^{-2}
$3\ ^3A''(3)$	2020 m/s	1.0x10^{-3}
$4\ ^3A''(1)$	2055 m/s	3.5x10^{-4}
$4\ ^3A''(2)$	2055 m/s	3.9x10^{-3}
$4\ ^3A''(3)$	2055 m/s	3.5x10^{-4}
$5\ ^3A''(1)$	2012 m/s	2.2x10^{-4}
$5\ ^3A''(2)$	2012 m/s	2.0x10^{-2}
$5\ ^3A''(3)$	2012 m/s	2.2x10^{-4}
$6\ ^3A''(1)$	1935 m/s	2.5x10^{-5}
$6\ ^3A''(2)$	1935 m/s	2.5x10^{-5}
$6\ ^3A''(3)$	1935 m/s	2.5x10^{-5}
$7\ ^3A''(1)$	1129 m/s	1.1x10^{-3}
$7\ ^3A''(2)$	1129 m/s	7.6x10^{-4}
$7\ ^3A''(3)$	1129 m/s	1.1x10^{-3}

Table 4.1: The triplet states are numbered by increasing energy, and the number in parentheses corresponds to the first, second, or third component of the triplet state as shown in Figure 4.3. There are additional triplet repulsive states that cross the B state at higher energies, but these are energetically inaccessible at 320 nm. The relative velocity for each crossing point and the transition probability calculated with couplings from Grebenshchikov and Rosenwaks[65] and Equation 4.1 are shown.

tion energy. Figure 4.5 shows the angular distributions of the outer ring from each image in Figure 4.4.

Analysis of the angular distributions is limited for a 1-color experiment because images are only collected in a single geometry (VV) and the system is underdetermined when using the equations of Wei et al. to extract vector correlations.[92] The angular distributions were fit with Equation 2.5 which includes the fourth Legendre polynomial (P_4) but does not include the sixth (P_6). Although the angular distribution should theoretically be fit with a P_6 polynomial because there are three photons with vertical polarization contributing to the anisotropy of the image, the P_6 cannot be detected experimentally in most cases and P_4 provides a reasonable fit. Table 4.2 shows the image anisotropy parameters, β_2 and β_4 corresponding to the angular distribution fits in Figure 4.5.

State	β_2	β_4
S17	1.08 $\pm$ 0.06	-0.22 $\pm$ 0.11
S18	1.25 $\pm$ 0.07	0.16 $\pm$ 0.11
S19	1.67 $\pm$ 0.06	0.44 $\pm$ 0.10
S20	1.54 $\pm$ 0.07	0.33 $\pm$ 0.13
R17	0.76 $\pm$ 0.06	-0.33 $\pm$ 0.06
R18	0.76 $\pm$ 0.05	-0.46 $\pm$ 0.06
R19	0.78 $\pm$ 0.06	-0.61 $\pm$ 0.08
R20	0.75 $\pm$ 0.05	-0.74 $\pm$ 0.06

Table 4.2: Image anisotropy parameters β_2 and β_4 obtained by fitting the angular distributions in Figure 4.5 with Equation 2.5.

The values of β_2 are similar for the S-branch j=19 and 20 transitions, and lower for j=17 and j=18. The values of β_2 are very similar for the R-branch j=17-20 transitions. The values

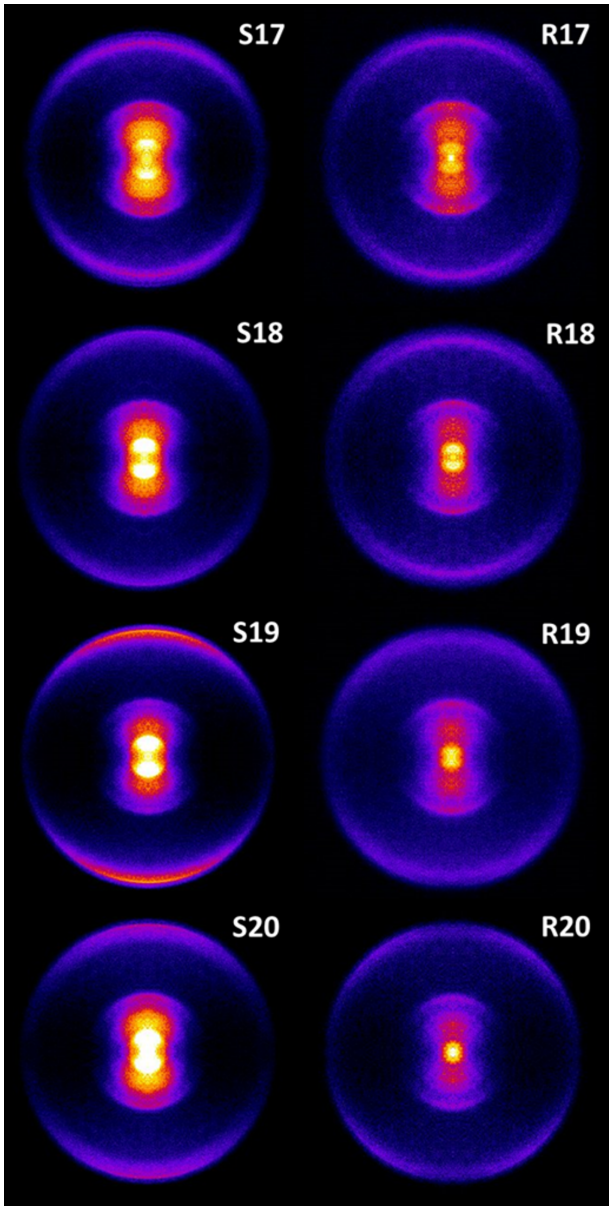

Figure 4.4: Symmetrized images of $O_2(a^1\Delta_g)$ in a 1-color experiment following dissociation of O_3, probed via the 2-0 band of the $O_2(d^1\Pi_g \leftarrow\leftarrow a^1\Delta_g)$ transition. The outer ring corresponds to spin-forbidden dissociation producing $O_2(a^1\Delta_g)$ with an $O(^3P)$ co-fragment, and the inner ring corresponds to spin-allowed dissociation of O_3 with additional internal energy producing $O_2(a^1\Delta_g)$ with an $O(^1D)$ co-fragment.

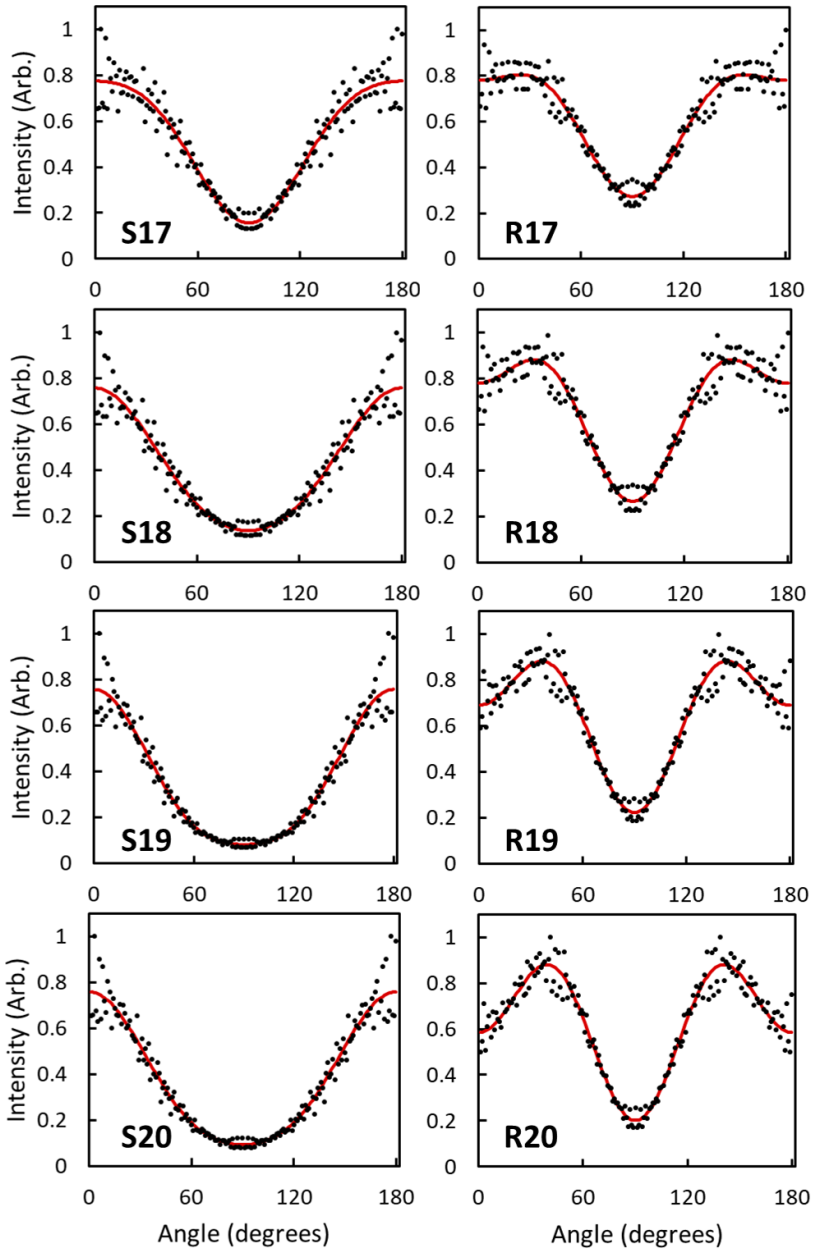

Figure 4.5: Angular distributions of the outer ring of the images in Figure 4.4. Black circles correspond to the experimental data and the red lines are fits to Equation 2.5.

of β_4 are positive for S-branch transitions of j=18-20 and negative for the S-branch transition of j=17 and all R-branch transitions. According to peak assignments from Morrill et al. and the speed distributions discussed in Section 4.3, the R- and S-branch transitions for j=17 and j=18 overlap with O- and P-branch transitions for higher rotational states.[82] Overlap with a P-branch transition is likely the reason β_4 is negative for the S-branch j=17 transition. The R- and S-branch transitions for j=19 and j=20 do not overlap with other transitions according to the assignments of Morrill et al., so these images are best for comparing even and odd rotational states. In both the S and R branches, the values of β_2 and β_4 are similar for j=19 and j=20.

The image anisotropy parameters obtained from 1-color 320 nm images can be compared to the anisotropy parameters extracted from 2-color images following a 266 nm dissociation shown in Table 4.3.[108] In Gunthardt's images, the anisotropy parameters are much more

70 K			170 K		
State	β_2	β_4	State	β_2	β_4
S19	1.88	0.39	S19	1.10	-0.10
S20	1.89	0.25	S20	1.17	0.02
R19	0.90	-0.72	R19	1.05	-0.06
R20	0.87	-0.96	R20	0.76	-0.59

Table 4.3: Image anisotropy parameters from $O_2(a^1\Delta_g)$ images following the 266 nm dissociation of O_3 from Gunthardt.[108] Images were collected at probe wavelengths corresponding to S- and R-branch transitions of j=19 and 20 to compare the anisotropy of odd and even rotational states at beam temperatures of 70 K and 170 K.

similar between odd and even rotational states at the low temperature and differ at higher

temperatures. The similarity between the values of β_2 and β_4 in Table 4.2 for S- and R-branch transitions of j=19 and 20 indicate a cold beam temperature, consistent with the 50 K temperature estimated from NO calibration. This supports the explanation that the enhancement of the odd rotational states in the REMPI spectrum in Figure 4.1 is in fact due to stronger coupling between the B and $^3A''$ states, rather than the dissociation of a warmer distribution of parent O_3 molecules.

Although analysis of 1-color images is limited due to the single laser geometry available, bipolar moments can be estimated through forward convolution and Monte Carlo simulation. The resulting bipolar moments for the angular distributions in Figure 3.8 are shown in Table 4.4. Because the system is underdetermined, the error bars on the bipolar moments are

Bipolar Moment	j=17	j=18	j=19	j=20
$\beta_0^2(20)$	0.52 $\pm$ 0.08	0.49 $\pm$ 0.06	0.65 $\pm$ 0.10	0.55 $\pm$ 0.09
$\beta_0^2(02)$	0.15 $\pm$ 0.17	-0.01 $\pm$ 0.19	-0.01 $\pm$ 0.17	-0.05 $\pm$ 0.19
$\beta_0^0(22)$	0.10 $\pm$ 0.11	-0.03 $\pm$ 0.09	0.01 $\pm$ 0.14	-0.11 $\pm$ 0.12
$\beta_0^2(22)$	-0.07 $\pm$ 0.13	0.13 $\pm$ 0.12	0.03 $\pm$ 0.15	0.15 $\pm$ 0.13
$\beta_0^2(24)$	0.33 $\pm$ 0.09	0.23 $\pm$ 0.07	0.37 $\pm$ 0.11	0.26 $\pm$ 0.09
$\beta_0^2(44)$	-0.37 $\pm$ 0.10	-0.30 $\pm$ 0.10	-0.38 $\pm$ 0.12	-0.31 $\pm$ 0.11
$\beta_0^0(44)$	-0.06 $\pm$ 0.14	0.08 $\pm$ 0.09	-0.28 $\pm$ 0.10	0.13 $\pm$ 0.13
$\beta_0^2(42)$	0.12 $\pm$ 0.12	-0.06 $\pm$ 0.14	-0.02 $\pm$ 0.15	-0.09 $\pm$ 0.15
$\beta_0^2(64)$	0.34 $\pm$ 0.08	0.25 $\pm$ 0.07	0.37 $\pm$ 0.11	0.27 $\pm$ 0.08

Table 4.4: Bipolar moments and error bars were obtained by fitting the angular distributions from Figure 4.5 via Monte Carlo simulation by forward convolution.

large. Despite the large uncertainty, general conclusions can be made. The value of $\beta_0^2(20)$, corresponding to the $\boldsymbol{\mu}$-$\boldsymbol{v}$ correlation is positive, consistent with a parallel transition to the

B state of O_3. The value of $\beta_0^0(22)$ is close to zero for all four rotational states. The $\boldsymbol{v}$-$\boldsymbol{j}$ should be negative for the dissociation of a triatomic, but overlap of rotational transitions of different branches may affect the angular distributions of j=17 and 18, resulting in near zero or positive values of $\beta_0^0(22)$.

4.3 $O_2(a^1\Delta_g)$ Ion Image Speed Distributions at 320 nm

The rotational state distribution of the $O_2(a^1\Delta_g)$ fragment following 320 nm dissociation of O_3 is difficult to obtain from the REMPI spectrum in Figure 4.1 because the resonant state of the REMPI scheme is highly perturbed. However, the speed distributions of the ion images indicate both high and low rotational states are formed. In 2-color images following 266 nm dissociation from Gunthardt et al., the speed distributions are unimodal, indicating fragments in a single rotational state.[47] A multimodal speed distribution indicates fragments in multiple rotational states. Figure 4.6 shows the outer edge of the reconstructed images corresponding to the symmetrized images in Figure 4.4 and the speed distribution of each outer ring. The black circles are the experimental speed distributions. Gaussian distributions centered on the expected speeds of fragments in the indicated rotational states based on the assignments of Morrill et al. are shown in maroon (O branch), green (P branch), blue (R branch) and purple (S branch) with the sum of the branches shown by the solid black line.[82] Gaussian distributions with σ=40 m/s were used, corresponding to 2% uncertainty in velocity.

The speed distributions of j=19 and 20 in the S branch and j=20 in the R branch are unimodal, as reported by Gunthardt et al. for a 266 nm dissociation.[47] The speed distributions of the j=17 and j=18 images in both branches and j=19 in the R branch are multimodal. Based on the assimgnments of Morrill et al., the S-branch transition of j=17 overlaps with the P-branch transition of j=35 and O-branch transition of j=43.[82] The S-branch transition of

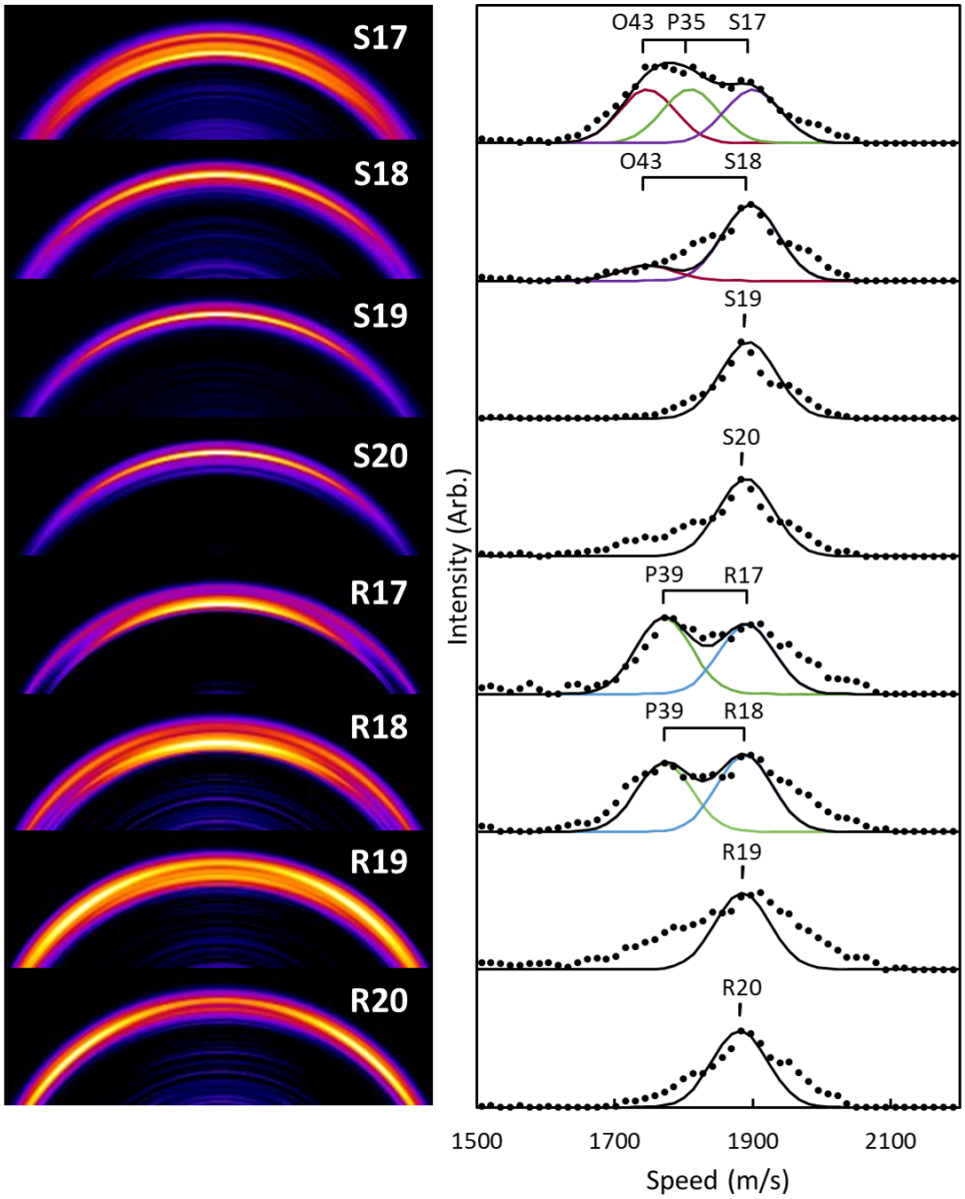

Figure 4.6: The outer edge of the reconstructed $O_2(a^1\Delta_g)$ ion images in Figure 4.4 is shown on the left. The speed distributions for each image are shown on the right, with the experimental data represented by black circles, and a Gaussian distribution representing each rotational state contributing to the overall signal shown in maroon (O branch), green (P branch), blue (R branch) and purple (S branch). The sum of the individual Gaussian distributions is represented by the solid black line.

j=18 overlaps with the O-branch transition of j=43. The R-branch transitions of j=17 and 18 overlap with the P-branch transition of j=39. While there is not a transition overlapping the R-branch j=19 transition in the assignments of Morrill et al., it is possible there is an additional unassigned transition at this wavelength. Following a 266 nm dissociation rotational states j$\geq$35 have very little or no population, so fragments in these states are not observed in the 2-color image speed distributions.[6,47] Population of both low rotational states (j=17-20) and high rotational states (j=35-43) indicates a broad rotational distribution of the $O_2(a^1\Delta_g)$ fragment following 320 nm dissociation.

O- and S-branch transitions are expected to have 2-fold symmetry, and P- and R-branch transitions are expected to have 4-fold symmetry for a perpendicular $\boldsymbol{v}$-$\boldsymbol{j}$ correlation. The S-branch images all appear to have 2-fold symmetry, and the R-branch images of j=19 and 20 as well as the outer edge of the ring in the j=17 and j=18 images have 4-fold symmetry. The inner edge of the rings in the R-branch images of j=17-19 have 2-fold symmetry, which is inconsistent with the P-branch assignments in the j=17 and j=18 speed distributions. The 2-fold symmetry suggests there may be additional transitions contributing to the observed signal at these wavelength. Based on the nearby peak assignments of Morrill et al., it is possible there are yet unassigned O-branch transitions at these wavelengths, which would lead to 2-fold symmetry. The signal assigned to the P-branch transition of j=35 in the S-branch image of j=17 also appears to have 2-fold symmetry, but this may be due to overlap with the O-branch transition of j=43 and the S-branch transition of j=17 which should both have 2-fold symmetry.[82]

The inner ring in the images shown in Figure 4.4 is attributed to spin-allowed dissociation of vibrationally excited O_3. Although the population of vibrational states above v=0 of O_3

is small, $O_2(a^1\Delta_g)$ fragments originating from vibrationally excited O_3 can be observed because the Franck-Condon factors are larger for higher vibrational states of O_3.[119] The inner ring of the images is wavelength dependent and appears to increase in radius with increasing laser energy in the R-branch images. There is not a clear trend in radius as a function of laser energy in the S-branch images. The R- and S-branch images were collected on separate days and are therefore subject to changes in beam temperature or other running conditions that would cause subtle effects on fragments at fast speeds, but will be more significant close to threshold. The measured fragment speed can be converted to total translational energy of both fragments, and this can be compared to the calculated available energy for the probed rotational state formed in a spin-allowed dissociation, without including the internal energy of the parent O_3. The calculated available energy is negative because the photon energy is less than the dissociation energy of the spin-allowed singlet channel. If the calculated translational energy ($E_{T,calc} = h\upsilon - D_0 - E_{int,O_2}$) is plotted as a function of the experimental translational energy (derived from the measured fragment speed), the y-intercept will be the negative of the internal energy of the parent O_3 molecule.

The R-branch image translational energies are shown in Figure 4.7. Reconstruction methods work best at larger radii, so identifying peaks for low energy fragments in the reconstructed radial distribution is difficult. The outer edge of the inner rings were instead estimated from the raw, symmetrized images. The error bars represent an uncertainty of 1-2 pixels for the radius of the inner ring. The absolute value of the y-intercept represents the internal energy of the O_3 molecule. An internal energy of 1941.5 cm^{-1} is consistent with two quanta of vibrational energy, but it is unclear from this analysis which vibrational modes are excited in this process. The vibrational frequencies of O_3 (X) are 1103 cm^{-1} (symmetric

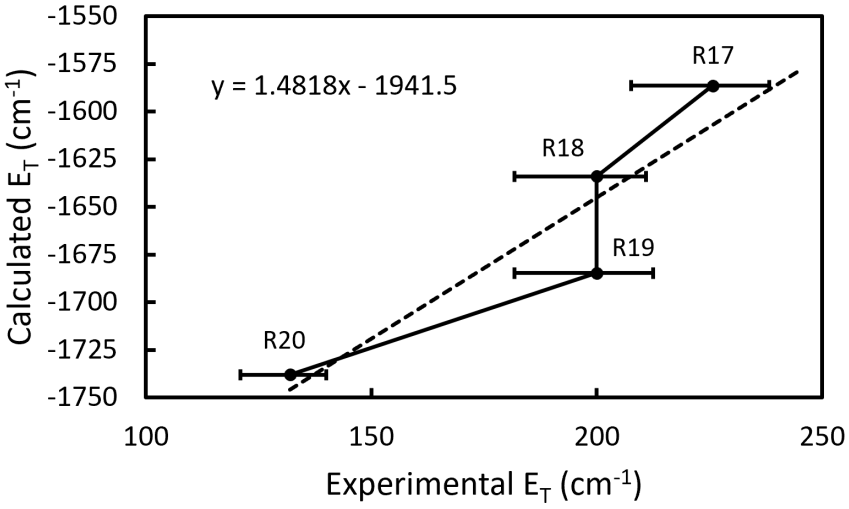

Figure 4.7: The total translational energy for both fragments is calculated from the photon energy and dissociation energy for fragments in j=17-20 and plotted as a function of the experimental translational energy determined from fragment speed in the ion images.

stretch), 1042 cm^{-1} (asymmetric stretch), and 701 cm^{-1} (bend), and Takahashi et al. have previously argued the asymmetric stretch primarily contributes to the observed hot bands.[119]

4.4 $O_2(a^1\Delta_g)$ Rotational Distribution at 330 nm

The $O_2(a^1\Delta_g)$ image speed distributions following 320 nm dissociation of O_3 suggest a broad rotational distribution extending from at least j=17 to j=43. $O_2(a^1\Delta_g)$ REMPI spectra can be used to further support a broad distribution. The 1-0 band of the $O_2(d^1\Pi_g \leftarrow\leftarrow a^1\Delta_g)$ transition was used to probe the $O_2(a^1\Delta_g)$ fragment despite the perturbed resonant state because this REMPI scheme overlaps with the 4-0 band of the $O_2(d^1\Pi_g \leftarrow\leftarrow b^1\Sigma_g^+)$ transition which is unperturbed.

Figure 4.8 shows the $O_2(d^1\Pi_g, v = 1 \leftarrow\leftarrow a^1\Delta_g, v = 0)$ REMPI spectrum collected in

a 1-color experiment following the dissociation of O_3 near 330 nm. The spectrum at shorter

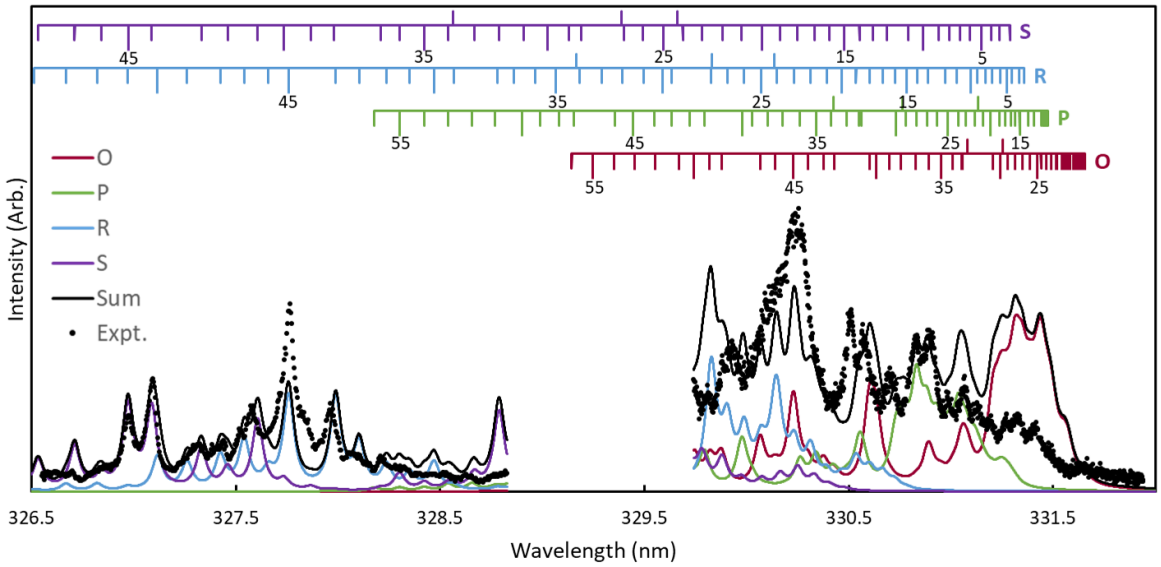

Figure 4.8: REMPI spectrum of $O_2(a^1\Delta_g)$ collected in a 1-color experiment following the dissociation of O_3 near 330 nm, probed via the $O_2(d^1\Pi_g, v = 1 \leftarrow\leftarrow a^1\Delta_g, v = 0)$ transition. The black circles indicate experimental data, obtained in a 2D-REMPI spectrum at shorter wavelengths and a 1D spectrum at longer wavelengths. The O, P, R, and S branches are shown in maroon, green, blue, and purple, respectively, with the sum of the branches shown by the solid black line.

wavelengths was collected in a 2D-REMPI spectrum that was integrated over a narrow range of fragment speeds corresponding to the $O_2(a^1\Delta_g, v = 0)$ fragments. The 2D-REMPI will be discussed in Section 4.5. The spectrum at longer wavelengths is a 1D-REMPI with a mask over the center of the detector to block low-velocity signal. There was no data collected at intermediate wavelengths. Because the spectra were collected independently, they were scaled relative to each other to best fit the simulation. The black circles in Figure 4.8 represent

experimental data, and the simulated O, P, R, and S branches used to fit the spectrum are shown in maroon, green, blue, and purple, respectively. The solid black line is the sum of the branches. The combs at the top indicate the rotational transitions at each wavelength based on spectroscopic constants derived from $O_2(a^1\Delta_g, v = 0)$ energy levels from Morrill et al.,[82] adjusted to fit previous data, and $O_2(d^1\Pi_g, v = 1)$ energy levels from O'Keeffe et al.[73] Because of the perturbed nature of the resonant state and the highly overlapped rotational branches in the REMPI spectrum, extracting accurate rotational state populations is difficult, but there is clear evidence that the rotational distribution is broad. Specifically, there is evidence of low rotational states (j=20-25) between 330.5 and 331.5 nm and evidence of high rotational states (j=40-50) between 326.5 and 328.5 nm.

To account for the perturbations in the resonant state, scaling factors corresponding to each rotational level of $O_2(d^1\Pi_g, v = 1)$ were included in the simulation that scaled the intensity of all transitions leading to the same upper state equally. The scaling factors were determined by fitting the $O_2(d^1\Pi_g, v = 1 \leftarrow\leftarrow a^1\Delta_g, v = 0)$ REMPI spectrum from Morrill et al. with a rotational distribution determined from classical trajectory calculations, depolarized by Gunthardt's classical model.[47,82] The REMPI spectrum from Morrill et al. was collected following 280 nm dissociation of O_3, and the O_2 distribution was expected to be thermalized because the authors used 46 mTorr of O_3 in 7 Torr of He. The rotational distribution for a 282 nm dissociation from Warter et al. was depolarized with the classical model of Gunthardt et al. at a temperature of 300 K.[12,47] The depolarized rotational distribution was used to fit Morrill's spectrum, adjusting only the scaling factors of the $O_2(d^1\Pi_g)$ rotational levels.

Figure 4.9 shows the 1-0 REMPI spectrum of $O_2(d^1\Pi_g \leftarrow\leftarrow a^1\Delta_g)$ from Morrill et al. at

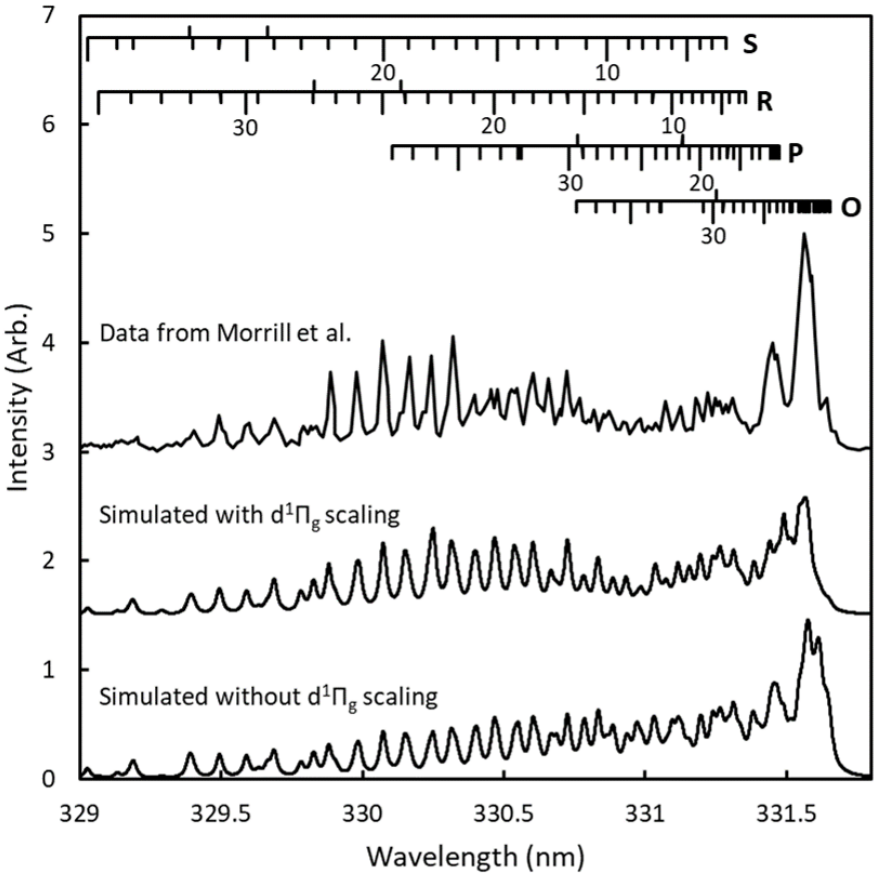

Figure 4.9: The experimental 1-0 REMPI spectrum of $O_2(d^1\Pi_g \leftarrow\leftarrow a^1\Delta_g)$ collected by Morrill et al. following the 280 nm dissociation of O_3 is shown at the top.[82] The simulated REMPI spectra using the O_2 rotational distribution calculated by classical trajectory calculations[12] and depolarized[47] are shown with (middle) and without (bottom) scaling factors for each rotational level of the $O_2(d^1\Pi_g)$ state included.

the top.[82] Spectra simulated using the depolarized rotational state distribution for a 282 nm dissociation with scaling of the $O_2(d^1\Pi_g)$ rotational levels is shown in the middle and the simulation without $d^1\Pi_g$ state scaling is shown on the bottom. Including the scaling factors better reproduces the increase in intensity around 330 nm and the dip in intensity around 331 nm. The $O_2(d^1\Pi_g)$ scaling factors were included in the simulated REMPI spectrum in Figure 4.8 to estimate the rotational state distribution of $O_2(a^1\Delta_g)$ following 330 nm dissociation.

The rotational state distribution obtained from fitting the REMPI spectrum in Figure 4.8 is shown in black in Figure 4.10. In their fits of kinetic energy distributions from $O(^3P)$

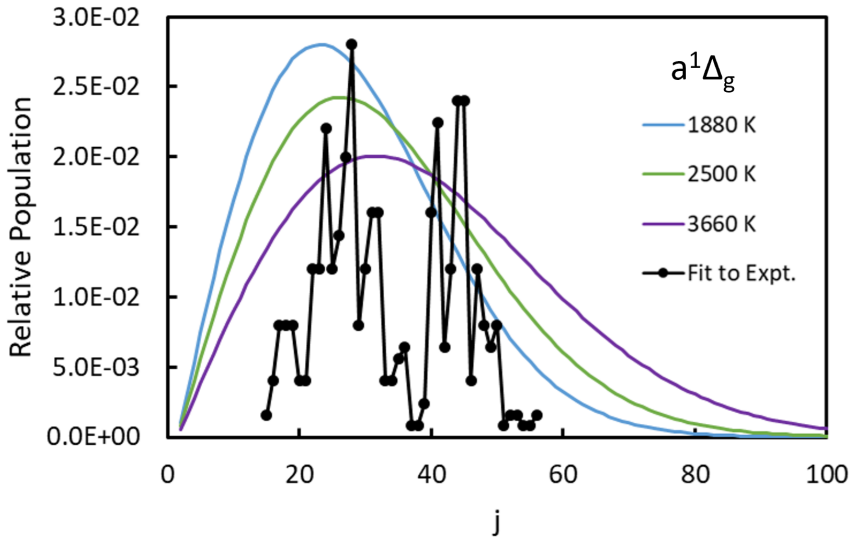

Figure 4.10: The rotational state populations fit to the REMPI spectrum in Figure 4.8 are shown in black. Rotational state populations for Boltzmann distributions at 1880 K, 2500 K, and 3660 K are shown in blue, green, and purple, respectively.

ion images, Ulrich et al. reported rotational temperatures of 1880 K and 3660 K for their "full" and "restricted" models, and the authors proposed 2500 K as an average temperature. Boltzmann rotational state distributions for 1880 K, 2500 K, and 3660 K are shown in blue, green, and purple, respectively in Figure 4.10. The rotational state distribution fit to the experimental spectrum is clearly non-Boltzmann, but accurate populations are difficult to obtain because of the perturbed resonant state and the assumptions included in fitting the spectrum with resonant state scaling factors. The experimental rotational state distribution appears bimodal with low population around j=35-40. The R- and S-branch transitions of these rotational states are in the wavelength region where no data was collected, and the O- and P-branch transitions of these rotational states overlap with R- and S-branch transitions of lower rotational states. As a result, the population of rotational states in middle of the distribution is unclear.

As further evidence for the assigned rotational state transitions in Figure 4.8, images were taken throughout the 1D spectrum, and the speed distributions can be compared to the expected speeds for fragments in the assigned rotational states. Figure 4.11 shows the longer wavelength region of the $O_2(d^1\Pi_g, v = 1 \leftarrow\leftarrow a^1\Delta_g, v = 0)$ REMPI spectrum from Figure 4.8. The speed distributions shown in (b)-(e) correspond to images taken at wavelengths in the spectrum indicated by the arrows in (a). The experimental speed distributions shown in black circles were fit with Gaussian distributions centered at the expected speeds of fragments in the rotational states assigned in Figure 4.8, with σ=35 m/s, corresponding to $\sim$2% uncertainty. Gaussian distributions shown in maroon, green, blue, and purple, correspond to O-, P-, R-, and S-branch transitions, and the sum of the branches is shown by the solid black line. The relative intensity of the transitions will vary throughout a peak in the REMPI spec-

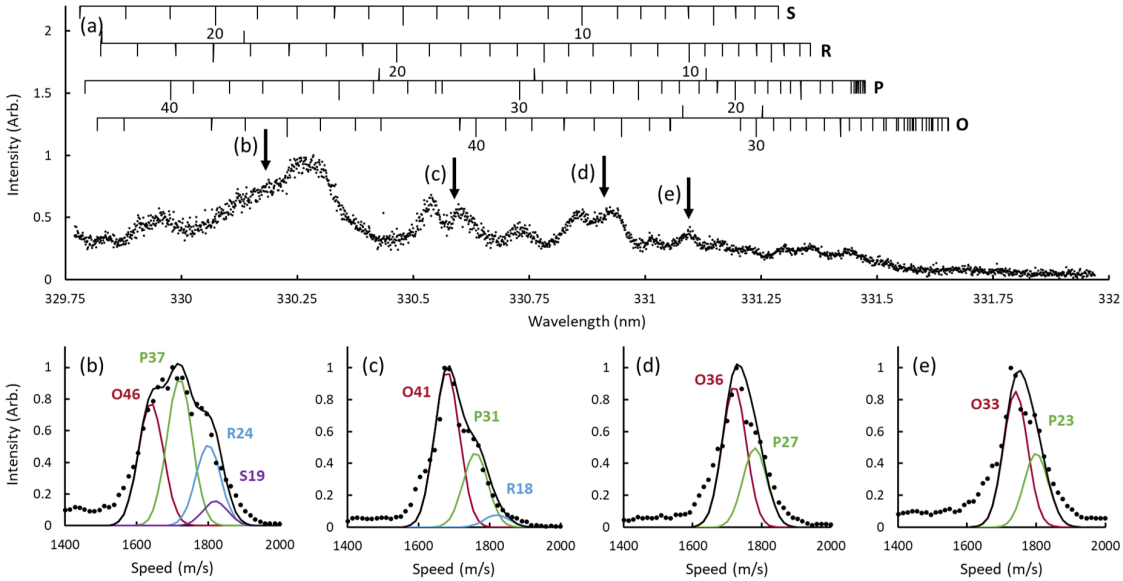

Figure 4.11: The 1-D REMPI spectrum of the $O_2(d^1\Pi_g, v = 1 \leftarrow\leftarrow a^1\Delta_g, v = 0)$ transition from Figure 4.8 is shown in (a). Panels (b)-(e) are speed distributions for images collected at wavelengths indicated by the arrows in (a). The experimental speed distributions are shown in black circles, and are fit with Gaussian distributions corresponding to the expected fragment speeds based on the rotational states assignments in Figure 4.8.

trum based on the extent of overlap between nearby transitions, so the relative intensities of the peaks in the speed distributions are not necessarily reflective of the relative populations of the corresponding rotational states. However, the speed distributions are consistent with the rotational state assignments.

The high intensity peaks in the short wavelength region of the $O_2(d^1\Pi_g, v = 1 \leftarrow\leftarrow a^1\Delta_g, v = 0)$ REMPI spectrum approximately overlap with peaks in the $O(^3P)$ yield spectrum reported by O'Keeffe et al.[61] as shown in Figure 4.12. Overlap of peaks in the O_3

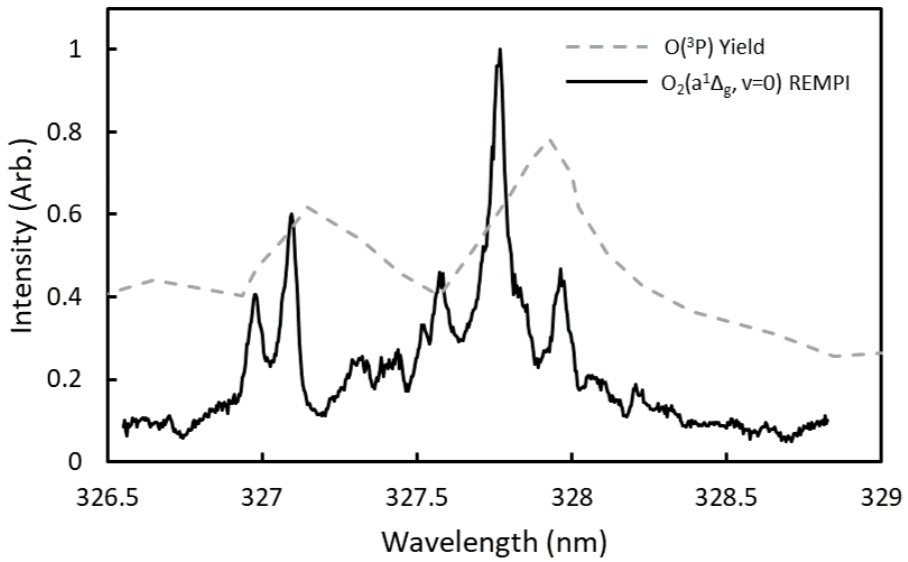

Figure 4.12: The $O_2(d^1\Pi_g, v = 1 \leftarrow\leftarrow a^1\Delta_g, v = 0)$ REMPI spectrum from the short wavelength region of Figure 4.8 is shown in black and the $O(^3P)$ yield spectrum from O'Keeffe et al. is shown by the dashed gray line.[61]

absorbance spectrum and REMPI peaks may indicate that the increased signal is due to in-

creased O_3 absorption rather than reflective of an increase in the population of the rotational state corresponding to the intense peaks, but 2-color experiments with a single dissociation wavelength would be necessary to further study the effect of the dissociation wavelength on the resulting REMPI spectrum.

4.5 $O_2(b^1\Sigma_g^+)$ Rotational and Vibrational Distributions at 330 nm

The rotational distribution of the $O_2(b^1\Sigma_g^+)$ fragment was previously reported by O'Keeffe et al. following dissociation at 337.2 and 344 nm, but the REMPI schemes used by the authors accessed a perturbed vibrational level of the resonant $O_2(d^1\Pi_g)$ state and these perturbations needed to be accounted for in their fitting of the rotational state distribution.[73] Vibrational levels v$\geq$4 of the $O_2(d^1\Pi_g)$ state are unperturbed and therefore extraction of rotational state distributions from REMPI spectra accessing these higher vibrational levels is more straightforward. The 4-0 band of the $O_2(d^1\Pi_g \leftarrow\leftarrow b^1\Sigma_g^+)$ transition corresponds to wavelengths near 330 nm, which overlaps with the 1-0 band of the $O_2(d^1\Pi_g \leftarrow\leftarrow a^1\Delta_g)$ transition discussed in Section 4.4.

Figure 4.13 shows the 1D-REMPI spectrum of $O_2(b^1\Sigma_g^+, v = 0)$ collected between 326.61 and 328.85 nm. For this spectrum, a mask was used to cover low-velocity signal and the total unblocked signal was collected with a PMT. Based on simulations, this wavelength range was expected to be primarily the $O_2(d^1\Pi_g, v = 4 \leftarrow\leftarrow b^1\Sigma_g^+, v = 0)$ transition with minor contributions from the $O_2(d^1\Pi_g, v = 1 \leftarrow\leftarrow a^1\Delta_g, v = 0)$ transition. Because the $O_2(a^1\Delta_g)$ rotational state distribution extends to high rotational states, the $a^1\Delta_g$ state contribution is more significant than initially expected. In Figure 4.13, the black circles are the experimental data. The simulated P, R, and S branches are shown in green, blue, and purple, respectively, with the sum of the branches shown by the solid black line. The rotational

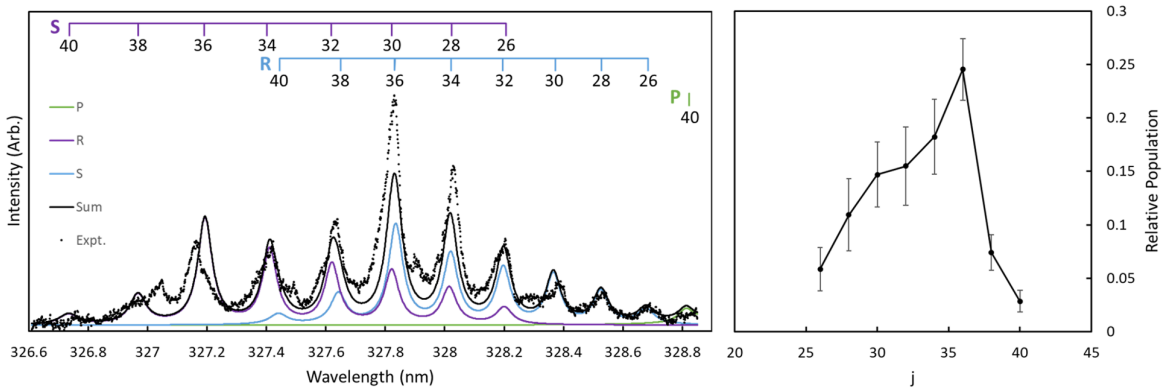

Figure 4.13: REMPI spectrum of O_2 in a 1-color experiment following the dissociation of O_3 near 330 nm, probed via the $O_2(d^1\Pi_g, v = 4 \leftarrow\leftarrow b^1\Sigma_g^+, v = 0)$ transition. The black circles indicate experimental data. The P, R, and S branches are shown in green, blue, and purple, respectively, with the sum of the branches represented by the solid black line. The rotational state distribution used to fit the spectrum is shown on the right.

state distribution used in the fit is shown on the right, with error bars obtained by Monte Carlo simulation.

The simulated spectrum fits the general shape of the experimental spectrum and the intensity of several of the peaks, but the intensity of the peaks near 327.8 and 328 nm as well as several minor features are not reproduced in the simulation. The peaks in the center of the spectrum are assigned to the S-branch transitions of j=28 and 30 and the R-branch transitions of j=34 and 36. The high intensity of the peak corresponding to the R-branch transition of j=36 results in a relatively high population in j=36 in the fit rotational state distribution. Additionally, there are features around 327, 327.5, and 327.9 nm that are not reproduced in the simulation. Based on the regular spacing of the major peaks and the unperturbed nature of the $O_2(d^1\Pi_g, v = 4 \leftarrow\leftarrow b^1\Sigma_g^+, v = 0)$ REMPI scheme used, these small features are not consistent with signal from the $O_2(b^1\Sigma_g^+)$ fragment. These discrepancies between the data

and the fit suggest contribution from the high rotational states in the $O_2(a^1\Delta_g)$ REMPI spectrum. The $O_2(a^1\Delta_g)$ fragment has lower electronic energy than the $O_2(b^1\Sigma_g^+)$ so is expected to be traveling faster following dissociation, but in a 1D-REMPI spectrum where the total ion count is recorded, fragments of different speeds cannot be distinguished from each other. 2D-REMPI allows spatial resolution of the fragments by collecting an image at each wavelength step in the spectrum. Fragments in the $a^1\Delta_g$ and $b^1\Sigma_g^+$ electronic states will appear at different radii because of the difference in speed, which can be resolved in ion images.

The 2D-REMPI spectrum collected over the same wavelength range is shown in Figure 4.14. The spectrum was obtained by collecting a velocity-mapped image at each wavelength

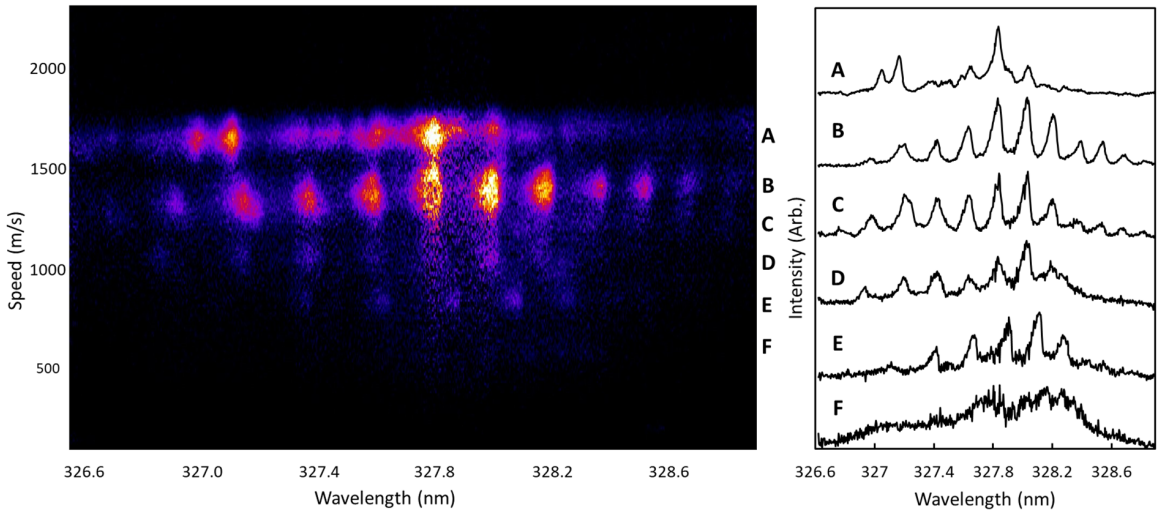

Figure 4.14: 2D-REMPI spectrum of O_2 following the dissociation of O_3 collected in a 1-color experiment near 330 nm. An image was collected at each wavelength step and the reconstructed speed distributions were plotted as a function of wavelength on the left. The 2D spectrum was integrated at locations A-F over ranges of speed corresponding to different electronic and vibrational states of O_2 to obtain the 1D spectra on the right. Region A is assigned to v=0 of $O_2(a^1\Delta_g)$ and B-F are assigned to v=0-4 of $O_2(b^1\Sigma_g^+)$.

step. The reconstructed speed distribution is plotted as a function of wavelength on the left in Figure 4.14. There are several horizontal bands in the spectrum, corresponding to fragments traveling a particular speed. Fragments traveling different speeds can be assigned to different electronic and vibrational states of O_2. Each horizontal band is integrated over a narrow range of speeds to obtain the 1D spectra on the right. The fastest fragments (Region A) are attributed to $O_2(a^1\Delta_g, v = 0)$, and the next fastest band (Region B) is attributed to $O_2(b^1\Sigma_g^+, v = 0)$. Based on the structure of the peaks and the speed distribution, the signal at lower speeds (Regions C-F) are assigned to v=1-4 of $O_2(b^1\Sigma_g^+)$ with higher vibrational states traveling slower speeds.

A vertical slice of the 2D spectrum integrated over a narrow wavelength range provides a speed distribution that can be used to confirm the electronic and vibrational state assignments. Figure 4.15 shows the average image (a) and corresponding speed distribution (b) for the 2D spectrum integrated between 327.970 and 328.145 nm, as well as the $O_2(b^1\Sigma_g^+)$ vibrational state distribution obtained from the translational energy distribution of the full spectrum (c). The faint outer ring in the image is assigned to $O_2(a^1\Delta_g, v = 0)$ and the next ring, corresponding to the tallest peak in the speed distribution is assigned to $O_2(b^1\Sigma_g^+, v = 0)$. There is overlap between v=0 and v=1 of $O_2(b^1\Sigma_g^+)$, so v=1 appears as a shoulder on the v=0 peak in the speed distribution. The remaining peaks in the speed distribution are consistent with v=2, 3, and 4 of $O_2(b^1\Sigma_g^+)$. The speed distribution is fit with a series of Gaussian distributions centered at the speeds expected for the fragments in the ro-vibrational states assigned to the REMPI peaks in Figures 4.16 and 4.17. The values of σ used in the Gaussian distribution increase with increasing vibrational states because similar distributions in energy will result in broader distributions in speed at lower speeds. Similar analysis was performed

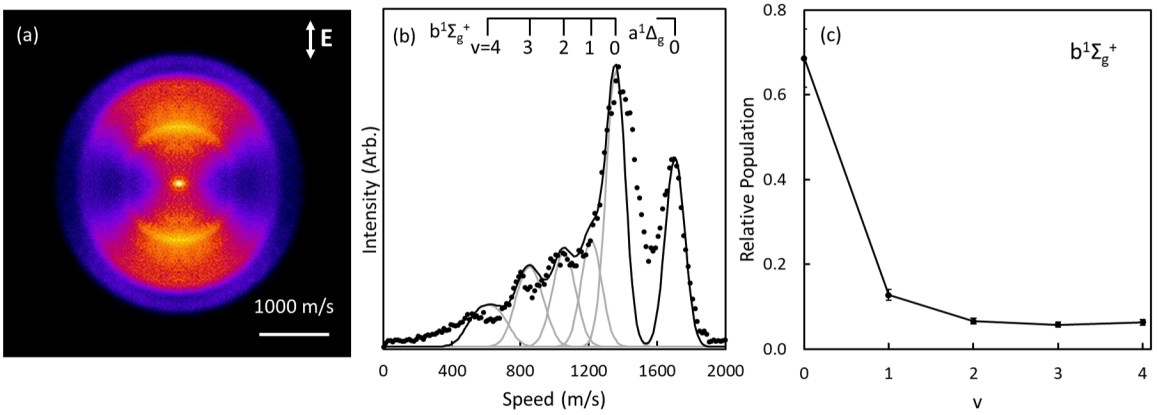

Figure 4.15: Images collected between 327.970 and 328.145 nm were averaged to obtain the image in (a). The speed distribution corresponding to the image is shown in (b), with peaks assigned to v=0 of $O_2(a^1\Delta_g)$ and v=0-4 of $O_2(b^1\Sigma_g^+)$. The translational energy distribution of the spectrum integrated between 327.620 and 328.870 nm was used to obtain the $O_2(b^1\Sigma_g^+)$ vibrational state distribution shown in (c).

following integration between 327.620 and 328.870 nm, which is almost the entire spectrum, to obtain the $O_2(b^1\Sigma_g^+)$ vibrational state distribution. The wavelength limits were chosen to maximize R- and S-branch contributions from $O_2(b^1\Sigma_g^+, v = 0-3)$ and minimize O- and P-branch contributions. The integrated area of the distributions used to fit the translational energy distribution of the whole spectrum were corrected by the Franck-Condon factor for each vibrational state to obtain the vibrational state distribution in (c). The Franck-Condon factors calculated with FC Intensity used in determining the vibrational state distribution are shown in Table 4.5.[120] The resulting vibrational distribution peaks at v=0 and decreases with increasing vibrational state.

The 1D spectrum of the $O_2(a^1\Delta_g)$ state was previously shown in Figure 4.8 and discussed. The remaining 1D spectra from Figure 4.14 can be fit individually to obtain rotational state distributions for each vibrational level of the $b^1\Sigma_g^+$ state. The spectrum corresponding

$v' \leftarrow\leftarrow v''$	Franck-Condon Factor
4-0	0.061
5-1	0.158
6-2	0.222
7-3	0.213
8-4	0.142

Table 4.5: Franck Condon factors for the 4-0, 5-1, 6-2, 7-3, and 8-4 bands of the $O_2(d^1\Pi_g \leftarrow\leftarrow b^1\Sigma_g^+)$ transition probed in the 2D-REMPI spectrum in Figure 4.14 calculated with FCIntensity.[120]

to Region B in Figure 4.14, assigned to the $O_2(d^1\Pi_g, v = 4 \leftarrow\leftarrow b^1\Sigma_g^+, v = 0)$ transition, is shown in Figure 4.16. The experimental spectrum is represented by black circles, with the simulated P, R, and S branches shown in green, blue, and purple respectively. The sum of the branches is shown by the solid black line, and the rotational state distribution used to fit the spectrum is shown on the right. The error bars were obtained by Monte Carlo simulation. The rotational distribution is similar to the distribution fit to the 1D spectrum in Figure 4.13, but without the relatively high population of j=36, which contained signal from $O_2(a^1\Delta_g)$. The rotational state distribution is similar but slightly narrower than the distribution reported by O'Keeffe et al. for dissociation at 337.2 nm, and shifted to higher rotational states than the distribution reported for a 344 nm dissociation.[73]

The fits and rotational state distributions for $O_2(b^1\Sigma_g^+, v = 1 - 4)$ are shown in Figure 4.17. The simulated spectra were calculated using spectroscopic constants of $O_2(b^1\Sigma_g^+)$ and $O_2(d^1\Pi_g)$ to determine the transition energies and adjustable linewidths which will be further discussed in Chapter 5. The lower vibrational states (v=0-2) of $O_2(b^1\Sigma_g^+)$ have been previously studied and well-characterized.[73,82] Rotational constants fit to the reported en-

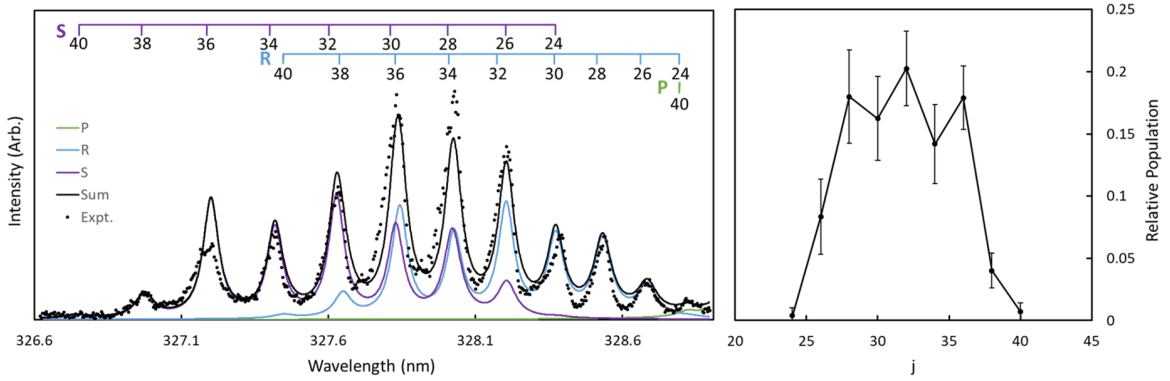

Figure 4.16: The 1D spectrum of the $O_2(d^1\Pi_g, v = 4 \leftarrow\leftarrow b^1\Sigma_g^+, v = 0)$ transition obtained by integrating the 2D-REMPI spectrum over a range of speeds corresponding to $O_2(b^1\Sigma_g^+, v = 0)$ is represented by the black circles. The P, R, and S branches are shown in green, blue, and purple, respectively, with the sum of the branches shown by the solid black line. The rotational state distribution used to fit the spectrum is shown on the right.

ergies were used in the simulations and the rotational constants of the lower vibrational states were extrapolated to obtain rotational constants of the higher vibrational levels (v=3-4) of $O_2(b^1\Sigma_g^+)$. The lower vibrational levels (v=0-4) of the $O_2(d^1\Pi_g)$ have also been well-characterized, but of the previously studied vibrational levels, only v=4 is unperturbed. Therefore the rotational constants could not be extrapolated to higher vibrational levels for the resonant state. To estimate the rotational constants of the higher vibrational levels of $O_2(d^1\Pi_g)$, the BCONT program was used, which calculates eigenvalues for a given potential.[103] The potential from Li et al.[76] was adjusted until the calculated vibrational levels were similar to those calculated by Morrill et al.[74] The rotational constant for v=4 calculated with BCONT was slightly different than the previous experimentally determined constant, so the rotational constants for all vibrational levels were scaled to account for this difference. To fit the spectra, the energies of the $O_2(d^1\Pi_g)$ vibrational levels needed to be shifted relative

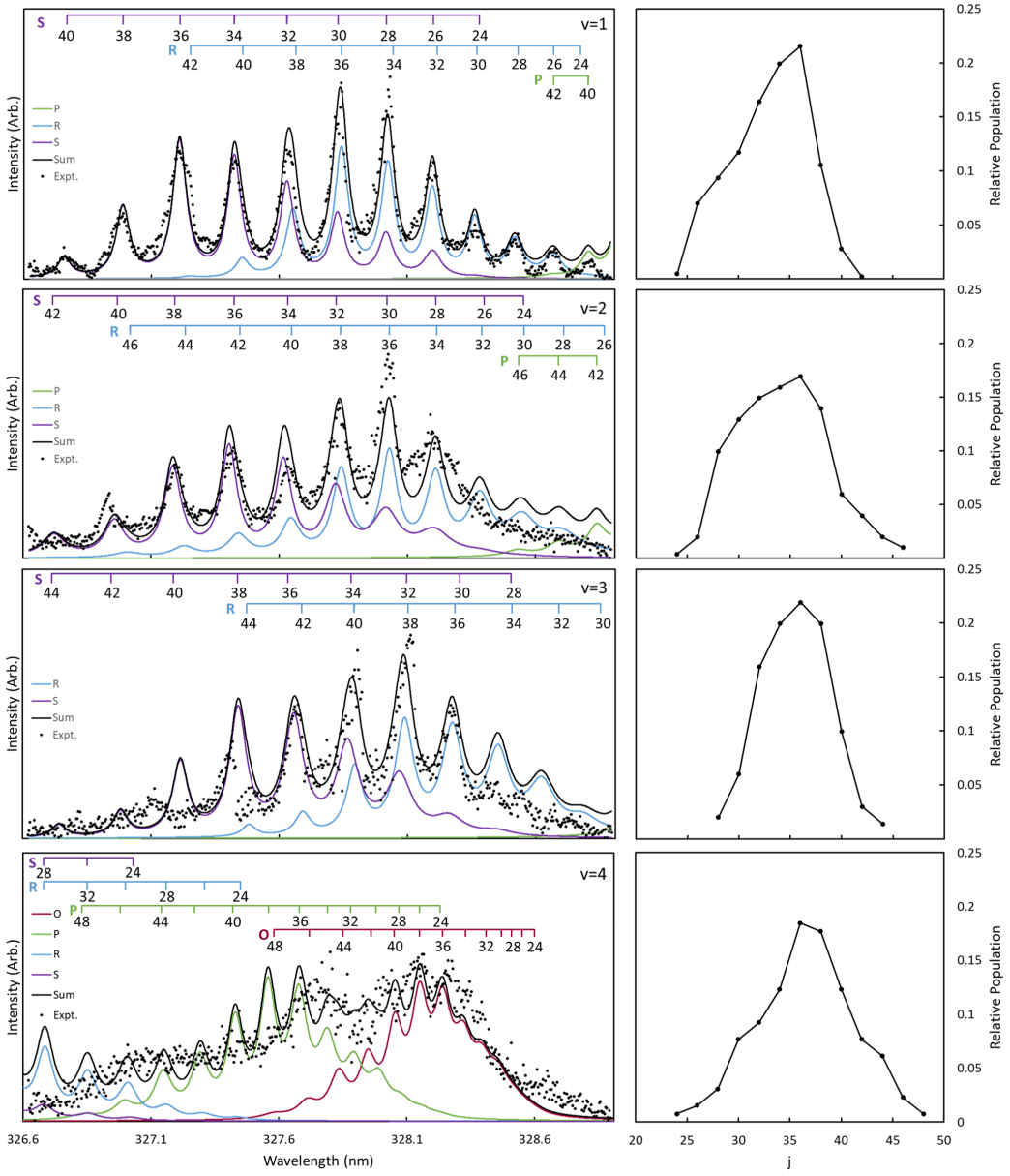

Figure 4.17: 1D spectra of the 5-1, 6-2, 7-3, and 8-4 bands of the $O_2(d^1\Pi_g \leftarrow\leftarrow b^1\Sigma_g^+)$ transition obtained from the 2D spectrum in Figure 4.14 are shown in black circles. The O, P, R, and S branches are shown in maroon, green, blue, and purple, respectively, with the sum shown in black. The rotational state distributions corresponding to each fit are shown on the right.

to the energies previously calculated. However, the spacing of the peaks is consistent with overlapped R and S branches of the $O_2(b^1\Sigma_g^+)$ state and the difference in energy between the $O_2(d^1\Pi_g)$ and $O_2(C^3\Pi_g)$ is not enough to account for the energy shifts, so we believe the assignments of v=4-8 of the $O_2(d^1\Pi_g)$ state are the most reasonable. The spectroscopic constants used to fit the spectra are shown in Table 4.6.

State	T (cm^{-1})	b (cm^{-1})	d (cm^{-1})	Calc. T (cm^{-1})[74]
$O_2(b^1\Sigma_g^+, v=0)$	13122.32	1.39107	5.25865x10^{-6}	
$O_2(b^1\Sigma_g^+, v=1)$	14527.0	1.37301	5.43777x10^{-6}	
$O_2(b^1\Sigma_g^+, v=2)$	15903.7	1.35465	5.51256x10^{-6}	
$O_2(b^1\Sigma_g^+, v=3)$	17252.07	1.33649	5.48302x10^{-6}	
$O_2(b^1\Sigma_g^+, v=4)$	18572.85	1.31828	5.34915x10^{-6}	
$O_2(d^1\Pi_g, v=4)$	73746.87	1.588308	4.7023x10^{-6}	73740
$O_2(d^1\Pi_g, v=5)$	75157.58	1.56724	5.09413x10^{-6}	75485
$O_2(d^1\Pi_g, v=6)$	76503.31	1.54713	5.14598x10^{-6}	77196
$O_2(d^1\Pi_g, v=7)$	77810.58	1.52689	5.20024x10^{-6}	78924
$O_2(d^1\Pi_g, v=8)$	79465	1.50653	5.25708x10^{-6}	80596

Table 4.6: Spectroscopic constants used to fit the spectra in Figures 4.16 and 4.17 are shown. The calculated T values from Morrill et al. are shown in the last column for comparison.[74]

Based on the fits in Figures 4.16 and 4.17, the rotational state distributions of v=0-4 of $O_2(b^1\Sigma_g^+)$ are all very similar, extending from j$\sim$24 to j$\sim$46. This differs from rotational state distributions measured in the Hartley band where lower rotational states are populated in higher vibrational levels.

As discussed in Section 4.4 for the $O_2(a^1\Delta_g)$ rotational state distribution, Ulrich et al. assumed Boltzmann rotational distributions of the $O_2(a^1\Delta_g$ and $b^1\Sigma_g^+)$ fragments to fit their

$O(^3P)$ ion images.[71] Like the $O_2(a^1\Delta_g)$ rotational state distribution, the $O_2(b^1\Sigma_g^+)$ is also non-Boltzmann. Figure 4.18 (a) shows a comparison of the experimental rotational state

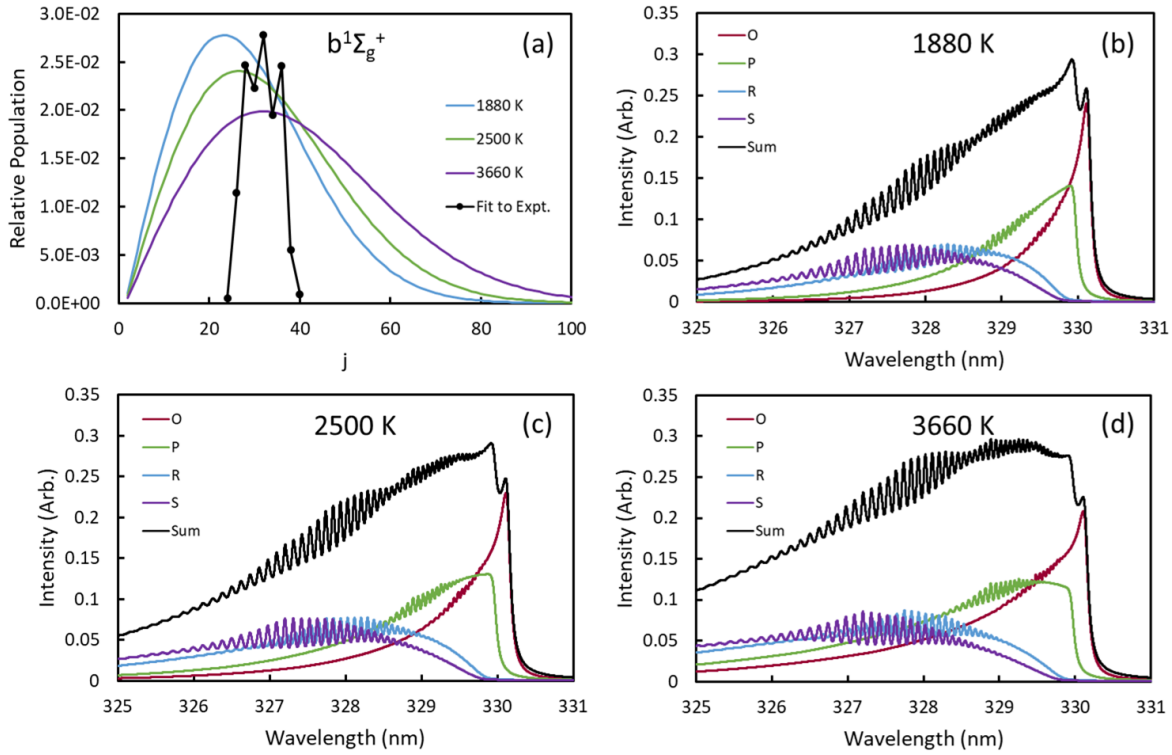

Figure 4.18: (a) The experimental rotational distribution of $O_2(b^1\Sigma_g^+, v = 0)$ is represented by black circles, compared to Boltzmann rotational state distributions for temperatures of 1880 K (blue), 2500 K (green), and 3660 K (purple). (b)-(d) Simulated REMPI spectra using Boltzmann rotational state distributions. The simulated O, P, R, and S branches are shown in maroon, green, blue, and purple, with the sum of the branches shown in black.

distribution for $O_2(b^1\Sigma_g^+, v = 0)$ from Figure 4.16 with Boltzmann distributions for the three temperatures used by Ulrich et al.[71] The distribution obtained from the REMPI spectrum of the $O_2(b^1\Sigma_g^+, v = 0)$ fragment is clearly much narrower than a Boltzmann distribution.

Simulated REMPI spectra for Boltzmann rotational distributions at 1880 K, 2500 K, and 3660 K are shown in (b)-(d) and are much broader and less structured because of the greater overlap between branches.

Probing the molecular fragment indicates the rotational state distributions of $O_2(a^1\Delta_g)$ and $O_2(b^1\Sigma_g^+)$ are both non-Boltzmann and are very different from each other, so the rotational distributions cannot be described by a single temperature.

To confirm the structure in the 330 nm REMPI spectra is not a result of the structured absorbance in the Huggins band, the $O(^3P)$ yield spectrum from O'Keeffe et al.[61] is shown in gray in Figure 4.19 with the $O_2(d^1\Pi_g, v = 4 \leftarrow\leftarrow b^1\Sigma_g^+, v = 0)$ REMPI spectrum from the 2D spectrum shown in black. The high intensity peaks of the REMPI spectrum overlap

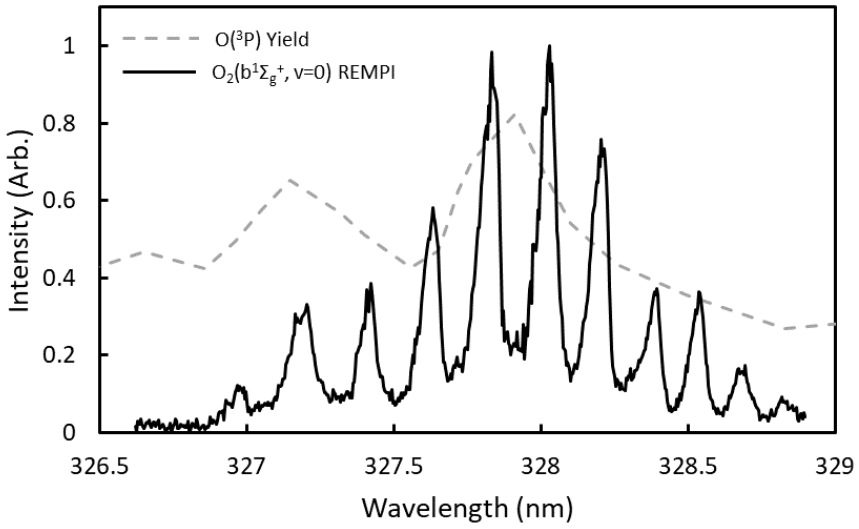

Figure 4.19: The $O_2(d^1\Pi_g, v = 4 \leftarrow\leftarrow b^1\Sigma_g^+, v = 0)$ REMPI spectrum obtained from the 2D-REMPI in Figure 4.14 is shown in black and the $O(^3P)$ yield spectrum from O'Keeffe et al.[61] is represented by the dashed gray line.

with one of the peaks in the $O(^3P)$ yield spectrum, but there is not a corresponding increase in REMPI peak intensity near 327.2 or 326.6 nm. This suggests that the peak intensity is primarily due to differences in rotational state populations rather than O_3 absorbance. Because the REMPI peaks in the $O_2(d^1\Pi_g, v = 1 \leftarrow\leftarrow a^1\Delta_g, v = 0)$ spectrum are consistent with peaks in the $O(^3P)$ yield but the REMPI peaks in the $O_2(d^1\Pi_g, v = 4 \leftarrow\leftarrow b^1\Sigma_g^+, v = 0)$ spectrum are not, the branching ratio between the channels forming $O_2(a^1\Delta_g)$ and $O_2(b^1\Sigma_g^+)$ may change as a function of dissociation wavelength. Additionally, the fragment rotational distribution may depend on the vibrational modes of O_3 excited in the initial absorption. 2-color experiments measuring the O_2 fragment rotational state distributions following dissociation at a single wavelength or additional imaging studies of the $O(^3P)$ fragment both on and off-resonance with O_3 absorbance peaks would provide insight into the wavelength dependence of the branching ratios and rotational distributions of both singlet O_2 fragments.

4.6 $O_2(b^1\Sigma_g^+)$ Ion Images at 330 nm

Ion images of $O_2(b^1\Sigma_g^+)$ were also collected and the corresponding angular distributions were fit to Equation 2.5 to obtain image anisotropy parameters. Images were collected with a vertically polarized laser at wavelengths corresponding to the S-branch transition of j=34 and the R-branch transition of j=32, shown in Figure 4.20. The faint outer ring in the images corresponds to $O_2(a^1\Delta_g, v = 0)$ and moving to smaller radii, the next ring corresponds to $O_2(b^1\Sigma_g^+, v = 0)$ based on the speed distributions. Typically images are collected for two branches of the same rotational state, but because of the overlap of the R and S branches in the REMPI spectrum, nearby rotational states were chosen to minimize contributions from the other branch. The S-branch transition of j=34 overlaps with the R-branch transition of j=40, but the j=40 contribution should be minimal. The R-branch transition of j=32 overlaps

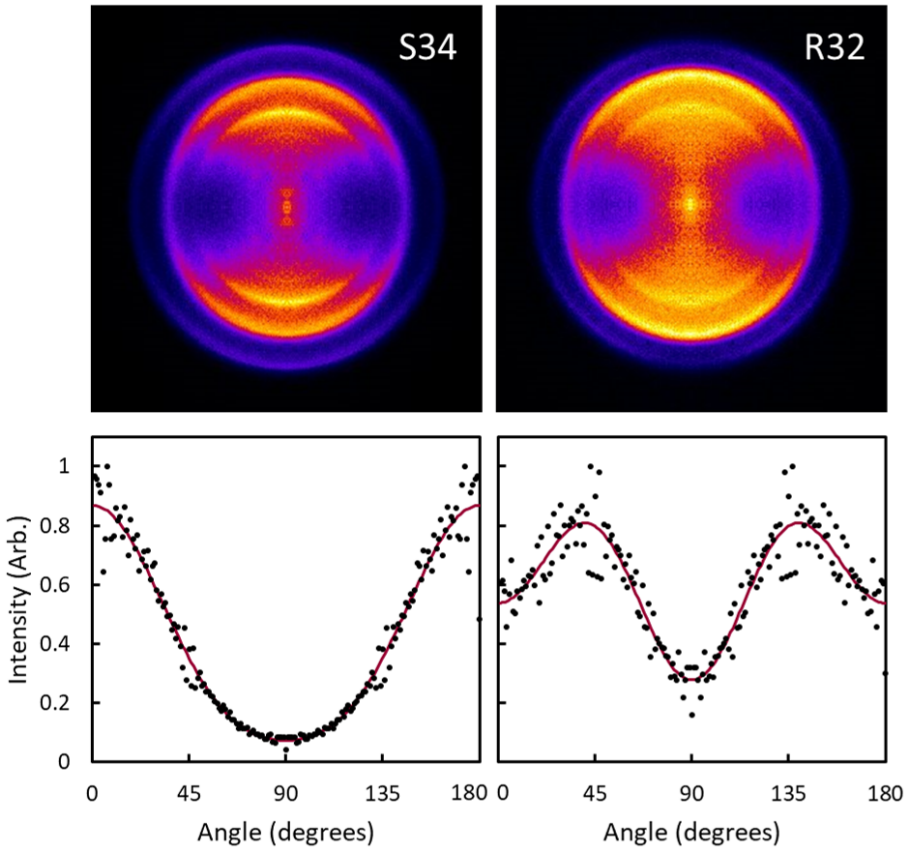

Figure 4.20: Images of the S-branch transition of j=34 and the R-branch transition of j=32 are shown above. The angular distributions of the ring corresponding to the $O_2(b^1\Sigma_g^+, v = 0)$ are shown below. The black circles are the experimental angular distribution and the fit to Equation 2.5 is shown in red.

with the S-branch transition of j=26. Because the fragments in j=26 will be traveling faster than fragments in j=32 following dissociation, the inner edge of the $O_2(b^1\Sigma_g^+)$ ring was used for the angular distribution to minimize contributions from j=26.

The angular distributions of the rings are shown in the bottom of Figure 4.20, with the experimental distribution represented by black circles and the fit to the distribution using Equation 2.5 shown in red. The image anisotropy parameters fit to the distributions are shown in Table 4.7 The angular distribution of the S-branch image has 2-fold symmetry

State	β_2	β_4
S34	1.76 ± 0.08	0.40 ± 0.09
R32	0.56 ± 0.07	-0.62 ± 0.06

Table 4.7: Image anisotropy parameters for the angular distributions in Figure 4.20 obtained by fitting image angular distributions with Equation 2.5.

and the angular distribution of the R-branch image has 4-fold symmetry, as expected for a perpendicular $\boldsymbol{v}$-$\boldsymbol{j}$ correlation. Because of the overlap with the S-branch transition of j=26, the R-branch image appears to have 2-fold symmetry, but the angular distribution below demonstrates that the inner edge of the $O_2(b^1\Sigma_g^+)$ ring does in fact have 4-fold symmetry. The β parameters reported by Ulrich et al. for the $O(^3P_2)$ fragments formed with $O_2(b^1\Sigma_g^+)$ range from -.59 to 1.97, but most values are positive which is consistent with the β_2 values in Table 4.7.

5. PREDISSOCIATION AND LINEWIDTHS

5.1 Rydberg-Valence Interactions in O_2

Interactions between Rydberg and valence states in molecules commonly result in perturbations and predissociation, making them particularly interesting to study.[121] These interactions, however, can also make them difficult to study theoretically. In O_2, interactions between the $O_2(d^1\Pi_g)$ Rydberg state accessed in REMPI schemes and the nearby $O_2(II^1\Pi_g)$ valence state results in predissociation.[74–76] Figure 5.1 from Morrill et al. shows the $d^1\Pi_g$ state on the left indicated by the solid line and the $II^1\Pi_g$ valence state on the right.[74] In this region, the Rydberg state is largely harmonic. The valence state has a shallow well, allowing the repulsive wall above the dissociation threshold to function as a dissociative state in interactions with the higher vibrational levels of the Rydberg state.

The Rydberg and valence states as well as the interactions between them are difficult to study directly because they are high in energy and because the lower energy states of $O_2(X^3\Sigma_g^-$, $a^1\Delta_g$, and $b^1\Sigma_g^+)$ and the higher energy states ($d^1\Pi_g$, and $II^1\Pi_g$) are all gerade so 1-photon transitions between them are forbidden. Additionally, high rotational states of the $O_2(d^1\Pi_g$ and $II^1\Pi_g)$ states cannot be directly accessed from low rotational states of the lower electronic states because of the rotational state selection rule ($\Delta j = 0, \pm 1$). Photodissociation and REMPI experiments provide a unique opportunity to study the Rydberg-valence state interactions of O_2 because photodissociation produces highly rotationally excited O_2 fragments, and 2-photon excitation allows transitions from the $O_2(a^1\Delta_g$ and $b^1\Sigma_g^+)$ states to the $O_2(d^1\Pi_g)$ state. Interactions between the Rydberg and valence states are evident in the structure and variable linewidths in the resulting REMPI spectra of the O_2 fragments.

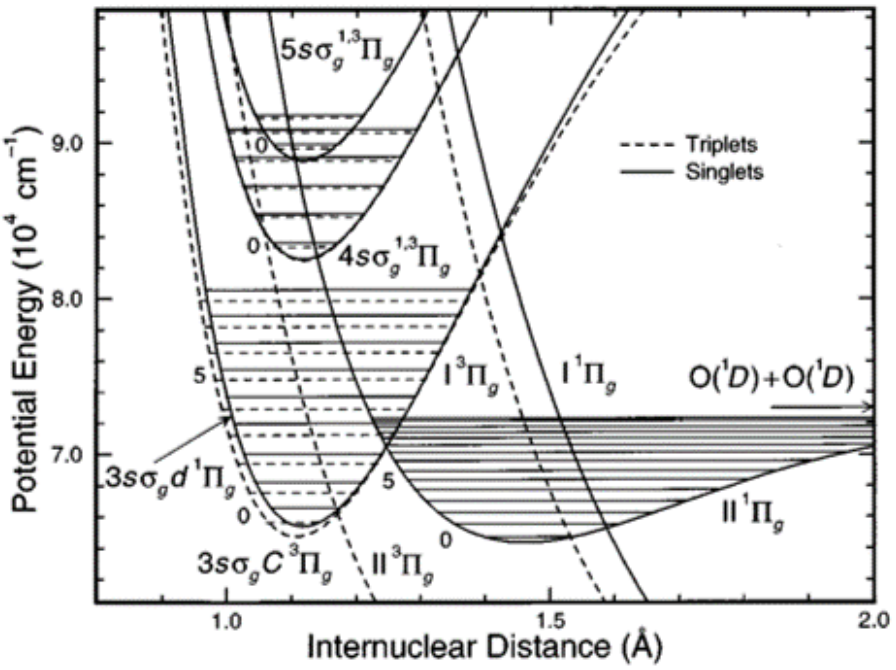

Figure 5.1: Potentials calculated by Morrill et al. for the Rydberg and valence states of O_2.[74] The dashed lines indicate triplet states and the solid lines indicate singlet states. In REMPI schemes of O_2 between 300 and 330 nm, O_2 is excited from the $a^1\Delta_g$ or $b^1\Sigma_g^+$ state to the $d^1\Pi_g$ state, shown on the left. The $d^1\Pi_g$ Rydberg state interacts with the $II^1\Pi_g$ valence state shown on the right, resulting in predissociation. Reprinted from *J. Chem. Phys.* 111, 1, 173-185, 1999, with the permission of AIP Publishing.

5.2 Modeling Spectral Line Shapes and Linewidths

In an experiment, there are many factors that influence the observed line shape and linewidth of peaks in a spectrum. Gaussian, Lorentzian, and Voigt distributions are commonly used to fit spectra depending on which factors are dominant in the peak broadening. As discussed in Chapter 2, Doppler broadening is Gaussian but is negligible for the speeds O_2 fragments travel following dissociation. The laser linewidth (0.1-0.2 cm^{-1}) is also minor and therefore not considered. Lifetime, power, and pressure broadening are all Lorentzian, and lifetime and power broadening are expected to be dominant. A Lorentzian function follows the equation,

$$L = \frac{1}{1 + [\frac{x - x_0}{w/2}]^2} \tag{5.1}$$

where x_0 is the center of the distribution and w is the full width at half maximum of the curve. In comparison to a Gaussian, a Lorentzian profile has greater intensity at the edges of the distribution. A Voigt distribution is a combination of a Gaussian and Lorentzian distribution, but because the Gaussian component is expected to be negligible, a Lorentzian line shape is used for all simulations in this dissertation.

High laser power broadens the peaks in a spectrum, and the effect is largely uniform for all peaks.[102] Lifetime broadening, however, is highly dependent on vibrational and rotational state. When the potential of a repulsive state crosses through the minimum of a bound state potential, transitions from the bound to the repulsive state result in predissociation. The probability of transition depends on the wavefunction overlap between the two states, which can vary significantly across ro-vibrational levels of the bound state. Because of the energy-time uncertainty principle, a shorter lifetime results in a broader spectral linewidth and a

longer lifetime results in a narrower linewidth. The predissociation rates can be calculated if the potentials of both states are known as well as the coupling between them, and the rate can be converted to linewidth with the equation

$$w = \frac{p}{2\pi c} \tag{5.2}$$

where p is the predissociation rate, w is the linewidth and c is the speed of light. The predissociation rates are calculated with the Bound-Continuum (BCONT) program from Le Roy and Kraemer.[103] The BCONT program calculates wavefunctions for given potentials and determines the predissociation rates from the wavefunction overlap and coupling between the states.

ClO predissociation has been previously characterized using experimental measurements of the predissociation rates as a function of ClO vibrational state and modeling the contributions of several dissociative states to the overall predissociation.[122,123] The bound ClO($A^2\Pi$) potential energy curve is shown in Figure 5.2 along with five repulsive states that cross the bound region of the ($A^2\Pi$) state.[123] The dashed lines are from previous calculations and the solid lines were optimized by Dooley et al. to best reproduce the experimentally observed predissociation rates which oscillate as a function of vibrational state. The observed rates can be well-reproduced by including predissociation from the $1^2\Delta$, $1^4\Delta$, $2^4\Sigma^-$, and $3^2\Pi$ states. Repulsive state wavefunctions can be represented by an Airy function with the largest amplitude along the curve, largely unchanging with energy. The potential curve of the $1^2\Delta$ state is along the repulsive wall of the $A^2\Pi$ state, so the wavefunction overlap will not be highly variable with vibrational state and the predissociation rates resulting from $1^2\Delta$ state interactions with the $A^2\Pi$ state as a function of vibrational state will be a smooth function. In

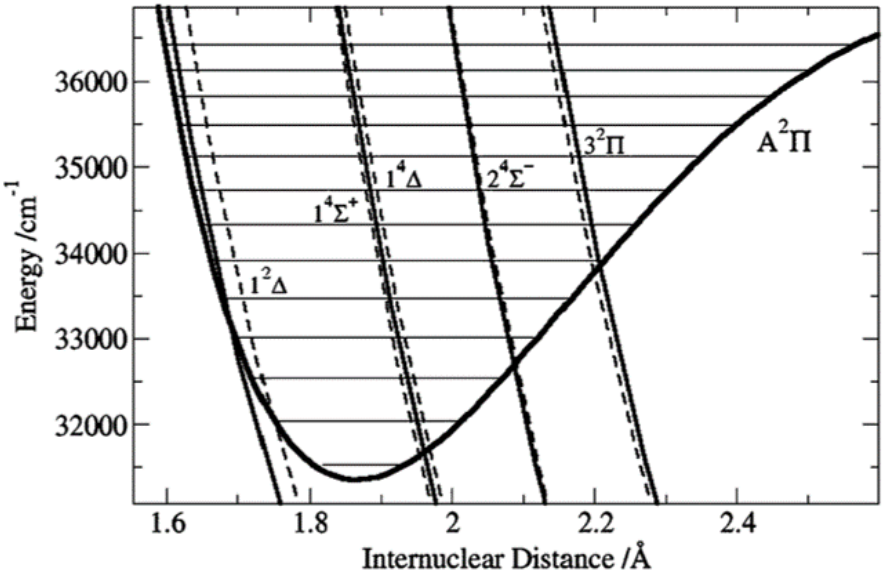

Figure 5.2: Potential energy curves from Dooley et al. for ClO($A^2\Pi$) and several repulsive states that lead to predissociation.[123] The dashed lines are from previous calculations and the solid lines represent the authors' optimization of the potentials. Used with permission of Royal Society of Chemistry, from Correlated fine structure branching ratios arising from state-selected predissociation of ClO($A^2\Pi_{3/2}$), Dooley, K., et al., *Phys. Chem. Chem. Phys.* 11, 23, 4770-4776, 2009, permission conveyed through Copyright Clearance Center, Inc.

contrast, for repulsive states that cut through the middle of the bound potential, the high amplitude region of the repulsive state interacts with high amplitude regions of some vibrational states and low amplitude regions of other vibrational states, resulting in very different wavefunction overlap and predissociation rates. As a result, the predissociation rates resulting from interactions of the $1^4\Delta$, $2^4\Sigma^-$, and $3^2\Pi$ states with the $A^2\Pi$ as a function of vibrational state will oscillate. The wavefunction overlap and resulting predissociation rates are highly dependent on the relative positions of the potentials. Small shifts of the repulsive potentials to shorter or longer radii can produce very different rates of predissociation.

5.3 O_2 Predissociation

REMPI schemes of $O_2(a^1\Delta_g)$ and $O_2(b^1\Sigma_g^+)$ between 300 and 330 nm excite O_2 to the $d^1\Pi_g$ Rydberg state, which interacts with the nearby $II^1\Pi_g$ valence state. In this energy range, O_2 is excited to the bound region of the $d^1\Pi_g$ state. The $II^1\Pi_g$ state is bound, but the repulsive wall above the dissociation threshold interacts with the Rydberg state, so it can be treated as dissociative.

Van der Zande et al. previously studied the interactions of the $d^1\Pi_g$ and $II^1\Pi_g$ states of O_2 by measuring the linewidth in translational spectroscopy experiments and by calculating expected linewidths with Fermi golden rule assuming a constant coupling of 450 cm^{-1} between the Rydberg and valence states.[75] The authors reported experimental and calculated vibrational state dependent linewidths for j=1 of $^{16}O_2$ and $^{18}O_2$ and rotational state dependent linewidths for v=4 of $^{16}O_2$ and $^{18}O_2$ and v=6 of $^{18}O_2$. However, the reported trends only extended to j=25, and in some cases only an upper bound of the experimental linewidth was reported. Linewidths for j=1 increase between v=4 and v=5, which is the vibrational state with the broadest calculated linewidth, and decrease between v=5 and v=7. The cal-

culated linewidths for $^{16}O_2(v = 4)$ decrease with increasing j, and the calculated linewidths for $^{18}O_2(v = 6)$ increase with increasing j. Linewidths for $^{18}O_2(v = 4)$ oscillate. Li et al. performed ab initio calculations for the O_2 Rydberg and valence state potentials and reported the potentials as well as the R-dependent coupling between the states, which exponentially decays with increasing R.[76] The authors reported the resulting linewidths for v=0-7, j=1-25 of $^{16}O_2$ and $^{18}O_2$. The v-dependent linewidth trend was similar to that reported by van der Zande et al. but the linewidth for v=5, j=1 from Li et al. was much higher. The calculated j-dependent trends for $^{16}O_2(v = 4)$ and $^{18}O_2(v = 4, 6)$ are also consistent with the trends reported by van der Zande et al.

More recently, Han et al. used j-dependent linewidths to fit the REMPI spectrum of O_2 following 266 nm dissociation of O_3 probed via the $O_2(d^1\Pi_g, v = 4 \leftarrow\leftarrow a^1\Delta_g, v = 0)$ transition.[6] The authors used an exponential function to estimate the decrease in linewidth as a function of increasing rotational state.

Previous calculations included rotational states j=1-25 and Han et al. used a simple function for a global fit of the REMPI spectrum. More complex trends in linewidth can be calculated with the BCONT program and used to fit experimental spectra, but to better assess the potentials and coupling used in the BCONT calculations, additional experimental measurements were needed. Probing O_2 following a higher energy dissociation of O_3 at 226 nm affords access to higher rotational states of the O_2 fragment, and the linewidths of these peaks in the REMPI spectrum can be compared to calculated predissociation rates to refine the parameters used in the calculations.

5.4 Optimization of Potentials for Calculating Linewidths

The calculated predissociation rates are minimally sensitive to shifting the potentials in energy relative to each other but are highly sensitive to shifting the valence potential to shorter or longer radii relative to the Rydberg potential. Figure 5.3 shows the j-dependent

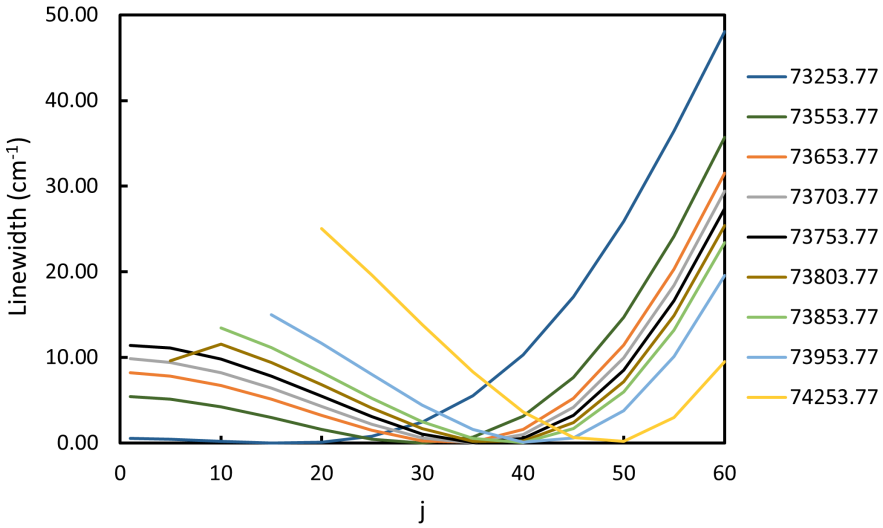

Figure 5.3: Calculated linewidths for $O_2(d^1\Pi_g, v = 4)$ as a function of j for shifts in the energy of the valence state. Each curve is labeled by the asymptotic energy of the valence state in cm^{-1}.

trend in linewidth for $O_2(d^1\Pi_g, v = 4)$ where each line represents a different shift in the asymptotic energy of the valence state. The asymptotic energy corresponding to each curve in cm^{-1} is indicated in the legend. The initial set of linewidths was calculated with a valence state asymptotic energy of 73753.77 cm^{-1}. For small changes in energy (50-100 cm^{-1}) the changes in calculated linewidths are subtle and the trend as a function of j is largely the

same. For large shifts in energy (200-500 cm^{-1}) the trend as a function of j changes more significantly. At lower valence state energies, the linewidths are smaller at lower rotational states and increase more rapidly with increasing j. At higher valence state energies, the linewidths are much larger at low rotational states and reach a minimum at higher rotational states before increasing again. Because the calculations only work for transitions to the continuum region of the valence state, shifting the valence state to high enough energies prevents predissociation of the lower energy rotational states because the shallow bound region of the valence state becomes similar in energy to the lower ro-vibrational states of the Rydberg state.

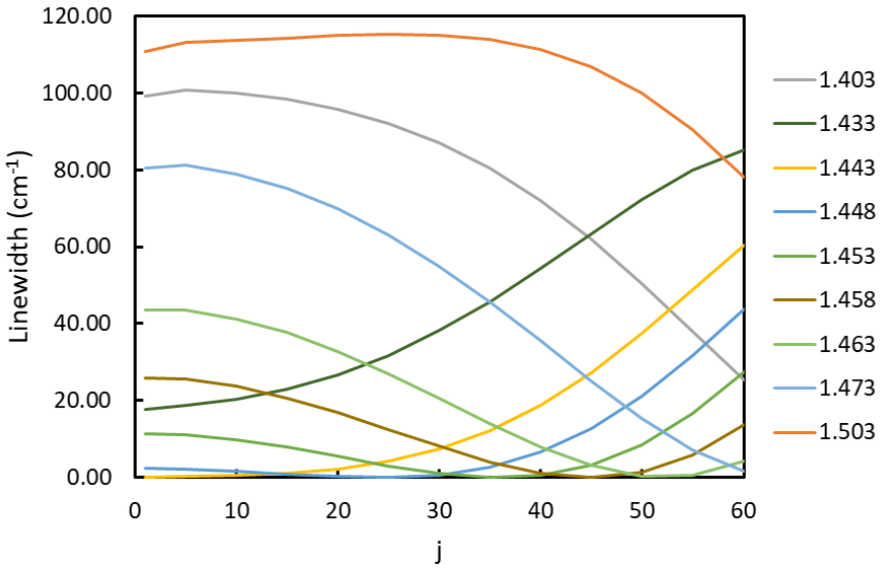

Figure 5.4: Calculated linewidths for $O_2(d^1\Pi_g, v = 4)$ as a function of j for shifts in the radius of the valence state. Each curve is labeled by the equilibrium radius in Å of the valence state.

Figure 5.4 shows the j-dependent trend in linewidth for $O_2(d^1\Pi_g, v = 4)$ where each line represents a shift in radius of the valence state, labeled by the equilibrium radius in Å. The initial set of linewidths was calculated with a radius of 1.453 Å at the minimum of the valence state potential. At this radius, the linewidths initially decrease with increasing j, reaching a minimum near j$\sim$35, and begin to increase as j continues to increase. As the potential is shifted to longer radii, the linewidths increase at lower rotational states and the minimum linewidth shifts to higher rotational states. Between 1.473 and 1.503 Å, the linewidths are large at low rotational states and decrease with increasing j. As the radius shifts to smaller radii from 1.453 Å, the linewidths decrease at low rotational states and increases more quickly with increasing j. Between 1.443 and 1.433 Å, the linewidths increase for all j, and between 1.433 and 1.403 Å, the trend in linewidth changes significantly, and at 1.403 Å, linewidths are large at low rotational states and decrease with increasing rotational state.

The effect of the coupling between the Rydberg and valence states on the calculated linewidths is shown in Figure 5.5. All j-dependent linewidth trends were calculated with a constant coupling that did not depend on radius (R). The initial set of linewidths was calculated with a coupling of 525 cm^{-1}. As the coupling is increased or decreased, the shape of the linewidth trend as a function of j is unchanging, all reaching a minimum in linewidth near j=35. The calculated linewidths at both low and high rotational states increase with increasing coupling and decreases with decreasing coupling.

The j-dependent linewidth trends change very little with shifts in energy but depend strongly on the relative equilibrium radii of the two potentials and the coupling between them, so adjustments were primarily made to these two parameters until the calculated

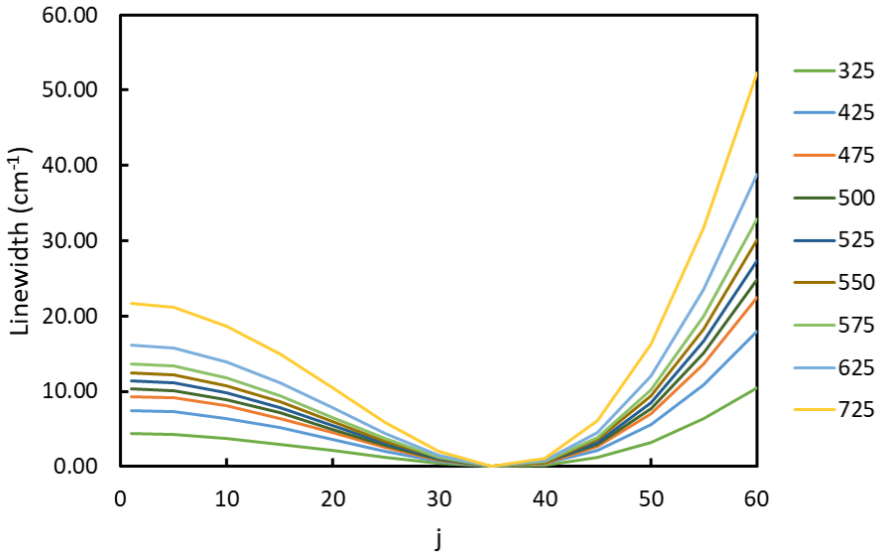

Figure 5.5: Calculated linewidths for $O_2(d^1\Pi_g, v = 4)$ as a function of j. Each line indicates a different strength of coupling between the Rydberg and valence states, labeled by coupling in cm^{-1}.

linewidths were consistent with previous calculations and experimental measurements.

5.5 Comparison of Calculated Linewidths to Experimental Measurements

Previous measurements and calculations of the linewidths of individual spectral peaks were only extended to j=25 of the $d^1\Pi_g$ state, but the rotational distribution of $O_2(a^1\Delta_g)$ following 226 nm dissociation peaks at j=40, so the REMPI spectrum of $O_2(d^1\Pi_g, v = 4 \leftarrow\leftarrow a^1\Delta_g, v = 0)$ discussed in Chapter 3 allows measurement of the linewidths of higher rotational states than previously studied. Individual peaks in the REMPI spectrum following 266 nm dissociation of O_3 from Han et al.[6] were fit to obtain experimental linewidths of lower rotational states and the REMPI spectrum following 226 nm dissociation from Chapter 3 was used for linewidth measurements of higher rotational states. Peaks with minimal overlap

from other rotational branches were selected for individual fitting. The measured linewidths decrease with increasing j until j$\sim$35 where the linewidths reach a minimum. As j increases to rotational states j>35, the linewidths increase.

To model the observed j-dependent linewidth trend, the diabatic potentials calculated by Li et al. were fit with Morse potentials and used as a starting point in the BCONT calculations.[76] The valence state was shifted by 0.051 Å to shorter radii from the original fit and an R-independent coupling of 575 cm^{-1} was used to best reproduce the previously calculated and experimentally observed trends. A comparison of the j-dependent linewidth trends for $O_2(d^1\Pi_g, v = 4)$ are shown in Figure 5.6. The linewidths from van der Zande et al. were calculated using previously calculated potentials and Fermi golden rule with an R-independent coupling to determine the rate of transition between the Rydberg and valence states.[75,124] The authors shifted the valence state and adjusted the coupling between the states to reproduce experimentally measured linewidths. New potentials were later calculated by Li et al. along with an R-dependent coupling between the Rydberg and valence states.[76] The potentials were again shifted to match experimental linewidths. The linewidths calculated with the BCONT program reproduce the previous trends well. However, the experimentally measured linewidths are broader than calculated linewidths. This is likely due to peak broadening from high laser power because the effect is largely uniform across rotational states and this effect has been previously observed at lower laser powers.[108]

The optimized potentials used in the BCONT calculations are shown in Figure 5.7. The 575 cm^{-1} coupling in the BCONT calculations is higher than the constant 450 cm^{-1} coupling used by van der Zande et al.[75] The R-dependent coupling used by Li et al. has an average of 970 cm^{-1} between 1.15 and 1.20 Å.[76] Linewidths calculated with a constant coupling match

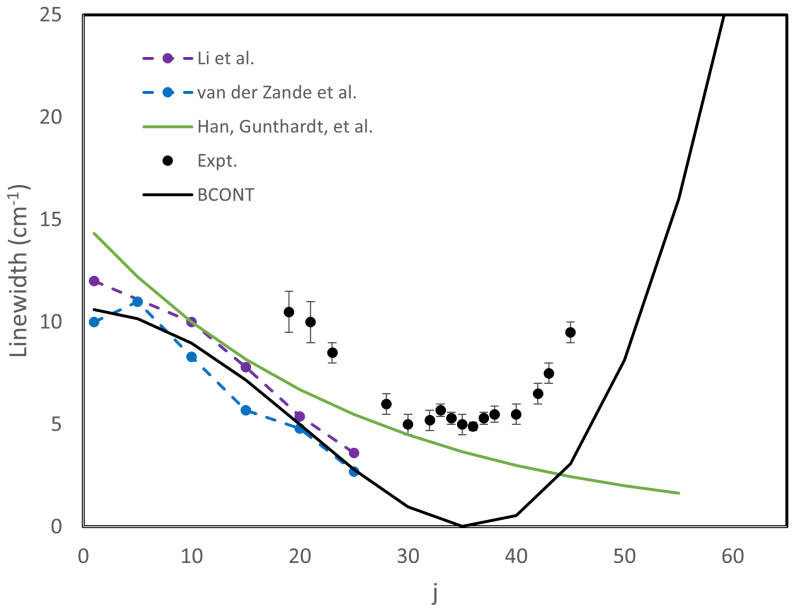

Figure 5.6: Calculated linewidths from Li et al. and van der Zande et al. are shown in purple and blue, respectively.[75,76] The exponential function used by Han et al. to model the decrease in linewidth as a function of j is shown in green.[6] The black circles represent fits to individual peaks in REMPI spectra of O_2 following dissociation at 266 nm[6] and 226 nm. The solid black line is the j-dependent linewidth trend calculated with the BCONT program. Reprinted with permission from Aardema et al. *J. Phys. Chem. A* 2022, 126, 39, 6898-6907. Copyright 2022 American Chemical Society.

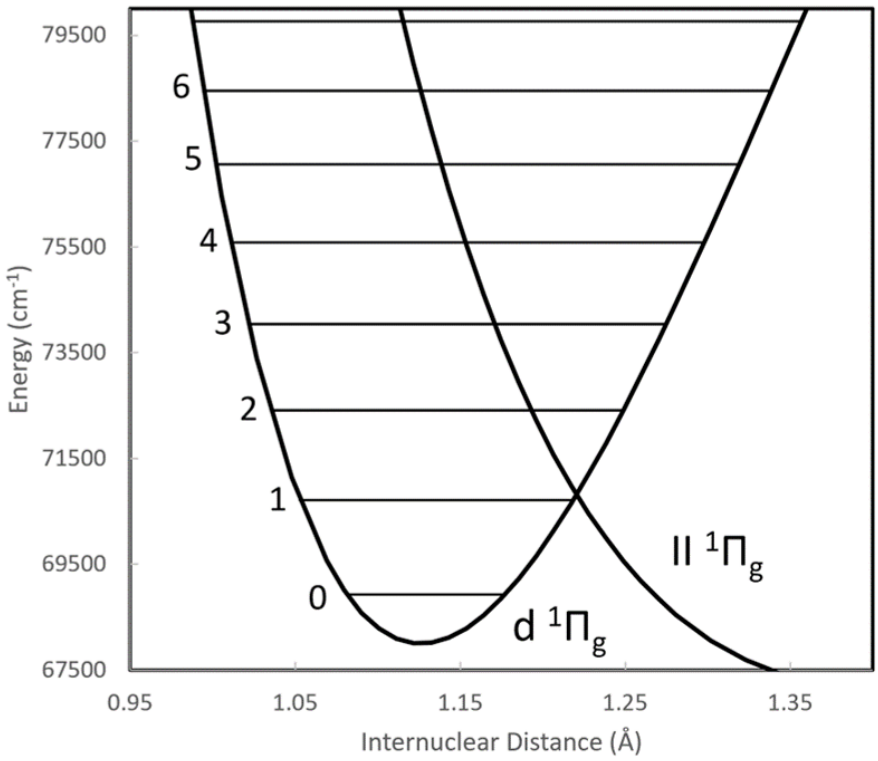

Figure 5.7: Potential energy curves for $O_2(d^1\Pi_g)$ and $O_2(II^1\Pi_g)$ used in BCONT calculations of predissociation rates and the corresponding linewidths as a function of j. The potentials are Morse potentials fit to the potentials calculated by Li et al.,[76] and the $II^1\Pi_g$ potential is shifted 0.051 Å to shorter radii to best reproduce the trend in experimental linewidths. Reprinted with permission from Aardema et al. *J. Phys. Chem. A* 2022, 126, 39, 6898-6907. Copyright 2022 American Chemical Society.

experimental trends well for $^{16}O_2(v = 4)$, so a constant coupling was used. The BCONT input file corresponding to the optimized potentials is included in Appendix B.

Figure 5.8 shows the linewidths calculated by BCONT as a function of j for $^{16}O_2$ and $^{18}O_2$ in v=4-7. Linewidths as a function of vibrational state were also calculated for j=1 of both isotopes, shown in Figure 5.9. All BCONT linewidths are shown in black. The linewidths previously calculated by Li et al. and van der Zande et al. are shown in purple and blue, respectively.[75,76] The j-dependent trends for v=4 in both isotopes is reproduced well, with the BCONT calculations falling between the two previous calculations. For v=5, the linewidths calculated with the BCONT program are large and relatively unchanging at low j, consistent with the calculations from Li et al. The trend for $^{16}O_2$ (v=6) calculated with BCONT is opposite the trend calculated by Li et al., but all three sets of calculations show a gradual increase in linewidth as a function of j for the $^{18}O_2$ isotope. The BCONT linewidths, however, are much larger than previous calculations for $^{18}O_2$. The trends calculated for v=7 of both isotopes are not consistent with the calculations of Li et al. The v-dependence of the linewidths increases between v=4 and v=5 for all calculations and both isotopes. The BCONT calculation for $^{16}O_2$, v=6 continues to increase before decreasing at v=7, but previous calculations of the $^{16}O_2$ isotope predict decreasing linewidths between v=5 and v=7. Previous calculations for the $^{18}O_2$ isotope predict a sharp decrease in linewidth at v=6, which is not reproduced in the BCONT calculations, but the BCONT prediction for v=7 is consistent with both Li et al. and van der Zande et al.

Some of the deviations between the linewidths calculated with BCONT and the previous calculations may be due to the use of an R-independent coupling between the Rydberg and valence states, and a more complex coupling function could result in better fits. Overall,

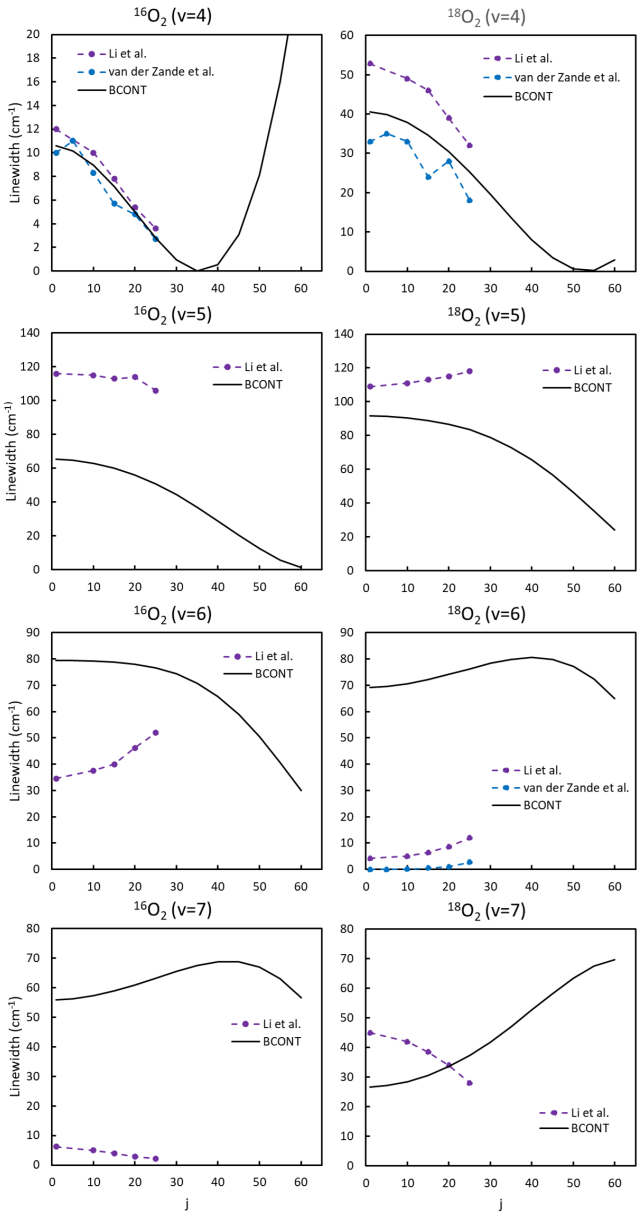

Figure 5.8: Linewidths calculated with the BCONT program for v=4-7 and j=1-60 of the $^{16}O_2$ and $^{18}O_2$ isotopes. BCONT linewidths are shown in black and compared to previous calculations from Li et al. and van der Zande et al., shown in purple and blue, respectively.[75,76] Reprinted (adapted) with permission from Aardema et al. *J. Phys. Chem. A* 2022, 126, 39, 6898-6907. Copyright 2022 American Chemical Society.

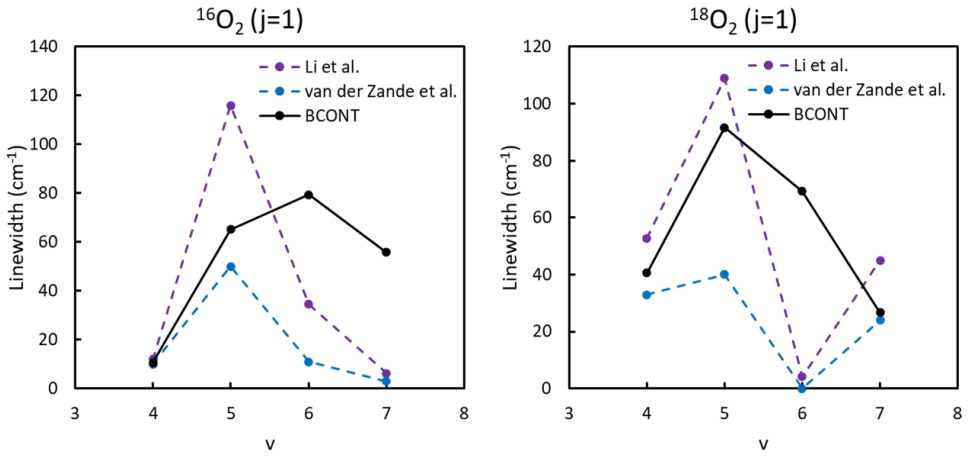

Figure 5.9: Linewidths calculated with the BCONT program for v=4-7, j=1 of the $^{16}O_2$ and $^{18}O_2$ isotopes. BCONT linewidths are shown in black and previously calculated linewidths from Li et al. and van der Zande et al. are shown in purple and blue, respectively.[75,76] Reprinted (adapted) with permission from Aardema et al. *J. Phys. Chem. A* 2022, 126, 39, 6898-6907. Copyright 2022 American Chemical Society.

however, many features of the j- and v-dependence of the linewidths are well-reproduced. A complete list of the calculated linewidths is shown in Table 5.1 and the experimental linewidths in Table 5.2. Variable linewidths were used to fit the $O_2(d^1\Pi_g, v = 4 \leftarrow\leftarrow a^1\Delta_g, v = 0)$ REMPI spectrum following 226 nm dissociation of O_3 discussed in Chapter 3. The linewidths used follow the trend of the individually fit REMPI peaks indicated by the black circles in Figure 5.6 and are extrapolated to higher rotational states following the trend calculated with BCONT.

The potentials used in the BCONT calculations were later adjusted so that the vibrational spacing of the $O_2(d^1\Pi_g)$ state matched calculations from Morrill et al. using a model that considers nearby Rydberg and valence states and the interactions between them.[74] Morrill et al. reported two energies for v=2 because this level interacts with the nearly degenerate v=8

j	$^{16}O_2$ v=4	$^{16}O_2$ v=5	$^{16}O_2$ v=6	$^{16}O_2$ v=7	$^{18}O_2$ v=4	$^{18}O_2$ v=5	$^{18}O_2$ v=6	$^{18}O_2$ v=7
1	10.6	65.3	79.4	55.8	40.6	91.6	69.3	26.7
5	10.2	64.7	79.4	56.2	39.9	91.4	69.6	27.2
10	9.0	62.9	79.3	57.2	37.9	90.5	70.7	28.5
15	7.2	60.1	78.9	58.8	34.7	89.0	72.2	30.6
20	5.0	56.0	78.1	60.9	30.4	86.8	74.2	33.6
25	2.8	50.8	76.7	63.2	25.3	83.5	76.3	37.4
30	1.0	44.4	74.4	65.5	19.6	79.0	78.4	41.9
35	0.03	37.0	70.8	67.5	13.6	73.1	79.9	47.1
40	0.6	28.9	65.7	68.7	8.1	65.7	80.6	52.7
45	3.1	20.5	59.0	68.7	3.5	56.7	79.9	58.3
50	8.2	12.5	50.6	66.9	0.6	46.5	77.2	63.5
55	16.0	5.8	40.7	62.9	0.2	35.3	72.3	67.6
60	26.7	1.3	29.9	56.5	3.0	24.1	64.9	69.8

Table 5.1: Linewidths for v=4-7 and j=1-60 of the $^{16}O_2$ and $^{18}O_2$ isotopes calculated with the BCONT program. The potentials were obtained by fitting the potentials calculated by Li et al.[76] with Morse functions, shifting the valence state potential to shorter radii, and adjusting the coupling between the Rydberg and valence states to reproduce previously calculated and experimentally measured trends. Reprinted (adapted) with permission from Aardema et al. *J. Phys. Chem. A* 2022, 126, 39, 6898-6907. Copyright 2022 American Chemical Society.

of the valence state. Once the calculations were consistent, the rotational constants associated with the vibrational levels of the new potential provided a reasonable approximation for fitting the REMPI spectra discussed in Chapter 4. The $O_2(d^1\Pi_g)$ state potential was adjusted by changing the well depth and the broadness of the potential and comparing the vibrational levels after each iteration. The new $O_2(d^1\Pi_g)$ potential is shown in black in Figure 5.10 in comparison to the original Morse potential fit to the calculations of Li et al., shown in gray.[76] A comparison of the calculated energies of each vibrational level is shown in Table 5.3.

Predissociation rates and linewidths were re-calculated with the new potentials for v=4-8

j	$^{16}O_2(v=4)$
19	10.5 $\pm$1
21	10 $\pm$ 1
23	8.5 $\pm$ 0.5
28	6.0 $\pm$ 0.5
30	5.0 $\pm$ 0.5
32	5.2 $\pm$ 0.5
33	5.7 $\pm$ 0.3
34	5.3 $\pm$ 0.3
35	5.0 $\pm$ 0.5
36	4.9 $\pm$ 0.2
37	5.3 $\pm$ 0.3
38	5.5 $\pm$ 0.4
40	5.5 $\pm$ 0.5
42	6.5 $\pm$ 0.5
43	7.5 $\pm$ 0.5
45	9.5 $\pm$ 0.5

Table 5.2: Linewidths fit to individual peaks in experimental spectra of O_2 probed via the $O_2(d^1\Pi_g, v=4 \leftarrow\leftarrow a^1\Delta_g, v=0)$ transition following dissociation at 266 nm from Han et al.[6] and 226 nm discussed in Chapter 3. Reprinted with permission from Aardema et al. *J. Phys. Chem. A* 2022, 126, 39, 6898-6907. Copyright 2022 American Chemical Society.

and j=1-60 of the $^{16}O_2$ isotope. The valence state potential was shifted by 0.44 Å to longer radii compared to the potential previously used for linewidth calculations and the coupling between the $d^1\Pi_g$ and $II^1\Pi_g$ states was decreased from 575 cm^{-1} to 525 cm^{-1} to best match the experimentally measured linewidths for $O_2(d^1\Pi_g, v=4)$. The previously used valence state potential was shifted 0.051 Å to shorter radii from the original fit to calculations from Li et al., and the new potential is shifted 0.44 Å back to longer radii, resulting in a potential very close to the original calculations. The coupling constant of 525 cm^{-1} is also closer than the previously used 575 cm^{-1} to the coupling of 450 cm^{-1} used by van der Zande et al.[75] The

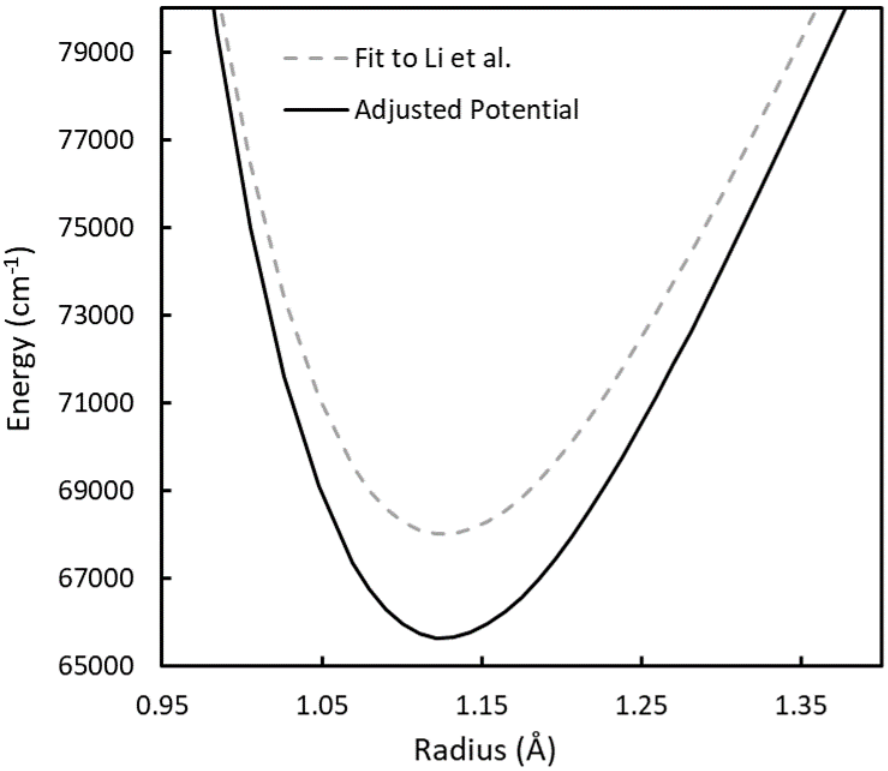

Figure 5.10: The Morse function initially fit to the calculated potential from Li et al. is shown in gray, and the optimized potential corresponding to similar vibrational level energies to Morrill et al. is shown in black.[74,76]

	BCONT	Morrill et al.[74]
v=0	66327.1 cm^{-1}	66356 cm^{-1}
v=1	68239.1 cm^{-1}	68226 cm^{-1}
v=2	70115.7 cm^{-1}	70011 cm^{-1}
		70142 cm^{-1}
v=3	71956.8 cm^{-1}	71950 cm^{-1}
v=4	73762.4 cm^{-1}	73740 cm^{-1}
v=5	75532.6 cm^{-1}	75485 cm^{-1}
v=6	77267.3 cm^{-1}	77196 cm^{-1}
v=7	78966.6 cm^{-1}	78924 cm^{-1}
v-8	80630.4 cm^{-1}	80596 cm^{-1}

Table 5.3: The energy of vibrational levels v=0-8 of the $O_2(d^1\Pi_g)$ were calculated with BCONT and the potential used was adjusted until the energy levels matched previous calculations of Morrill et al.[74]

asymptote of the valence state was decreased by 30 cm^{-1} so predissociation of all rotational levels of $O_2(d^1\Pi_g, v = 4)$ could be calculated above the dissociation threshold, and this small shift should have a very minor effect on the calculated rates for the other ro-vibrational levels. The BCONT input file used in these calculations is included in Appendix B. To calculate predissociation rates for the $^{18}O_2$ isotope, the asymptote of the valence state would need to be shifted more significantly, so calculations were not performed for the predissociation rates of $^{18}O_2$.

The linewidths calculated with the BCONT program for v=4-8 and j=1-60 of $^{16}O_2$ are shown in Figure 5.11 in black. Previous calculations from Li et al. and van der Zande et al. are shown in purple and blue, respectively.[75,76] The previously calculated trends are all well-reproduced by the BCONT calculations. The linewidths calculated with BCONT for v=5 are larger than the calculations from Li et al., but the trend is very similar. For v=7, the trend

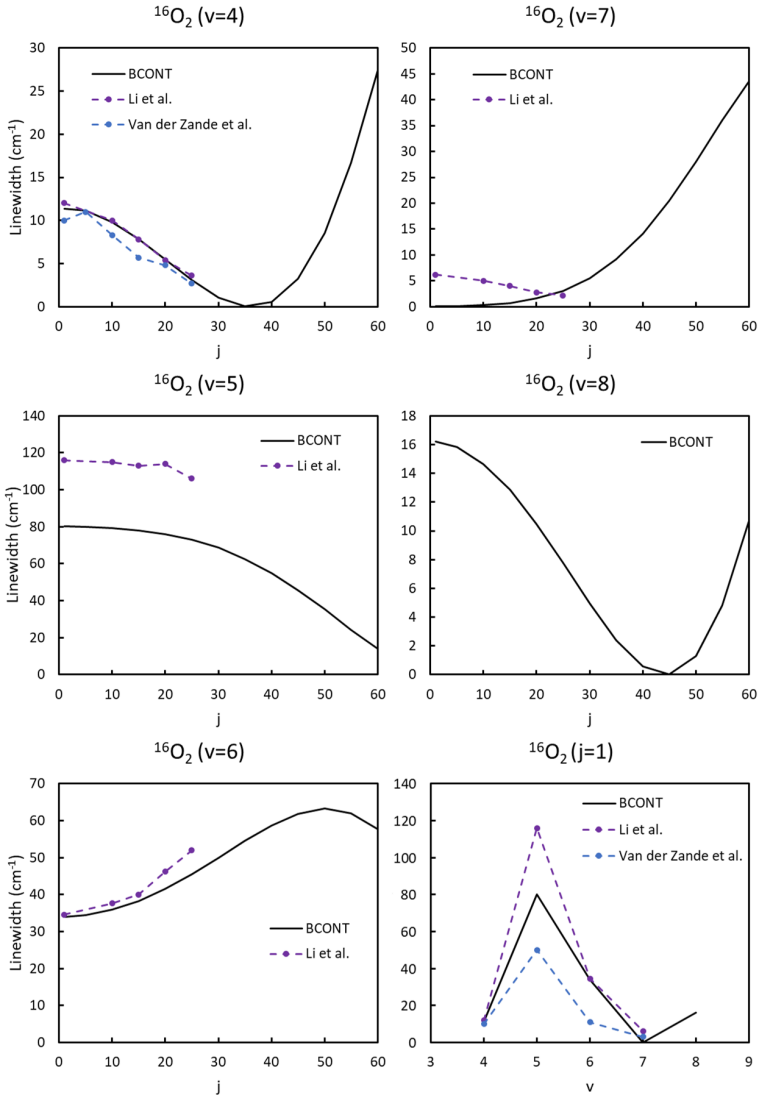

Figure 5.11: Linewidths are shown as a function of j for $^{16}O_2(v = 4-8)$ in black, determined from predissociation rates calculated by the BCONT program. The calculated linewidths are compared to previous calculations from Li et al. and van der Zande et al., shown in purple and blue, respectively.[75,76] The bottom right plot shows the v-dependence of the linewidth for j=1.

calculated with BCONT is opposite of the trend calculated by Li et al., but the magnitude is similar. Linewidths were also calculated for v=8 despite the lack of previous calculations for comparison because v=8 is accessed in the 2D REMPI discussed in Chapter 4. The v-dependence of the linewidths for j=1 is also well-reproduced. All calculated linewidths are similar for j=1 of v=4 and v=7, and the linewidths calculated with BCONT for v=5 and 6 fall between the linewidths from previous calculations. A complete list of the linewidths calculated with the adjusted potentials is shown in Table 5.4.

	$^{16}O_2$	$^{16}O_2$	$^{16}O_2$	$^{16}O_2$	$^{16}O_2$
j	v=4	v=5	v=6	v=7	v=8
1	11.4	80.3	33.9	0.1	16.2
5	11.1	80.0	34.4	0.2	15.8
10	9.8	79.4	35.9	0.3	14.7
15	7.8	78.1	38.3	0.7	12.8
20	5.5	76.1	41.5	1.6	10.5
25	3.1	73.0	45.5	3.1	7.8
30	1.1	68.6	49.9	5.5	4.9
35	0.04	62.6	54.5	9.2	2.4
40	0.6	55.0	58.7	14.2	0.6
45	3.2	45.8	61.9	20.5	0.02
50	8.5	35.3	63.2	28.0	1.3
55	16.6	24.3	62.0	36.0	4.8
60	27.4	13.9	57.6	43.6	10.7

Table 5.4: Linewidths for v=4-8 and j=1-60 of the $^{16}O_2$ isotope calculated with the BCONT program. The linewidths were obtained by fitting the potentials calculated by Li et al.[76] with Morse functions, optimizing the parameters to reproduce $O_2(d^1\Pi_g)$ vibrational level energies reported by Morrill et al.,[74] and adjusting the valence state potential equilibrium radius and coupling between the Rydberg and valence states to reproduce experimental linewidths for v=4.

The calculated linewidths were used as a starting point for fitting the REMPI spectra of the 4-0, 5-1, 6-2, 7-3, and 8-4 bands of the $O_2(d^1\Pi_g \leftarrow\leftarrow b^1\Sigma_g^+)$ transition, but because there was no experimental data from previous studies to verify the calculated linewidths for most of the $O_2(d^1\Pi_g)$ vibrational levels, the linewidths were adjusted to best fit the data. The linewidths used in fitting the spectra in Chapter 4 are shown in Table 5.5. Similar to the calculated linewidths, the linewidths used to fit the 5-1 spectrum are larger at low rotational states and decrease with increasing j, but the curvature of the trend is different than that predicted by the BCONT calculations. The calculated linewidths for v=6 increase with increasing j, reaching a maximum near j=50, but the linewidths used to fit the 6-2 spectrum decrease with increasing j, reaching a minimum near j=37. The calculated linewidths for v=7 increase quickly with increasing j, but the linewidths used to fit the 7-3 spectrum again follow the opposite trend, decreasing with increasing j. The trend in calculated and experimental linewidths for v=8 are similar, decreasing initially with increasing j and reaching a minimum near j=40 before increasing again, but the minimum experimental linewidth is larger than the calculated minimum, which may be due to power broadening, as seen for v=4.

Figure 5.12 shows a comparison of the vibrational state dependence of the linewidths for j=30 and 40, which correspond to rotational states assigned to the spectra in Chapter 4, rather than j=1 which was used in previously calculations and shown in Figure 5.11. The linewidths used to fit the experimental spectra are similar for j=30 and 40 in v=4, 5, and 8. In v=6 and 7, the linewidth for j=30 is larger than j=40. The linewidths calculated with the BCONT program increase from v=4 to v=5, are large in v=5 and 6, and decrease in v=7 and 8. The experimental linewidths are larger in v=6 and 7 than v=4, 5, and 8, but are much smaller than the largest linewidths predicted by the BCONT calculations. The experi-

	Linewidth (cm^{-1})				
j	v=4	v=5	v=6	v=7	v=8
22					18
23					18
24					18
25	15.5	18	41		18
26	15	17	39.5		18
27	14.5	16	37		17.75
28	14	15	34		17.5
29	13.5	14	31	28	17.25
30	13	13	29	28	17
31	12.5	12	26	27	16.75
32	12	12	23	26	16.5
33	12	12	20	24	16.25
34	12	12	18	22	15.75
35	12	12	16	20	15.25
36	12	12	14.5	19	14.75
37	12	12	14	18	14.25
38	12	12	14	17	14
39	13	12	14.5	16	14
40	14	12	15	15	14.5
41	15.5	12	16	14	15
42	17	12	17	13.5	15.5
43		12	18	13	16
44		12	19	12.5	17
45			20	12	18
46			21	12	20
47			22		22
48			23		

Table 5.5: Linewidths used in fitting the REMPI spectra of the 4-0, 5-1, 6-2, 7-3, and 8-4 bands of the $O_2(d^1\Pi_g \leftarrow\leftarrow b^1\Sigma_g^+)$ transition shown in Chapter 4.

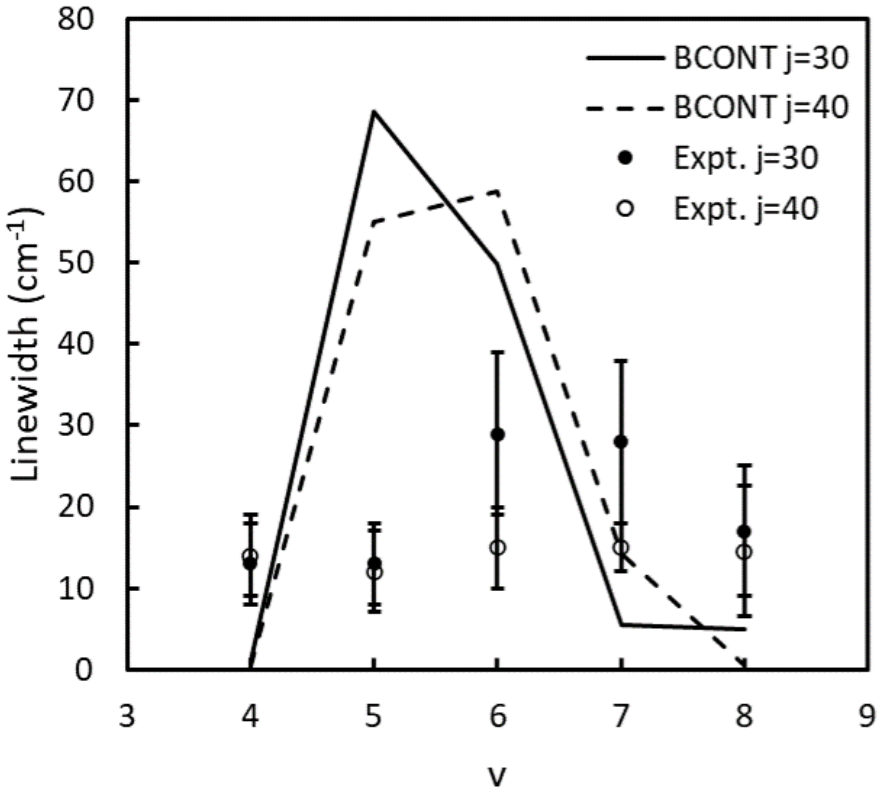

Figure 5.12: The linewidths calculated with the BCONT program for j=30 and j=40 are shown by solid and dashed lines, respectively, as a function of $^{16}O_2(d^1\Pi_g)$ vibrational state. The linewidths for j=30 and j=40 used in the fits to the experimental spectra in Chapter 4 are represented by the closed and open circles, respectively.

mental linewidths are larger than the calculated linewidths for v=4 and v=8, but the observed linewidths also contain contributions from power broadening, so the experimental linewidths in Figure 5.12 represent an upper bound of the peak broadening due to predissociation. Previous calculations predicted a large increase in the linewidth of v=5, which is reproduced for j=1 as shown in Figure 5.11. However, the observed linewidths for higher rotational states of v=5 are much smaller than predicted.

Figure 5.13 shows a comparison of the potentials used in the calculations. The Morse potentials initially fit to the potentials calculated by Li et al. are shown by the dashed gray lines.[76] The linewidths shown in Figures 5.8 and 5.9 were calculated with the initial Morse potential fit of $O_2(d^1\Pi_g)$ and the $O_2(II^1\Pi_g)$ potential shown in blue, which represents a shift in equilibrium radius. The potentials used to calculate the linewidths in Figure 5.11 are shown by the solid black lines. The well depth and width of the $O_2(d^1\Pi_g)$ potential were adjusted until the vibrational levels matched the energies of Morrill et al.[74] and the $O_2(II^1\Pi_g)$ potential was shifted horizontally (and the asymptote was lowered by 30 cm^{-1}) to reproduce the experimental linewidths for $^{16}O_2(v = 4)$. The final $O_2(d^1\Pi_g)$ potential has a deeper well depth than the original calculations, but remains similar in shape. The final $O_2(II^1\Pi_g)$ is very close to the original calculations.

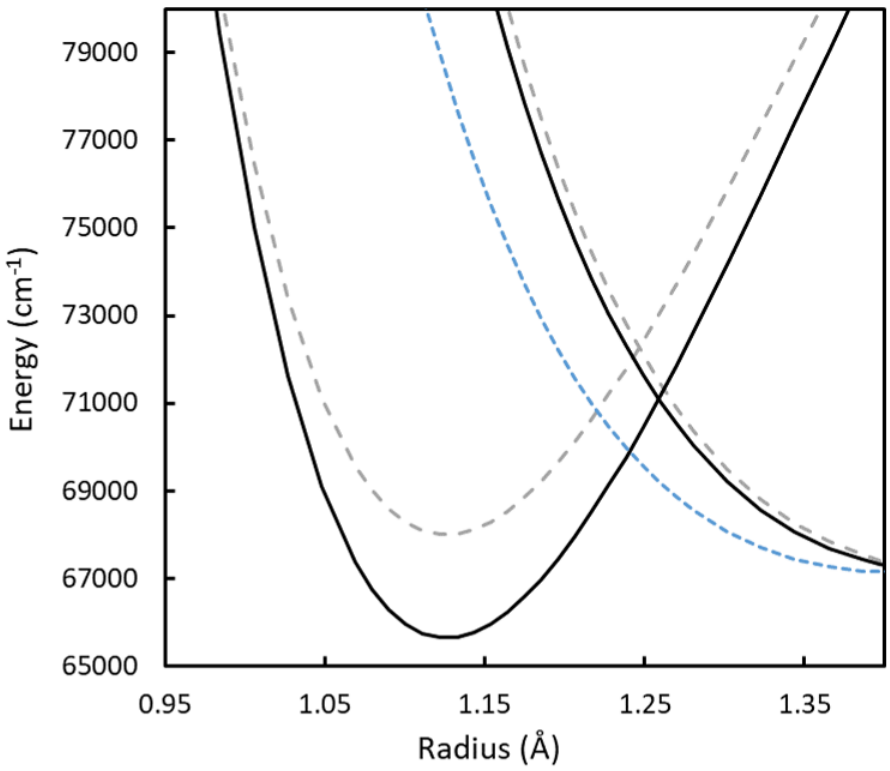

Figure 5.13: The potentials shown in gray represent Morse functions fit to the potentials for $O_2(d^1\Pi_g$ and $II^1\Pi_g)$ calculated by Li et al.[76] The initial $O_2(d^1\Pi_g)$ potential and the potential shown in blue, representing an adjusted $O_2(II^1\Pi_g)$ potential, were used to calculate the linewidths in Figures 5.8 and 5.9. The adjusted potentials shown in black were used to calculate the linewidths in Figure 5.11.

6. CONCLUSIONS AND FUTURE WORK

6.1 Conclusions

This dissertation has extended measurements of the O_2 fragment following O_3 photodissociation to both the short and long wavelength regions of the Hartley absorption band. At 226 nm, the observed $O_2(a^1\Delta_g)$ rotational distribution and vector correlations are consistent with previous measurements in the Hartley band. The rotational state distribution shifts to higher rotational states and the suppression of the odd rotational states slightly increases with increasing dissociation energy. The measured rotational envelope is largely consistent with the calculated rotational state distribution, but lacks the shoulder at high rotational states predicted by classical trajectory calculations. The $\boldsymbol{\mu}$-$\boldsymbol{v}$ correlation is mostly parallel, but the value of $\beta_0^2(20)$ is closer to zero at 226 nm than at longer wavelengths. This is consistent with the previously observed trend and results from a large recoil velocity minimizing the effect of the bending potential restoring force that deflects the fragments toward the direction of $\boldsymbol{\mu}$. The $\boldsymbol{v}$-$\boldsymbol{j}$ correlation is mostly perpendicular but is closer to zero than expected. Parent translational and rotational motion depolarize the $\boldsymbol{v}$-$\boldsymbol{j}$ correlation, but this effect should be minimal at cold temperatures and high rotational states. Overlap between the O- and P-branch transitions in the ion images affecting the angular distributions may also contribute to the deviation from the expected perpendicular $\boldsymbol{v}$-$\boldsymbol{j}$ correlation.

The Huggins band is the structured long wavelength tail of the Hartley band between 310 and 370 nm, and in this energy range O_3 is excited to the bound region of the B state. The dissociation dynamics are significantly different following Huggins band absorption with spin-forbidden dissociation channels dominating. The $O_2(a^1\Delta_g$ and $b^1\Sigma_g^+)$ fragments have

been probed following spin-forbidden dissociation in the Huggins band. The odd rotational states of $O_2(a^1\Delta_g)$ are enhanced in the $O_2(d^1\Pi_g, v = 2 \leftarrow\leftarrow a^1\Delta_g, v = 0)$ REMPI spectrum following dissociation near 320 nm, consistent with calculations from Grebenshchikov and Rosenwaks that predict stronger coupling between the B state of O_3 and the $^3A''$ states that lead to odd rotational states of $O_2(a^1\Delta_g)$ and weaker coupling between the B state and the $^3A'$ states that lead to even rotational states.[65] There is evidence in the ion image speed distributions following 320 nm dissociation and the REMPI spectrum following 330 nm dissociation that the rotational state distribution of $O_2(a^1\Delta_g, v = 0)$ is broad, extending from at least j=17 to 43 at both dissociation wavelengths. In contrast, the rotational state distribution of $O_2(b^1\Sigma_g^+, v = 0)$ is narrow, extending from j=24 to 40, and the rotational state distribution is largely independent of vibrational state. The vibrational distribution peaks at v=0 and decreases with increasing vibrational state, extending to at least v=4. The maximum of the distribution at v=0 is similar to measurements and calculations of the $O_2(a^1\Delta_g)$ vibrational distribution in the spin-allowed dissociation channel in the Hartley band, but the measured distribution is inconsistent with the vibrational distributions used by Ulrich et al. to fit the $O(^3P)$ images.[71] In the "full" analysis by Ulrich et al., only v=0 and v=2 are populated at 328.022 nm with a higher population in v=2. In the "restricted" analysis, only v=0 and v=1 are populated with a higher population in v=1.

6.2 Future Work

6.2.1 2-Color REMPI probing $O_2(a^1\Delta_g)$ and $O_2(b^1\Sigma_g^+)$

The intensity of the $O_2(b^1\Sigma_g^+)$ REMPI peaks in the 1-color spectrum do not clearly correlate with Huggins band structure, so we do not believe O_3 absorbance is a primary factor in the measured $O_2(b^1\Sigma_g^+)$ rotational state distribution. However, peaks with high intensity

in the $O_2(d^1\Pi_g, v = 1 \leftarrow\leftarrow a^1\Delta_g, v = 0)$ REMPI spectrum overlap with peaks in the $O(^3P)$ yield spectrum, so the O_3 absorbance may have an effect on the measured REMPI spectrum of $O_2(a^1\Delta_g)$. Dissociation at wavelengths corresponding to excitation of different vibrational modes may result in different branching ratios between the electronic channels of O_2 or different rotational distributions. There may also be differences for dissociation on-resonance or off-resonance of the O_3 absorbance peaks. 2-color experiments that utilize a single dissociation wavelength independent of the probe wavelength would eliminate the possibility of the O_3 absorbance cross section affecting the REMPI spectra and allow studies of the wavelength dependence of the branching ratio between dissociation channels and the fragment rotational distributions. While only general comparisons between the 320 and 330 nm rotational state distributions of $O_2(a^1\Delta_g)$ could be made based on the 1-color experiments, 2-color experiments would allow clear identification of wavelength-dependent trends in the rotational state distribution. In the Hartley band, the $O_2(a^1\Delta_g)$ rotational distribution shifts to higher rotational states with increasing dissociation energy, but it is unclear if this trend is also present in the Huggins band. The rotational state distribution of the $O_2(b^1\Sigma_g^+)$ fragment was only measured following 330 nm dissociation of O_3, so additional 2-color studies probing the $O_2(b^1\Sigma_g^+)$ fragment following 320 nm dissociation would allow identification of the wavelength dependence of the $O_2(b^1\Sigma_g^+)$ rotational distribution as well.

2-color experiments would be particularly useful in obtaining a more accurate $O_2(a^1\Delta_g)$ rotational state distribution. The 1-0 and 2-0 bands of the $O_2(d^1\Pi_g \leftarrow\leftarrow a^1\Delta_g)$ transition were used in Chapter 4 because the 1-0 band overlaps in wavelength with the $O_2(d^1\Pi_g, v = 4 \leftarrow\leftarrow b^1\Sigma_g^+, v = 0)$ REMPI scheme, and the 2-0 band was used for comparison of the even-odd alternation with previous studies. The 4-0 band near 303 nm, however, would ex-

cite $O_2(a^1\Delta_g, v = 0)$ to the unperturbed v=4 level of the $d^1\Pi_g$ state. A 2-color experiment with 320 or 330 nm dissociation of O_3 and 303 nm probing of the $O_2(a^1\Delta_g)$ fragment would allow more straightforward rotational distribution analysis. Extracting populations from an unperturbed REMPI spectrum would also allow a more quantitative comparison of the A' versus A'' contributions to the spin-forbidden dissociation channels. In the 1-color 320 nm REMPI spectrum in Chapter 4, the odd states appear to be enhanced but the relative intensities of the peaks cannot directly provide relative even and odd state populations because the vibrational state accessed in the REMPI scheme is perturbed. In a REMPI spectrum accessing an unperturbed vibrational level, the relative intensities of the even and odd states would be reflective of the relative contributions of A' and A'' states to the dissociation because the A' states correlate with even rotational states of the O_2 fragment and the A'' with odd. Calculations of the coupling between the B state and $^3A'$ and $^3A''$ states have only been performed for a single geometry, so quantitative measurements of the relative A' and A'' contributions to the dissociation would provide a more complete picture of the couplings.

Full vector-correlation analysis, which is limited in 1-color experiments that require a single laser geometry, would also be possible in 2-color experiments. Similarities in vector correlations of even and odd rotational states of $O_2(a^1\Delta_g)$ would further support the conclusion that the difference in even and odd state intensity is due to differences in coupling between the B state and the $^3A'$ and $^3A''$ states, but the vector correlations may be different because the dissociations leading to even and odd states occur on different potentials. Obtaining values for $\beta_0^2(20)$ could also provide insight into the excited state lifetime.

6.2.2 Imaging of the O(^3P) Fragment

Studies of the molecular fragment following O_3 dissociation are averaged over the three spin-orbit states of the atomic O($^3P_{2,1,0}$) co-fragment. The differences in energy of the three spin-orbit states are very small, so the O_2 fragments formed with each of the three atomic states should have slightly different translational energies, but are typically indistinguishable in the ion images. Previous imaging studies by Ulrich et al. only reported images and speed distributions of the O($^3P_2$) fragment,[71] but it is possible the images of O($^3P_1$ and $^3P_0$) are different. The three components of the triplet O_3 states may correlate with specific spin-orbit states of the O(^3P) fragment, but multiple O_3 states correlate to each pair of O and O_2 spin-forbidden products, so predicting the resulting ratio of O spin-orbit states is difficult. However, the variations in the coupling between the B state and the triplet O_3 states indicate differences in the channels producing O($^3P_2$, $^3P_1$, and $^3P_0$) are likely. The spin-orbit states have previously been compared at several wavelengths in the Hartley band.[8,48,55,57,59,125–127] While there is some variation in the reported branching ratios between the spin-orbit states, the ratio is generally near-statistical. The anisotropy of the images, however, varies with spin-orbit states in some cases. The differences between O($^3P_2$, $^3P_1$, and $^3P_0$) in the Huggins band cannot be predicted without extensive calculations of the potential energy surfaces, but a comparison of the total O_2 speed distribution measured in the 2D-REMPI in Chapter 4 with the O($^3P_2$) speed distribution at a similar wavelength reported by Ulrich et al. can be made.

Figure 6.1 shows a comparison of the atomic O(^3P) speed distribution derived from measurements of the O_2 2D-REMPI collected between 326.62 and 328.90 nm and the total kinetic energy distribution following 328.022 nm dissociation reported by Ulrich et al.[71] The dashed black line represents the speed distribution of the O($^3P_2$) fragment measured

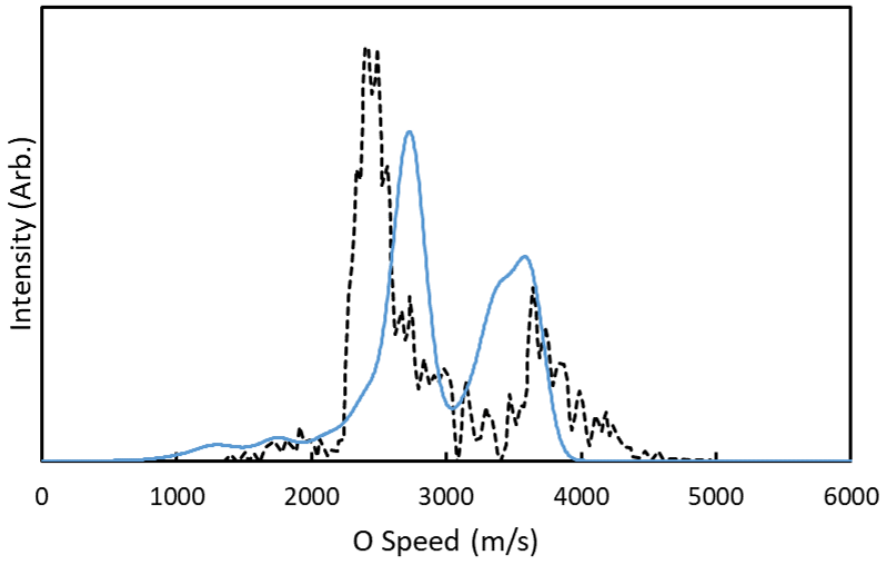

Figure 6.1: The black dashed line represents the atomic O($^3P_2$) speed derived from the total kinetic energy distribution reported by Ulrich et al. for a 328.022 nm dissociation of O_3.[71] The solid blue line represents the atomic O($^3P_2$) speed distribution obtained by converting the O_2 speed distribution measured in the 2D-REMPI spectrum to an O($^3P_2$) speed distribution with the conservation of energy.

by Ulrich et al. The reported total kinetic energy distribution was converted directly to a speed distribution of the atomic O($^3P_2$) fragment. The solid blue line is a simulated atomic O($^3P_2$) speed distribution using measurements of the $O_2(a^1\Delta_g$ and $b^1\Sigma_g)$ fragments in the 2D-REMPI spectrum. The parent O_3 rotational distribution used in the calculations was assumed to be 50 K based on the NO temperature calibration discussed in Chapter 2. For a single co-fragment rotational state, the simulated O($^3P_2$) speed distribution was obtained by calculating the fragment speed resulting from the energy of an individual rotational state of O_3 using the conservation of energy, weighted by the Boltzmann factor. The speeds were binned and summed, and the resulting speed distribution was Gaussian blurred with σ=100 m/s, which corresponds to approximately twice the σ used in fitting the speed distribution of the O_2 fragment because the O(^3P) fragment is traveling twice the speed. This was repeated for each rotational state measured in the $O_2(b^1\Sigma_g^+)$ spectra for v=0-4, weighted by the relative population of the ro-vibrational state. The same process was repeated for the $O_2(a^1\Delta_g)$ fragment. Measurements were only made for v=0 of $O_2(a^1\Delta_g)$ but the same vibrational state distribution was used for both O_2 electronic states and the same rotational state distribution was used for all vibrational levels of the $O_2(a^1\Delta_g)$ fragment as an approximation. Previous studies have estimated the branching ratio between channels forming O(^3P) with $O_2(a^1\Delta_g)$ and $O_2(b^1\Sigma_g^+)$ co-fragments to be equal, so the distributions for the two electronic states of the co-fragment were relatively scaled to have equal areas.

The peak at lower speeds results from an $O_2(b^1\Sigma_g^+)$ co-fragment because the electronic energy is higher than the $a^1\Delta_g$ state that leads to O(^3P) fragments at faster speeds. The O(^3P) speed distribution is also expected to have a peak at faster speeds corresponding to the $O_2(X^3\Sigma_g^-)$ co-fragment, which was not included in the simulation shown in blue. The

width of the low speed peaks is narrower than that of the high speed peaks, consistent with the narrower rotational state distribution observed in the $O_2(b^1\Sigma_g^+)$ fragment. The shapes of the peaks are different between the measurements of $O(^3P_2)$ and the simulation based on measurements of the O_2 fragment, which may be indicative of differences in the spin-orbit states of $O(^3P)$. If the spin-orbit states of $O(^3P)$ are formed with different distributions of O_2 co-fragments, the addition of $O(^3P_1$ and $^3P_0)$ speed distributions may account for the differences in Figure 6.1

This also emphasizes the need for full quantum calculations on Huggins band spin-forbidden dissociation dynamics. Calculations have been reported for the prediction of the rotational and vibrational state distributions of the $O_2(X^3\Sigma_g^-)$ fragment following Huggins band dissociation,[71] but to our knowledge, dynamics calculations have not yet been performed on the spin-forbidden channels. Calculations could elucidate differences between the triplet O_2 states that couple with the B state leading to spin-forbidden products as well as differences between channels producing $O(^3P_2$, $^3P_1$, and $^3P_0)$. 1D potential energy curves of the triplet states that cross the B state of O_3 and correlate with spin-forbidden products have previously been reported as well as the coupling between the B state and the triplet states for a single geometry.[2,65,118] Calculations of the complete potential energy surfaces could provide insight into the origin of the broad rotational state distribution observed in $O_2(a^1\Delta_g)$ and the narrow distribution in $O_2(b^1\Sigma_g^+)$.

6.2.3 Below-Threshold Dissociation of Vibrationally Excited Ozone

Extensive calculations have been performed on Hartley band dissociations via the spin-allowed dissociation channels and are largely consistent with experimental results. However, calculations have focused on dissociations of cold parent molecules, typically in the ground

vibrational and rotational states. However, the temperature-dependent production of singlet O and O_2 products just below the singlet channel threshold has been attributed to the dissociation of vibrationally excited O_3 molecules. O_2 signal consistent with hot band dissociation was observed in the 1-color 320 nm images discussed in Chapter 4, but the specific vibrational state of O_3 was not able to be assigned. To our knowledge, no trajectory calculations have been performed with initial vibrational energy in the parent O_3 molecule. Calculations in combination with additional experiments could help definitively assign the vibrational state of O_3 corresponding to the observed O_2 fragments at lower velocities. Analysis of the images in Chapter 4 was difficult because the reconstruction method does not work as well at small radii in the images, so additional experiments that allow the slower O_2 fragments to expand farther on the detector may also help in the assignment of the O_3 vibrational state. Greater expansion can be accomplished by lowering the repeller voltage so the fragments travel more slowly down the flight tube and have more time to expand radially. Alternatively, a longer flight tube could also result in greater expansion.

6.2.4 Ozone Dissociation to form Herzberg States of O_2

The production of low velocity $O(^3P)$ fragments from 226 nm dissociation of O_3 was long thought to originate from dissociations forming highly vibrationally excited $O_2(X^3\Sigma_g^-)$ co-fragments.[8] In a more recent study by Schinke et al., the authors instead attributed the low-velocity $O(^3P)$ fragments to dissociations forming O_2 in the Herzberg states ($A'\ ^3\Delta_u$ and $A\ ^3\Sigma_u^+$), which are higher in energy than the $a^1\Delta_g$ and $b^1\Sigma_g^+$ states, as shown in Figure 6.2.[48] The energetic threshold for the formation of $O(^3P)$ and highly vibrationally excited $O_2(X^3\Sigma_g^-)$ products from Geiser et al. is shown in blue for comparison.[57] Imaging experiments were conducted by Schinke et al. on the $O(^3P)$ fragment with higher resolution of

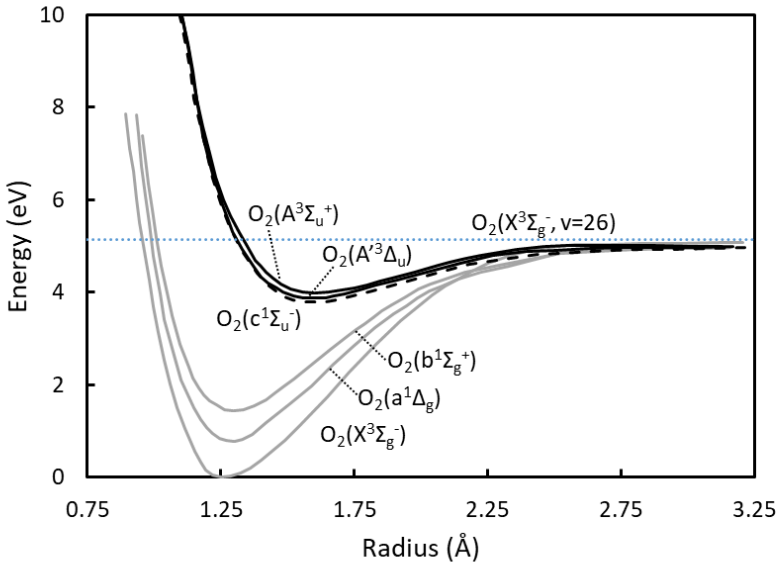

Figure 6.2: Potential energy curves of O_2 from Scheidsbach and Parker.[128] Curves of the previously discussed $X^3\Sigma_g^-$, $a^1\Delta_g$, and $b^1\Sigma_g^+$ states are shown in gray. Curves of the three Herzberg states ($c\ ^1\Sigma_u^-$, $A'\ ^3\Delta_u$, and $A\ ^3\Sigma_u^+$) are shown in black. The threshold for the production of $O(^3P_2)$ and $O_2(X^3\Sigma_g^-, v = 26)$ from Geiser et al. is shown in blue.[57]

the low-velocity fragments than previous studies. The resulting translational energy distributions of $O(^3P_2)$ and $O(^3P_1)$ are shown on the left and right, respectively, in Figure 6.3.[48] The combs at the top correspond to the vibrational levels of the $O_2(^3\Delta_u)$ (red) and $O_2(^3\Sigma_u^+)$

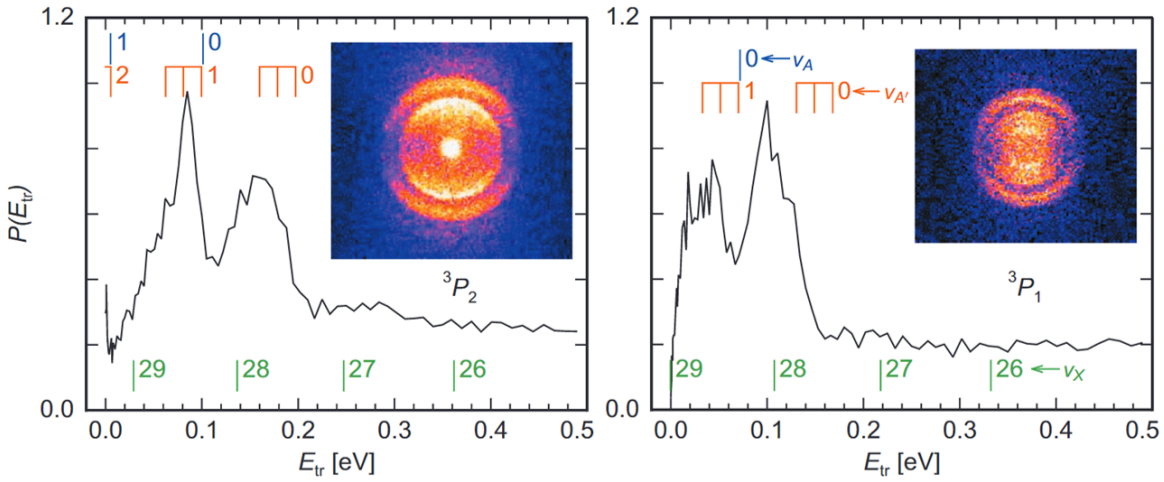

Figure 6.3: Sliced ion images and speed distributions of low-velocity $O(^3P_{2,1})$ following 226 nm dissociation of O_3 from Schinke et al.[48] The structure in the speed distributions are attributed to low vibrational states of the $O_2(A'\ ^3\Delta_u)$ (red) and $O_2(A\ ^3\Sigma_u^+)$ (blue) co-fragments, and the vibrational levels of $O_2(X^3\Sigma_g^-)$ corresponding to the same energies are indicated in green. Reprinted from J. Chem. Phys. 131, 011101 (2009), with the permission of AIP Publishing.

(blue) co-fragments, and the green comb at the bottom indicates the vibrational levels of the $O_2(X^3\Sigma_g^-)$ corresponding to these energies for comparison to previous assignments. The translational energy of the atomic fragment is consistent with formation of low vibrational levels of the Herzberg states. Full multistate dynamics calculations were not performed due to the high number of potentials involved and the complexity of their interactions, but the

authors proposed a possible mechanism for the formation of the O_2 fragment in Herzberg states.

Direct probing of the Herzberg states would allow further confirmation that $O_2(A'\ ^3\Delta_u$ and $A\ ^3\Sigma_u^+)$ fragments are produced following dissociation of O_3 at high energies in the Hartley band. A 2-color secondary dissociation experiment could be performed in which ozone in a molecular beam is dissociated at 226 nm, and the O_2 fragment is dissociated by a second laser. If a low vibrational state (v=0, 1) of the Herzberg states are formed as assigned in Figure 6.3, a wavelength near 320 nm would excite $O_2(A'\ ^3\Delta_u, A\ ^3\Sigma_u^+)$ to one of the $^3\Pi_g$ states, which interact and form an avoided crossing. The $^3\Pi_g$ states correlate with $O(^3P)$ and $O(^1D)$ products or two $O(^3P)$ atoms as shown in Figure 6.4. The resulting $O(^3P)$ fragments can be probed via REMPI at 226 nm. To use the same 226 nm laser as both the initial dissociation laser and the final probe laser, the two lasers would need to be overlapped in time.

In general, the speed distributions of atomic images are more difficult to analyze than molecular images following triatomic dissociation due to the large number of possible co-fragment states, The $O(^3P)$ images resulting from secondary dissociation of the Herzberg states will be particularly complex because multiple dissociation channels will be contributing to the measured signal. However, due to the high electronic energy of the Herzberg states, the O_2 molecules will have low velocity following O_3 dissociation as shown in Figure 6.3. The observed translational energy of the $O(^3P)$ fragments should therefore be primarily from the secondary dissociation of O_2. Using a wavelength that produces 1-color signal of O_2 near 320 nm may be useful for initial alignment and optimization. The images will include signal from 1-color dissociation of O_3 through the spin-allowed triplet channel forming

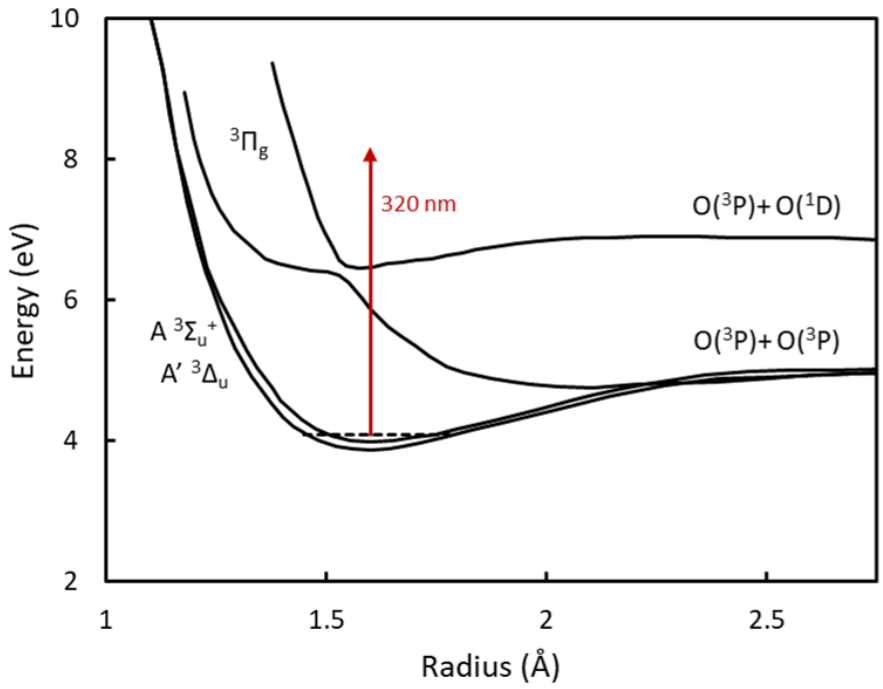

Figure 6.4: Potential energy curves of the Herzberg states and two $^3\Pi_g$ states that correlate with O(^3P) and O(^1D) products or O(^3P) and O(^3P).[128]

$O(X^3\Sigma_g^-)$ with $O(^3P)$, 2-color signal from $\sim$ 320 nm dissociation of O_3 in the spin-allowed triplet and spin-forbidden channels, and the secondary dissociation of O_2 Herzberg states following 226 nm dissociation of O_3. The images of $O(^3P)$ directly from dissociation of O_3 will need to be subtracted from the images collected with overlapping laser timing to obtain the speed distribution of $O(^3P)$ resulting from Herzberg dissociation.

If the $O(^3P)$ images contain features not accounted for by direct dissociation of O_3 either by the 226 nm laser or the $\sim$ 320 nm laser, this would imply an additional dissociation mechanism is at play. The $O(^3P)$ speed distribution resulting from Herzberg dissociation could be compared to the distribution of $O(^3P)$ formed directly from O_3 dissociation with O_2 co-fragments in the Herzberg states. If the energy distributions are consistent with each other, this would further support the explanation of Schinke et al. for the slow-moving $O(^3P)$ fragments following 226 nm dissociation of O_3.[48] Initial excitation to the B state is expected for dissociations forming the Herzberg states, so $\boldsymbol{\mu}$ and $\boldsymbol{v}$ should be mostly parallel, but differences in the image anisotropy between the direct dissociation of O_3 and the secondary dissociation of the O_2 Herzberg states could provide insight into the excited state lifetime. Schinke et al. have provided compelling experimental and theoretical evidence for the production of the O_2 Herzberg states, but studying the states directly would provide additional support for this explanation.

REFERENCES

1. H. S. Johnston, *Annu. Rev. Phys. Chem.* **43**, 1–32 (1992).

2. S. Y. Grebenshchikov, Z.-W. Qu, H. Zhu, R. Schinke, *Phys. Chem. Chem. Phys.* **9**, 2044–2064 (2007).

3. R. Schinke, G. C. McBane, *J. Chem. Phys.* **132**, 044305 (2010).

4. G. C. McBane, L. T. Nguyen, R. Schinke, *J. Chem Phys.* **133**, 144312 (2010).

5. D. Picconi, S. Y. Grebenshchikov, *J. Chem. Phys.* **141**, 074311 (2014).

6. S. Han, C. E. Gunthardt, R. Dawes, D. Xie, S. W. North, H. Guo, *PNAS* **117**, 21065–21069 (2020).

7. J. J. Valentini, D. P. Gerrity, D. L. Phillips, J.-C. Nieh, K. D. Tabor, *J. Chem. Phys.* **86**, 6745–6756 (1987).

8. R. L. Miller, A. G. Suits, P. L. Houston, R. Toumi, J. A. Mack, A. M. Wodtke, *Science* **265**, 1831–1838 (1994).

9. A. R. Ravishankara, G. Hancock, M. Kawasaki, Y. Matsumi, *Science* **280**, 60–61 (1998).

10. S. M. Dylewski, J. D. Geiser, P. L. Houston, *J. Chem. Phys.* **115**, 7460–7473 (2001).

11. Y. Matsumi, M. Kawasaki, *Chem. Rev.* **103**, 4767–4782 (2003).

12. M. L. Warter, C. E. Gunthardt, W. Wei, G. C. McBane, S. W. North, *J. Chem. Phys.* **149**, 134309 (2018).

13. Z.-W. Qu, H. Zhu, S. Y. Grebenshchikov, R. Schinke, *J. Chem. Phys.* **123**, 074305 (2005).

14. Z.-W. Qu, H. Zhu, S. Y. Grebenshchikov, R. Schinke, *J. Chem. Phys.* **122**, 191102 (2005).

15. L. Froidevaux, M. Allen, Y. L. Yung, *J. Geophys. Res.* **90**, 12999–13029 (1985).

16. P. L. Houston, A. G. Suits, R. Toumi, *J. Geophys. Res.* **101**, 18829–18834 (1996).

17. K. W. Jucks, D. G. Johnson, K. V. Chance, W. A. Traub, J. J. Margitan, G. B. Osterman, R. J. Salawitch, Y. Sasano, *Geophys. Res. Lett.* **25**, 3935–3938 (1998).

18. R. Khosravi, G. P. Brasseur, A. K. Smith, D. W. Rusch, J. W. Waters, J. M. Russell III, *J. Geophys. Res.* **103**, 16203–16219 (1998).

19. D. Lauvergnat, D. C. Clary, *J. Chem. Phys.* **108**, 3566–3573 (1998).

20. A. J. C. Varandas, *ChemPhysChem* **3**, 433–441 (2002).

21. A. J. C. Varandas, *J. Phys. Chem. A* **108**, 758–769 (2004).

22. L. Millán, S. Wang, N. Livesey, D. Kinnison, H. Sagawa, Y. Kasai, *Atmos. Chem. Phys.* **15**, 2889–2902 (2015).

23. R. T. Clancy, D. W. Rusch, R. J. Thomas, M. Allen, R. S. Eckman, *J. Geophys. Res.* **92**, 3067–3080 (1987).

24. T. G. Slanger, L. E. Jusinski, G. Black, G. E. Gadd, *Science* **241**, 945–950 (1988).

25. R. Toumi, B. J. Kerridge, J. A. Pyle, *Nature* **351**, 217–219 (1991).

26. K. Minschwaner, R. J. Salawitch, M. B. McElroy, *J. Geophys. Res.* **98**, 10543–10561 (1993).

27. J. Eluszkiewicz, M. Allen, *J. Geophys. Res.* **98**, 1069–1082 (1993).

28. C. A. Rogaski, J. M. Price, J. A. Mack, A. M. Wodtke, *Geophys. Res. Lett.* **20**, 2885–2888 (1993).

29. P. J. Crutzen, J.-U. Grooss, C. Brühl, R. Müller, J. M. Russell III, *Science* **268**, 705–708 (1995).

30. S. Skachko, R. Ménard, Q. Errera, Y. Christophe, S. Chabrillat, *Geosci. Model. Dev.* **9**, 2893–2908 (2016).

31. Q. Errera, S. Chabrillat, Y. Christophe, J. Debosscher, D. Hubert, W. Lahoz, M. L. Santee, M. Shiotani, S. Skachko, T. von Clarmann, K. Walker, *Atmos. Chem. Phys.* **19**, 13647–13679 (2019).

32. P. Warneck, *Chemistry of the Natural Atmosphere* (Academic Press, London, ed. 2, 2000).

33. S. Ndengué, S. Madronich, F. Gatti, H.-D. Meyer, O. Motapon, R. Jost, *J. Geophys. Res. Atmos.* **119**, 4286–4302 (2014).

34. K. Mauersberger, *Geophys. Res. Lett.* **8**, 935–937 (1981).

35. D. Krankowsky, F. Bartecki, G. G. Klees, K. Mauersberger, K. Schellenbach, J. Stehr, *Geophys. Res. Lett.* **22**, 1713–1716 (1995).

36. D. Krankowsky, K. Mauersberger, *Science* **274**, 1324–1325 (1996).

37. G. I. Gellene, *Science* **274**, 1344–1346 (1996).

38. S. M. Anderson, D. Hülsebusch, K. Mauersberger, *J. Chem. Phys.* **107**, 5385–5392 (1997).

39. K. Mauersberger, B. Erbacher, D. Krankowsky, J. Günther, R. Nickel, *Science* **283**, 370–372 (1999).

40. Y. Q. Gao, R. A. Marcus, *Science* **293**, 259–263 (2001).

41. C. E. Miller, R. M. Onorato, M.-C. Liang, Y. L. Yung, *Geophys. Res. Lett.* **32**, L14814 (2005).

42. S. A. Ndengué, F. Gatti, R. Schinke, H.-D. Meyer, R. Jost, *J. Phys. Chem. A* **114**, 9855–9863 (2010).

43. S. A. Ndengué, R. Schinke, F. Gatti, H.-D. Meyer, R. Jost, *J. Phys. Chem. A* **116**, 12271–12279 (2012).

44. S. P. Sander, J. Abbatt, J. R. Barker, J. B. Burkholder, R. R. Friedl, D. M. Golden, R. E. Huie, C. E. Kolb, M. J. Kurylo, G. K. Moortgat, V. L. Orkin, P. H. Wine, *Chemical Kinetics and Photochemical Data for Use in Atmospheric Studies, Evaluation Number 17* (Jet Propulsion Laboratory, 2011).

45. L. T. Molina, M. J. Molina, *J. Geophys. Res.* **91**, 14501–14508 (1986).

46. R. Atkinson, D. L. Baulch, R. A. Cox, R. F. Hampson Jr., J. A. Kerr, M. J. Rossi, J. Troe, *J. Phys. Chem. Ref. Data* **26**, 1329–1499 (1997).

47. C. E. Gunthardt, M. N. Aardema, G. E. Hall, S. W. North, *J. Chem. Phys.* **151**, 224302 (2019).

48. R. Schinke, G. C. McBane, L. Shen, P. C. Singh, A. G. Suits, *J. Chem. Phys.* **131**, 011101 (2009).

49. P. H. Wine, A. R. Ravishankara, *Chem. Phys.* **69**, 365–373 (1982).

50. A. A. Turnipseed, G. L. Vaghjiani, T. Gierczak, J. E. Thompson, A. R. Ravishankara, *J. Chem. Phys.* **95**, 3244–3251 (1991).

51. K. Takahashi, S. Hayashi, Y. Matsumi, N. Taniguchi, S. Hayashida, *J. Geophys. Res.* **107**, ACH 11-1-ACH 11–8 (2002).

52. R. K. Talukdar, C. A. Longfellow, M. K. Gilles, A. R. Ravishankara, *Geophys. Res. Lett.* **25**, 143–146 (1998).

53. R. K. Sparks, L. R. Carlson, K. Shobatake, M. L. Kowalczyk, Y. T. Lee, *J. Chem. Phys.* **72**, 1401–1402 (1980).

54. M. N. Aardema, G. C. McBane, S. W. North, *J. Phys. Chem. A* **126**, 6898–6907 (2022).

55. J. A. Syage, *J. Phys. Chem.* **99**, 16530–16533 (1995).

56. R. J. Wilson, J. A. Mueller, P. L. Houston, *J. Phys. Chem. A* **101**, 7593–7599 (1997).

57. J. D. Geiser, S. M. Dylewski, J. A. Mueller, R. J. Wilson, R. Toumi, P. L. Houston, *J. Chem. Phys.* **112**, 1279–1286 (2000).

58. T. Kinugawa, T. Sato, T. Arikawa, Y. Matsumi, M. Kawasaki, *J. Chem. Phys.* **93**, 3289–3294 (1990).

59. M. Brouard, A. Goman, S. J. Horrocks, A. J. Johnsen, F. Quadrini, W.-H. Yuen, *J. Chem. Phys.* **127**, 144304 (2007).

60. J. J. Valentini, *Chem. Phys. Lett.* **96**, 395–398 (1983).

61. P. O'Keeffe, T. Ridley, K. P. Lawley, R. R. J. Maier, R. J. Donovan, *J. Chem. Phys.* **110**, 10803–10809 (1999).

62. P. O'Keeffe, T. Ridley, K. P. Lawley, R. J. Donovan, *J. Chem. Phys.* **115**, 9311–9319 (2001).

63. K. Takahashi, M. Kishigami, Y. Matsumi, M. Kawasaki, A. J. Orr-Ewing, *J. Chem. Phys.* **105**, 5290–5293 (1996).

64. K. Takahashi, Y. Matsumi, M. Kawasaki, *J. Phys. Chem.* **100**, 4084–4089 (1996).

65. S. Y. Grebenshchikov, S. Rosenwaks, *J. Phys. Chem. A* **114**, 9809–9819 (2010).

66. S. Kuis, R. Simonaitis, J. Heicklen, *J. Geophys. Res.* **80**, 1328–1331 (1975).

67. M. Trolier, J. R. Wiesenfeld, *J. Geophys. Res.* **93**, 7119–7124 (1988).

68. S. M. Ball, G. Hancock, I. J. Murphy, S. P. Rayner, *Geophys. Res. Lett.* **20**, 2063–2066 (1993).

69. H. A. Michelsen, R. J. Salawitch, P. O. Wennberg, J. G. Anderson, *Geophys. Res. Lett.* **21**, 2227–2230 (1994).

70. W. Denzer, G. Hancock, J. C. Pinot de Moira, P. L. Tyley, *Chem. Phys.* **231**, 109–119 (1998).

71. C. K. Ulrich, J. Chen, O. Tokel, P. L. Houston, S. Y. Grebenshchikov, *J. Phys. Chem. A* **117**, 12011–12019 (2013).

72. P. O'Keeffe, T. Ridley, S. Wang, K. P. Lawley, R. J. Donovan, *Chem. Phys. Lett.* **298**, 368–374 (1998).

73. P. O'Keeffe, T. Ridley, H. A. Sheard, K. P. Lawley, R. J. Donovan, B. R. Lewis, *J. Chem. Phys.* **117**, 8705–8709 (2002).

74. J. S. Morrill, M. L. Ginter, B. R. Lewis, S. T. Gibson, *J. Chem. Phys.* **111**, 173–185 (1999).

75. W. J. van der Zande, W. Koot, J. Los, J. R. Peterson, *J. Chem. Phys.* **89**, 6758–6770 (1988).

76. Y. Li, I. D. Petsalakis, H.-P. Liebermann, G. Hirsch, R. J. Buenker, *J. Chem. Phys.* **106**, 1123–1133 (1997).

77. H. Kim, J. Park, T. C. Niday, S. W. North, *J. Chem. Phys.* **123**, 174303 (2005).

78. H. Kim, PhD thesis, Texas A&M University, 2006.

79. M. P. Grubb, M. L. Warter, K. M. Johnson, S. W. North, *J. Phys. Chem. A* **115**, 3218–3226 (2011).

80. B.-Y. Chang, R. C. Hoetzlein, J. A. Mueller, J. D. Geiser, P. L. Houston, *Rev. Sci. Instrum.* **69**, 1665–1670 (1998).

81. J. Luque, D. Crosley, *SRI International Report MP 99-009* (1999).

82. J. S. Morrill, M. L. Ginter, E. S. Hwang, T. G. Slanger, R. A. Copeland, B. R. Lewis, S. T. Gibson, *J. Molec. Spec.* **219**, 200–216 (2003).

83. R. G. Bray, R. M. Hochstrasser, *Molec. Phys.* **31**, 1199–1211 (1976).

84. D. W. Chandler, P. L. Houston, *J. Chem. Phys.* **87**, 1445–1447 (1987).

85. A. T. J. B. Eppink, D. H. Parker, *Rev. Sci. Instrum.* **68**, 3477–3484 (1997).

86. G. M. Roberts, J. L. Nixon, J. Lecointre, E. Wrede, J. R. R. Verlet, *Rev. Sci. Instrum.* **80**, 053104 (2009).

87. B. Whitaker, *Imaging in Molecular Dynamics* (Cambridge University Press, 2003).

88. V. Dribinski, A. Ossadtchi, V. A. Mandelshtam, H. Reisler, *Rev. Sci. Instrum.* **73**, 2634–2642 (2002).

89. G. A. Garcia, L. Nahon, I. Powis, *Rev. Sci. Instrum.* **75**, 4989–4996 (2004).

90. M. P. Grubb, M. L. Warter, C. D. Freeman, N. A. West, K. M. Usakoski, K. M. Johnson, J. A. Bartz, S. W. North, *J. Chem. Phys.* **135**, 094201 (2011).

91. R. N. Dixon, *J. Chem. Phys.* **85**, 1866–1879 (1986).

92. W. Wei, C. J. Wallace, M. P. Grubb, S. W. North, *J. Chem. Phys.* **147**, 013947 (2017).

93. G. E. Busch, K. R. Wilson, *J. Chem. Phys.* **56**, 3638–3654 (1972).

94. A. Schmaunz, U. Kensy, A. Slenczka, B. Dick, *Phys. Chem. Chem. Phys.* **11**, 7115–7119 (2009).

95. A. Schmaunz, U. Kensy, A. Slenczka, B. Dick, *J. Phys. Chem. A* **114**, 9948–9962 (2010).

96. A. M. Wenge, A. Schmaunz, U. Kensy, B. Dick, *Phys. Chem. Chem. Phys.* **14**, 7076–7089 (2012).

97. K. L. K. Lee, M. S. Quinn, A. T. Maccarone, K. Nauta, P. L. Houston, S. A. Reid, M. J. T. Jordan, S. H. Kable, *Chem. Sci.* **5**, 4633–4638 (2014).

98. M. S. Quinn, D. U. Andrews, K. Nauta, M. J. T. Jordan, S. H. Kable, *J. Chem. Phys.* **147**, 013935 (2017).

99. P. L. Houston, X. Wang, A. Ghosh, J. M. Bowman, M. S. Quinn, S. H. Kable, *J. Chem. Phys.* **147**, 013936 (2017).

100. H. Nakata, K. Nagamori, M. Haze, K. Yamasaki, H. Kohguchi, *J. Phys. Chem. A* **124**, 10694–10704 (2020).

101. M. S. Quinn, K. Nauta, S. H. Kable, *Molec. Phys.* **119**, e1836412 (2021).

102. J. Levine, *Spectrochim. Acta B* **69**, 61–66 (2012).

103. R. J. Le Roy, G. T. Kraemer, *University of Waterloo Chemical Physics Research Report CP-650R*^{2} (2004).

104. D. Stranges, X. Yang, J. D. Chesko, A. G. Suits, *J. Chem. Phys.* **102**, 6067–6077 (1995).

105. K. Takahashi, N. Taniguchi, Y. Matsumi, M. Kawasaki, *Chem. Phys.* **231**, 171–182 (1998).

106. M. Brouard, R. Cireasa, A. P. Clark, G. C. Groenenboom, G. Hancock, S. J. Horrocks, F. Quadrini, G. A. D. Ritchie, C. Vallance, *J. Chem. Phys.* **125**, 133308 (2006).

107. R. Schinke, S. Y. Grebenshchikov, *Chem. Phys.* **347**, 279–287 (2008).

108. C. E. Gunthardt, PhD thesis, Texas A&M University, 2020.

109. F. J. Aoiz, M. Brouard, P. A. Enriquez, R. Sayoe, *J. Chem. Soc., Faraday Trans.* **89**, 1427–1434 (1993).

110. S. W. North, G. E. Hall, *J. Chem. Phys.* **104**, 1864–1874 (1996).

111. S. W. North, G. E. Hall, *J. Chem. Phys.* **106**, 60–76 (1997).

112. W. S. McGivern, S. W. North, *J. Chem. Phys.* **116**, 7027–7034 (2002).

113. G. Hancock, P. J. Pearson, G. A. D. Ritchie, D. F. Tibbetts, *Phys. Chem. Chem. Phys.* **5**, 5386–5391 (2003).

114. G. Hancocks, P. J. Pearson, G. A. D. Ritchie, D. F. Tibbetts, *Chem. Phys. Lett.* **393**, 425–431 (2004).

115. G. Hancock, S. J. Horrocks, P. J. Pearson, G. A. D. Ritchie, D. F. Tibbetts, *J. Chem. Phys.* **122**, 244321 (2005).

116. S. J. Horrocks, G. A. D. Ritchie, T. R. Sharples, *J. Chem. Phys.* **127**, 114308 (2007).

117. G. Hancock, G. A. D. Ritchie, T. R. Sharples, *Mol. Phys.* **111**, 2012–2019 (2013).

118. H. Zhu, Z.-W. Qu, M. Tashiro, R. Schinke, *Chem. Phys. Lett.* **384**, 45–51 (2004).

119. K. Takahashi, M. Kishigami, N. Taniguchi, Y. Matsumi, M. Kawasaki, *J. Chem. Phys.* **106**, 6390–6397 (1997).

120. G. Lucchese, R. R. Lucchese, S. W. North, *J. Chem. Educ.* **87**, 345 (2010).

121. H. Reisler, A. I. Krylov, *Int. Rev. Phys. Chem.* **28**, 267–308 (2009).

122. I. C. Lane, W. H. Howie, A. J. Orr-Ewing, *Phys. Chem. Chem. Phys.* **1**, 3087–3096 (1999).

123. K. S. Dooley, M. P. Grubb, J. Geidosch, M. A. van Beek, G. C. Groenenboom, S. W. North, *Phys. Chem. Chem. Phys.* **11**, 4770–4776 (2009).

124. R. P. Saxon, B. Liu, *J. Chem. Phys.* **67**, 5432–5441 (1977).

125. T. Kinugawa, T. Sato, T. Arikawa, Y. Matsumi, M. Kawasaki, *J. Chem. Phys.* **93**, 3289–3294 (1990).

126. S. M. Shamsuddin, Y. Inagaki, Y. Matsumi, M. Kawasaki, *Can. J. Chem.* **72**, 637–642 (1994).

127. J. A. Syage, *J. Chem. Phys.* **105**, 1007–1022 (1996).

128. R. J. A. Scheidsbach, D. H. Parker, *Phys. Chem. Chem. Phys.* **21**, 14278–14283 (2019).

APPENDIX A

2+1 REMPI EQUATIONS

These equations relate experimental image anisotropy parameters (β_2, β_4, and β_6) to bipolar moments.[92]

$$\beta_2^{VV} = \frac{5\{[9800\beta_0^2(64) + 2100\beta_0^2(44) - 3080\beta_0^2(24)]s_4 + [3168\beta_0^2(42) - 7920\beta_0^2(22) - 1848\beta_0^2(02) + 16170\beta_0^0(22)]s_2 + 16170\beta_0^2(20)\}}{231\{[96\beta_0^2(42) + 40\beta_0^2(22) + 84\beta_0^2(02)]s_2 + 175\}} \tag{A.1}$$

$$\beta_4^{VV} = \frac{-[88200\beta_0^2(64) + 95900\beta_0^2(44) - 69300\beta_0^2(24) - 148225\beta_0^0(44)]s_4 - [-165528\beta_0^2(42) + 58080\beta_0^2(22) - 81312\beta_0^2(02)]s_2}{847\{[96\beta_0^2(42) + 40\beta_0^2(22) + 84\beta_0^2(02)]s_2 + 175\}} \tag{A.2}$$

$$\beta_6^{VV} = \frac{25[2590\beta_0^2(64) + 60\beta_0^2(44) - 220\beta_0^2(24)]s_4}{363\{[96\beta_0^2(42) + 40\beta_0^2(22) + 84\beta_0^2(02)]s_2 + 175\}} \tag{A.3}$$

$$\beta_2^{VH} = \frac{-10\{[455\beta_0^2(64) + 510\beta_0^2(44) - 638\beta_0^2(24)]s_4 + [792\beta_0^2(42) - 1056\beta_0^2(22)]s_2 - 1848\beta_0^2(20)\}}{[10220\beta_0^2(64) + 3840\beta_0^2(44) - 6380\beta_0^2(24) + 3465\beta_0^0(44)]s_4 + [-1584\beta_0^2(42) - 5280\beta_0^2(22) - 3696\beta_0^2(02) - 9240\beta_0^0(22)]s_2 + 9240} \tag{A.4}$$

$$\beta_2^{HV} = \frac{5\{[35\beta_0^2(64) + 15\beta_0^2(44) - 20\beta_0^2(24)]s_4 + [18\beta_0^2(42) - 24\beta_0^2(22) - 42\beta_0^0(22)]s_2\}}{[35\beta_0^2(64) + 15\beta_0^2(44) - 20\beta_0^2(24)]s_4 + [18\beta_0^2(42) + 60\beta_0^2(22) + 42\beta_0^2(02)]s_2 + 105\beta_0^2(20) - 105} \tag{A.5}$$

$$\beta_4^{HV} = \frac{-105[25\beta_0^2(64) + 14\beta_0^2(44) - 22\beta_0^2(24) + 11\beta_0^0(44)]s_4}{11\{[35\beta_0^2(64) + 15\beta_0^2(44) - 20\beta_0^2(24)]s_4 + [18\beta_0^2(42) + 60\beta_0^2(22) + 42\beta_0^2(02)]s_2 + 105\beta_0^2(20) - 105\}} \tag{A.6}$$

APPENDIX B

BCONT INPUT FILES

The following input file was used in calculating linewidths as a function of v and j for the potentials shown in Figure 5.7. Additional rows of "VJ" values can be added to calculate additional predissociation rates simultaneously.

```
'O2 predissoc'
8   8   0   1   1   1   0                % AN1 AN2 CHARGE NISTP NFS NSETS FITIT
16   16                                  % MN1 MN2
0.0015d0   0.5d0   3.5d0   1.d-6        % RH RMIN RMAX OVRCRT
0   0                                   % IWRSCH IWROVR

'Predissociation rates of O2 d state'
1   0   1   0   0                       % iset-1: ISOT BOLTZ DTYPE IFRPW PQR
3                                       % NVJ
4   1
4   5
4   10

0   0   1   118843                      % NTPI LPPOTI OMEGA(0) VLIMI
3   0   0   1  0   51155.16   1.126     % IPOTL MPAR NPAR NVARB IBOB DSCM REQ
2.83                                    % PARM(i), i=1, NVARB

1.6   1.6   0   0                       % REXFS REXTMF LPFS LPTMF

3   1   3   73783.77   1                % FSTYPE OMEGA NFSPRM VLIMF XCOORD
6647.448   1.409   2.95                 % FSPRM(j,1) j=1 NFSPRM(1)
1   13   0                             % GFS TMFTYP OTMF
575                                     % TMFPRM(m,1) m= 0 OTMF(1)
```

The following input file was used in calculating linewidths as a function of j following adjustment of the $O_2(d^1\Pi_g)$ potential to reproduce previously calculated vibrational levels from Morrill et al.[74]

```
'O2 predissoc'
8   8   0   1   1   1   0              % AN1 AN2 CHARGE NISTP NFS NSETS FITIT
16   16                                % MN1 MN2
0.0015d0   0.5d0   3.5d0   1.d-6      % RH RMIN RMAX OVRCRT
0   0                                 % IWRSCH IWROVR

'Predissociation rates of O2 d state'
1   0   1   0   0                     % iset-1: ISOT BOLTZ DTYPE IFRPW PQR
3                                     % NVJ
4   1
4   5
4   10

0   0   1   118843                    % NTPI LPPOTI OMEGA(0) VLIMI
3   0   0   1  0   53485.16   1.126  % IPOTL MPAR NPAR NVARB IBOB DSCM REQ
2.90                                  % PARM(i), i=1, NVARB

1.6   1.6   0   0                     % REXFS REXTMF LPFS LPTMF

3   1   3   73753.77   1              % FSTYPE OMEGA NFSPRM VLIMF XCOORD
6647.448   1.453   2.95               % FSPRM(j,1) j=1 NFSPRM(1)
1  13  0                              % GFS TMFTYP OTMF
525                                   % TMFPRM(m,1) m= 0 OTMF(1)
```